



Real-Time Security Assessment of Angle Stability Using Synchrophasors

Final Project Report

Power Systems Engineering Research Center

*Empowering Minds to Engineer
the Future Electric Energy System
Since 1996*



Real-Time Security Assessment of Angle Stability and Voltage Stability Using Synchrophasors

Final Project Report

Project Team

Vaithianathan “Mani” Venkatasubramanian (project leader)

Michael Sherwood

Washington State University

Venkataramana Ajjarapu, Professor

Bruno Leonardi, Ph.D. Student

Iowa State University

PSERC Document 10-10

May 2010

For information about this report, contact:

Vaithianathan “Mani” Venkatasubramanian
School of Electrical Engineering and Computer Science
Washington State University
Pullman, WA 99164-2752
Tel: 509-335-6452
Fax: 509-335-3818
Email: mani@eecs.wsu.edu

Power Systems Engineering Research Center

The Power Systems Engineering Research Center (PSERC) is a multi-university Center conducting research on challenges facing the electric power industry and educating the next generation of power engineers. More information about PSERC can be found at the Center’s website: <http://www.pserc.org>.

For additional information, contact:

Power Systems Engineering Research Center
Arizona State University
577 Engineering Research Center
Tempe, Arizona 85287-5706
Phone: 480-965-1643
Fax: 480-965-0745

Notice Concerning Copyright Material

PSERC members are given permission to copy without fee all or part of this publication for internal use if appropriate attribution is given to this document as the source material. This report is available for downloading from the PSERC website.

**© 2010 Iowa State University and Washington State University
All rights reserved**

Acknowledgements

This is the final report for the Power Systems Engineering Research Center (PSERC) research project S-31, titled “Real-Time Security Assessment of Angle Stability and Voltage Stability Using Synchrophasors.” Co-funding of this project from Tennessee Valley Authority (TVA) is gratefully acknowledged. Specifically, project team thanks Lisa Beard (who was with TVA during this project) and Floyd Galvan (Entergy) for their support throughout this project.

The project team at Washington State University (WSU) has consisted of an M.S. student Michael Sherwood (who has graduated and since joined Pacific Gas and Electric, San Francisco, CA), and a Ph.D. student Xing Liu. Prior contributions by Dongchen Hu on the topics of this report while he was an M.S. student at WSU are also gratefully acknowledged.

Iowa State University (ISU) research team consisted of a Ph.D. student Bruno Leonardi (who is expected to graduate in spring 2011) and Dr. Venkataramana Ajjarapu. The research team is grateful for the support provided by the industry advisors.

The project has greatly benefited from collaborations with engineers from several PSERC member companies including

- Ritchie Carroll (TVA)
- Gary Kobet (TVA)
- Sujit Mandal (Entergy)
- William Mittelstadt (BPA)
- Kolluri Sharma (Entergy).

We thank all our industry advisors for their support throughout this project:

- Navin Bhatt (AEP)
- Clifton Black (Southern Co)
- Jay Giri (AREVA T&D)
- Jim Gronguist (BPA)
- Jim Gurney (BCTC)
- Innocent Kamwa (IREQ)
- Robert Kingsmore (Duke Energy)
- Kip Morrison (BCTC)
- Mahendra Patel (PJM) and
- Suketu Shah (ITC)
- Jianzhong Tong (PJM)
- Bob Wilson (WAPA).

Executive Summary

This project examines the use of Phasor Measurements Units (PMUs) to assess angle and voltage stability in real time. The objective is to investigate how synchronized phasor measurements can be used to detect the loss of stability in real-time operations, be it angle stability or voltage stability. PMU deployment is becoming a common practice across the nation. Although the number of installed devices has quickly grown in the past few years, the development of applications to make use of PMU data has not been at the same pace.

This project also analyzes how PMU data can be used to detect proximity to angle instability and voltage instability by monitoring some key PMU measurements. In Part I, multiple algorithms are proposed for detecting and mitigating angle instability by triggering generation and possibly load shedding schemes whenever needed. In Part II, a model that infers how far the system is to a voltage collapse is developed.

During the development of the models, several operating scenarios and network topologies were considered to cover a wide range of daily operating conditions. The methodology makes use of wide area PMU measurements for voltage stability assessment. Important aspects of how to integrate the proposed methodology into SCADA/EMS were also taken into consideration to facilitate the practical implementation of the methodology.

Part I. Algorithms for Fast Detection and Mitigation of Angle Instability Using Synchrophasors (work done at Washington State University)

The advantages of synchrophasors are evident in their use in wide area monitoring systems where voltage magnitudes, phase angles, and frequency measurements in real time can be used for fast detection of angle instability. Problems arising from the introduction of new power market designs combined with growing presence of intermittent renewable power generation are nudging power systems towards potential dynamic instability scenarios. To help alleviate these issues, it is essential that the reliability status of a system be assessed in real time or as quickly as possible.

Synchrophasors, together with modern communication technology facilitate the monitoring of the current state of the power system, including the phase angles of the bus voltages at critical buses, in a time-synchronized fashion. The algorithms and the controller proposed in this report detect the fast separation of phase angles among the critical areas automatically by using data from synchrophasors, and proceed to mitigate the emerging angle instability by triggering suitable control action. Briefly, the algorithms initiate tripping of critical generators in the accelerating part of the system when necessary, and also initiate load shedding in the decelerating part of the system when necessary. The novelty of the algorithms is in the fact that all the decisions are made in real time purely based on the wide-area synchrophasor measurements without any knowledge of the details of relay actions that may have resulted in the angle instability phenomenon.

Part I of the report contains descriptions of methods for detection and fast mitigation of angle instability in large-scale power systems using synchrophasors. The use of synchrophasors or PMUs in automatic generation-shedding schemes, as well as load-shedding schemes have been proposed in the past. When such an action is initiated, it is extremely important to know

that it is the correct one to take since load shedding results in customer inconvenience and lost revenue. On the other hand, the total loss of a system such as from blackouts can lead to even greater economic and social impacts.

Our research team analyzed three different methods for detection of angle instability using synchrophasors. The first method is based on real-time tracking of the deviation of angle measurements of different control areas with respect to a weighted system reference angle that is computed as a real-time approximation of the system center of inertia reference frame. This method was proposed by the research team in earlier research work. The second method for determining the stability is proposed by computing an approximate version of a transient energy function. The use of transient energy functions in determining stability is shown to have potential in helping operators trigger and decide the location of generation and/or load shedding schemes. The computation of transient energy functions using real-time data from synchrophasors is therefore recommended for further study as a feasible solution to mitigating angle stability.

Our research team proposes a novel third approach for angle stability monitoring that is motivated by the least action principle from physics. The least action principle is used in theoretical physics for abstract modeling. Here, the concepts of the least action principle are applied to assessing and mitigating angle instability in power systems. From the computation of potential and kinetic energy, a different quantity known as the Lagrangian is formed. The Effort, which is the time integral of the Lagrangian, is then calculated, and is used in determining the critical generators for initiating generation shedding. The IEEE New England 39 bus test system was used to test all three algorithms.

From the testing results, it appears that synchrophasors can be effective in mitigating angle stability phenomena in power systems with the deployment of a sufficient number of synchrophasors at critical buses along with the deployment of fast communication networks to exchange the real-time data.

Part II. Online Voltage Stability Margin Monitoring Using Synchrophasor Measurements and Statistical Multi-Linear Regression Models (work done at Iowa State University)

The second part of the project is focused on the development of an online voltage stability monitoring tool. This tool is intended to make use of available phasor measurements to estimate proximity to voltage collapse. A thorough investigation of how phasor measurements can be used as potential candidates to voltage stability monitoring applications was performed. The confirmation that PMU measurements can provide important information regarding voltage stability would not only support a wider deployment of such devices in a power system, but would also stimulate the development of new software applications that use PMU data in real-time applications.

Reactive power and system voltage profiles are highly related. Voltage support is mainly achieved through proper reactive power management and control. Numerous *post mortem* system studies after significant power system events have pointed out that a shortage of proper reactive power support has been the cause of several voltage collapse incidents such as the Northeastern North American blackout in 2003. Therefore, a thorough investigation of the relationship between reactive power reserves and voltage stability margin was carried out in this project.

Another issue is what to do with the exponentially growing amount of data available at control rooms. Two common questions frequently raised in recent PSERC meetings have been:

- What should be done with the massive amount of data that is coming into control rooms?
- What kind of information can be extracted from the data?

Since most of the data being brought in is in its raw format (e.g., voltage magnitudes, active/reactive power flowing along lines, breaker status information, etc), a quantitative idea of how close a system is to an unstable/non-safe condition is not easily obtained. Such data overflow may actually distract operators from what could be a real reason for concern during real-time operations.

Intending to alleviate operator's burden in analyzing raw data and improve their awareness during real-time operations, a methodology to transform some of the data received in the control room into meaningful information was developed in this research. The methodology is based on the relationship between reactive power and voltage stability. The idea is based on offline development of a voltage stability margin estimation tool that would utilize reactive power reserves at some specific locations in the power system to indicate the voltage stability margin. An extensive voltage stability assessment of a power system is performed to include as many network topologies and load increase patterns as necessary. All the data gathered from offline simulation is then used for the development of multi-linear regression models (MLRM) that will correlate the amount of reactive power reserve (RPR) of some key generators with the voltage stability margin (VSM) of the system or area.

Due to many uncertainties involved in real-time operations, a specific set of MLRMs were needed to properly correlate RPRs and VSM. An artificial neural network (ANN) was designed for MLRM selection. The ANN uses PMU data as inputs and produces an index that represents what MLRM should be utilized. The ANN's objective is to automate the process of VSM estimation by automatically selecting the proper MLRM. Such automation avoids the need of a system operator having to select the correct MLRM to use, therefore allowing them to focus on other important tasks and also reducing the chances of human error.

The complete methodology is tested on a 1648 bus system. The results obtained showed that MLRMs can be successfully employed to estimate VSM based on the amount of RPR available at key locations. The uncertainties in load increase direction and network topology are modeled. By doing so, the VSM estimation error can be modeled using a probability distribution function. This modeling can further provide operators with confidence bounds for the estimated values of VSM which can further trigger remedial actions.

Our research team concluded that the methodology has the potential to be applied to any real-size system. Commercial grade software, such as PSS/E[®], Microsoft Excel[®] and Matlab[®], were used in the development of the methodology. Once designed, the MLRMs and the ANN can be incorporated into an EMS/SCADA for real-time VSM estimation using real-time PMU data. A software prototype is being developed and will be tested on a reduced case of the Eastern Interconnection for online voltage stability monitoring.

Part I

Algorithms for Fast Detection and Mitigation of Angle Instability Using Synchrophasors

Vaithianathan “Mani” Venkatasubramanian

Michael Sherwood*, M.S.

Washington State University

*Sherwood now works for Pacific Gas and Electric Co.

Information about this project

For information about this project contact:
Vaithianathan “Mani” Venkatasubramanian
School of Electrical Engineering and Computer Science
Washington State University
Pullman, WA 99164-2752
Tel: 509-335-6452
Fax: 509-335-3818
Email: mani@eecs.wsu.edu

Power Systems Engineering Research Center

The Power Systems Engineering Research Center (PSERC) is a multi-university Center conducting research on challenges facing the electric power industry and educating the next generation of power engineers. More information about PSERC can be found at the Center’s website: <http://www.pserc.org>.

For additional information, contact:

Power Systems Engineering Research Center
Arizona State University
577 Engineering Research Center
Tempe, Arizona 85287-5706
Phone: 480-965-1643
Fax: 480-965-0745

Notice Concerning Copyright Material

PSERC members are given permission to copy without fee all or part of this publication for internal use if appropriate attribution is given to this document as the source material. This report is available for downloading from the PSERC website.

© 2010 Washington State University. All rights reserved.

TABLE OF CONTENTS

TABLE OF CONTENTS	i
LIST OF TABLES	ii
LIST OF FIGURES	iii
1. INTRODUCTION	1
1.1 Overview	1
1.2 Load Shedding Principle	4
1.3 Overview of the Algorithms	5
2. TRANSIENT ENERGY FUNCTIONS	18
2.1 Introduction	188
2.2 Formulation	18
2.3 Lyapunov's Methods	20
2.4 Implementation	211
2.5 Conclusions	255
3. LAGRANGIAN AND EFFORT	26
3.1 Introduction	266
3.2 Formulation	266
3.3 Implementation	299
3.4 Determining Stability Limits	33
3.5 Conclusions	34
4. ANGLE MITIGATION ALGORITHM	366
4.1 Introduction	366
4.2 Formulation	366
4.3 Implementation	377
4.4 Conclusions	377
5. RESULTS AND COMPARISONS	399
5.1 New England 39 Bus Test System Fault Case	399
5.2 39 Bus 3 Area System Fault Case	466
5.3 Communication Delay Effect	633
6. CONCLUSIONS	666
7. REFERENCES	677
8. APPENDIX	70

LIST OF TABLES

Table 1- 1: Simulation Results for the Two-Area System	11
Table 1-2: Improvement on the System Stability	11
Table 3- 1: Load to Generation Ratio, 39 Bus 3-Area System	30
Table 3- 2: Control Times Comparisons For Fault At Bus 4.....	33
Table 5- 1: Unmodified 39 Bus System Thresholds	39
Table 5- 2: Control Times For Unmodified 39 Bus System	40
Table 5- 3: Critical Clearing Time Using Effort Control Times	41
Table 5- 4: Unstable Cont 1 Algorithm Comparisons	44
Table 5- 5: High Loading Level Comparisons	45
Table 5- 6: Max Loading Thresholds.....	46
Table 5- 7: Thesholds For 20% Less Load	47
Table 5- 8: Thresholds For 40% Less Load.....	47
Table 5- 9: Unstable Cases Using Maximum Loading	48
Table 5- 10: Unstable Cases Using 20% Less Load Of Maximum	50
Table 5- 11: Unstable Cases With 40% Less Load From Maximum	52
Table 5- 12: CCT at Max Loading Using Different Threshold Sets.....	54
Table 5- 13: CCT at -20% Loading Using Different Threshold Sets	55
Table 5- 14: CCT at -40% Loading Using Different Threshold Sets	56
Table 5- 15: Excessive Loading, 3-Area System.....	57
Table 5- 16: Recommended Voltage Protection Delay Times	63
Table 5- 17: Frequency Relay Delay Times	63
Table 5- 18: Time Delay, Effort Algorithm.....	64
Table 5- 19: Time Delay, Lagrangian Algorithm	64
Table 5- 20: Time Delay, Angle Algorithm.....	65
Table 5- 21: Time Delay, Energy Algorithm.....	65
Table A- 1: 39 Bus Overload Contingencies	73
Table A- 2: Exciter Parameters	74
Table A- 3: 39 Bus Governor Parameters.....	74
Table A- 4: Generator 1 to 9 Parameters	74
Table A- 5: Generator 10 Classical Model Parameters	75

LIST OF FIGURES

Figure 1-1 Angles of each area (fault-on time=0.08 sec)	8
Figure 1-2 Angles of each area (fault-on time=0.10 sec)	9
Figure 1-3 Angles of each area (fault-on time=0.11 sec)	9
Figure 1-4 Angles of Area 1 (fault-on time=0.11 sec).....	10
Figure 1-5 Comparison of two method to compute δ_c (fault-on time=0.11 sec)	12
Figure 2-1: TE Threshold Gen4	222
Figure 2- 2: Kinetic Energy Gen 4.....	233
Figure 2- 3: Potential Energy Gen4	24
Figure 2- 4: Gen 4 Total Energy, Fault Bus 29.....	244
Figure 3- 1: System Lagrangian, Unstable Fault Case	27
Figure 3- 2: Computation of Lagrange for each generator, no fault simulated	288
Figure 3- 3: Sum of Lagrangians for Cont1, Stable.....	288
Figure 3- 4: Estimated Rotor Angle from Bus Voltage Angle Measurement.....	30
Figure 3- 5: Effort Computed for Method 1	311
Figure 3- 6: Effort Using Method 2	322
Figure 3- 7: Effort Comparison Between Methods.....	322
Figure 3- 8: Gen 3 Lagrangian Stability Limit	333
Figure 3- 9: Gen 3 Stability Limit Using Effort	344
Figure 4- 1: Estimated Rotor Angle From Voltage Angle.....	377
Figure 5- 1: Rotor Angle Estimated From Bus Voltage Angle	422
Figure 5- 2: Total System Lagrangian for Unstable Cont2.....	422
Figure 5- 3: Effort for Unstable Cont2	433
Figure 5- 4: Lagrangian Computation for Unstable Cont1	433
Figure 5- 5 Energy for Unstable Cont1.....	444
Figure 5- 6: Lagrangian for Stable Cont 4	466
Figure 5- 7: Rotor Angle For 3-Area Over Load Case	588
Figure 5- 8: Lagrangian Computation for Unstable Cont4.....	588
Figure 5- 9: Energy Computation for Unstable Cont4.....	599
Figure 5- 10: Effort Computation Unstable Cont4	60
Figure 5- 11: Unstable Cont. 2 Rotor Angle.....	611
Figure 5- 12: Unstable Cont. 2 Rotor Frequency.....	611
Figure 5- 13: Voltage Magnitude, Unstable Cont 2.....	622
Figure A- 1: Two-area Test System [14].....	70
Figure A- 2: 39 Bus 3 Area Test Case.....	71
Figure A- 3: Original 39 Bus New England Test System.....	72

1. INTRODUCTION

1.1 Overview

Operational reliability of large power systems has received much attention in the past decade because of deregulation and ever increasing loads. One of the more recent events was the August 2003 blackout which occurred in the Northeastern United States and Canada. This 2003 blackout was estimated to have cost roughly 6 billion USD in lost revenue alone, apart from the societal impact [3]. In determining corrective actions to prevent such events from occurring, it was recommended that providing better real-time tools for operators was a top priority [4]. The emergence of synchrophasors in monitoring power system conditions seems to be an attractive solution for monitoring real-time operational reliability status. Even in an ideal future system, where the voltage phasors may be available at each bus in real-time, monitoring the dynamic state is only the first step in understanding dynamic stability properties of the complex power system. For instance, in the context of angle stability, we also need to know whether or not a generator or group of generators can potentially become unstable based on interactions with other components in the system.

Real-time algorithms proposed in this report are targetted towards detecting angle instability directly from system responses as seen by wide-area synchrophasor measurements without any knowledge of the disturbances that may have led to the responses. The mitigatory control actions initiated by the algorithms are purely response based controls and should be treated as wide-area system controls. On the other hand, Remedial Action Schemes (RAS) or Special Protection Schemes (SPS) which are commonly used in the present industry for angle stability control are directly triggered by transfer trip signals of initiating multiple contingencies. With growing complexity of RAS schemes in a modern power system, the task of coordinating RAS scheme is become a very challenging task. Response based wide-area control schemes such as proposed here provide an alternate approach for mitigating angle instability in future power systems.

Voltage stability is relatively a slower phenomenon since we typically know that the areas with the lowest reactive power reserves and voltage levels are the critical areas where corrective actions will have the greatest impact on mitigating voltage stability. New algorithms recently developed at Washington State University for automatic voltage instability detection using synchrophasors will be discussed in a future report. Typically, angle stability unlike voltage stability, is a fast dynamic phenomenon and is not as easy to analyze. Although it is defined as the ability for all the generators in a system to remain

in synchronism, it is a much faster phenomenon compared to voltage stability and is not as clearly understood. In some cases, a system may not go angle unstable on the first swing. In such cases, it is not as apparent which modes or mechanisms are causing the system to lose synchronism. Whether or not the system is heavily loaded at the time of disturbance is also important since under such stressed conditions, the swings cannot be easily distinguished as being stable or unstable right away [5]. When this happens, generators that may initially appear stable will later follow the other unstable generators rather than staying in synchronism with the rest of the system.

Looking back at the August 2003 blackout, we see that eventual loss of generators and transmission lines rapidly lead to the loss of synchronism between different areas [3]. From the data given in the August 14th blackout report, we see that the loss of synchronism happens in a matter of seconds whereas the voltage declines that preceded took minutes. An approach that seems well-suited for real-time stability assessment is the transient energy function and the angle algorithms proposed earlier in the thesis of Dongchen Hu [7].

The use of transient energy functions is one method used for determining angle stability. With recent advances in data acquisition using synchrophasors, the estimation of frequency and rotor angle can be accomplished with minimal time-delays from measurement and propagation delays. Transient energy functions are computed by using the kinetic energy and potential energy of a machine. In previous attempts to use the energy function the energy dissipated in the transmission network was estimated [1]. In the use of transient energy functions applied in this report, it is assumed that the dissipated energy is negligible. What we then have is the kinetic energy as a function of rotor frequencies and the potential energy as a function of rotor angle displacements. The summation of these two terms for each machine gives the total energy of that machine. Since the total energy is a function of quantities easily measured by synchrophasors, it is clear that the approximate total energy can be computed almost as quickly as data becomes available. By studying the total energy of each machine we can see how much energy each machine can produce or absorb from the system before losing synchronism with the grid.

Several new approaches for using the individual energy functions are proposed. The Lagrangian, which is based upon the difference rather than the sum of the kinetic and potential energy, can be used in determining dynamic stability in the same way as the total energy. There are several advantages to using the Lagrangian over the total energy which will be discussed in the later chapters. The physical meaning of the Lagrangian is somewhat vague since it is used in Classical Physics as a modeling principle to determine

the equations of motion of a system. Conceptually we can visualize the Lagrangian as an indication of which way the energy is being converted between the kinetic and potential energy. The Lagrangian is treated in the same way as the total energy by noticing that a maximum amount can be attained by each machine before instability occurs. The Lagrangian is shown in the thesis of Mike Sherwood [20] to indicate angle instability faster than by using the total energy. Majority of the work reported in this report is from the M.S. thesis of Mike Sherwood [20] that was primarily funded by this PSERC project.

A new approach proposed in [20] for detecting instability is the use of Effort for the individual machines. In classical physics, Effort is known as the Action. Effort, or Action, is given by the integral of the Lagrangian over time. Interestingly enough, the minimum of the action, known as the principle of least action, gives us to determine a set of equations which describe the motion of the system. Newton's laws of motion are the more commonly used alternate method for deriving the dynamic equations. In this report, Least Action Principle is applied in the context of real-time stability. Since the Lagrangian is being computed in real-time, it makes computing the Effort a straightforward procedure. To find the limiting amount of Effort that a generator can assert, we integrate the Lagrangian along the trajectories corresponding to the fault scenario, with duration equal to the critical clearing time, near the given generator. For disturbances dealing with only faults, we calculate the Effort for the fault duration, and if the Effort exceeds the maximum amount needed for maintaining stability we take preventive action to maintain synchronism. Since it is difficult to know that there is a fault until it has been detected and cleared, we will also look at cases where the sum of the Lagrangians over all machines is used as a trigger to start computation of the Effort.

By looking at the rotor angle alone, we can also determine generators that are losing synchronism with the system. This method was proposed recently in [19] and by Dongchen Hu [7]. The algorithm works by taking the estimated rotor angle and comparing with a set threshold. Once the threshold is exceeded the rotor angle is integrated and if the integral exceeds a set amount before the rotor angle begins decreasing then control action is taken. The advantage of this is it takes away from the oversensitivity of only looking at the rotor angle, which can change depending on the modes of instability. The results of Dongchen's algorithm, which will be called the angle algorithm from this point on, are compared with the transient energy function, Lagrangian and Effort to determine accuracy between algorithms.

The terms rotor angle and rotor frequency used in this report represent the approximate rotor angle and frequency. This refers to the synchrophasors measurements taken at the generator terminal bus. The bus voltage angle is approximately equivalent to

the rotor angle with regards to its use in the preceding work. This assumption is made based on the premise that the bus is located electrically near the generator, in other words the only impedance between the bus and the internal voltage is the synchronous reactance. From simulations on the 39 bus system, differences ranging from 1 to 20 degrees were observed but this is an irrelevant difference since we are referring the bus voltage angle on a center of inertia frame, not to mention that the critical energy is calculated using the bus voltage angle. The frequency on the other hand is not measured directly. It is computed numerically from the bus voltage angle and noting the change in angle with respect to time. This can be accomplished easily since each data point has a time stamp associated with it.

The structure of this report is as follows. In Chapter 2, we discuss the transient energy function that has been proposed with only the individual machine energy being computed. The model is modified to be used with synchrophasors data referenced on a system wide center of inertia frame of reference. The use of center of inertia is implemented on both rotor angle and frequency estimates. In Chapter 3, the Lagrangian and Effort are introduced. Since the computation of Effort follows from the Lagrangian it seems fitting to include them both in the same chapter. The angle algorithm is introduced in Chapter 4 with its formulation given in [7]. In Chapter 5 the algorithms are tested on two variations of the 39 bus system. In the first setup, we treat each generator as a separate area making the plant modes more prevalent than the inter-area modes. The loading was varied to make the system more or less stressed. For the second setup several transmission lines are removed from the system and the impedances of the tie-lines between areas are increased (i.e. the line length increased) in order to test the algorithms more thoroughly. The severity of the loading in the system is then varied to determine the accuracy of each algorithm with regards to different thresholds, taken at light, medium and heavy loading.

A few remarks regarding the dynamic data used in the simulations should be stated. First off the original dynamic data included power system stabilizers. These have been removed from the models. Governor models have been added on all generators except for Generator 10 located at bus 39. The droops on each generator governors vary from 15% to 30%. The classical model was used for Generator 10 and the two axis model for the rest of the generators.

1.2 Load Shedding Principle

From conducting simulations the proposed algorithms discussed so far have been shown to be well suited for determining generation shedding. Load shedding has been difficult to determine just from using these algorithms. From the 39 bus 3 area test

system, we can see that area 2 is significantly more loaded than the other two areas. As a consequence we see that area two is importing a significant amount of power from the other two areas. We would then expect that shedding load in area 2 would have a greater effect on mitigating a ngle instability than for shedding load in the other two areas. Looking at the center of inertia for with respect to rotor angle and frequency we cannot tell at the time when control action is taken if load shedding should occur. This is because if a fault occurs in the heavily loaded area then the machines will accelerate for a short time while the transmission line is still faulted. Although in the long term we would see the frequency to decay in this area, we can not predict it for certain by using the proposed algorithms. In the following simulations, a simple algorithm is proposed to determine the most suitable area for load shedding.

This indexing for each area is based on the load to generation ratio for that area. More specifically we take the total load in the area and divide by the total generation of the system, shown in equation 1-1.

$$R_{L/G}^i = \frac{Load_i}{\sum_{i=1}^k Gen_i} \quad (1.1)$$

This equation (1.1) is evaluated at the time of control action and the area with the highest ratio is the candidate area for load shedding. For simplicity, we shed the same amount of load as generation.

1.3 Overview of the Algorithms

1.3.1 Phase angle based algorithm

A first version of the phase angle based algorithm was postulated in Appendix 3 of the recent paper [19]. This section will discuss the algorithm in more detail along with illustrative examples on standard test systems.

The algorithm in this section extends the concept of the voltage-magnitude based algorithm “Vmag” from [19] by consideration of the phase angle measurements. Briefly, the algorithm Vmag in [9] measured the severity of disturbances in the WECC system by quantifying the extent of bus voltage magnitude dips in the California-Oregon tie-line corridor below pre-specified thresholds during system swings. The phase angle algorithm of this section analyzes the phase angles of the system in a similar fashion.

The consideration of the phase angles is more challenging as compared to bus voltage magnitudes because the phase angles can vary over wide ranges during the system operation. While the voltage magnitudes are kept within tight tolerances under

normal system conditions, the phase angles and the relative phase differences can vary a lot across the system as determined by the MW power transfers and the availability of transmission paths for the power transfer. In order to handle this difficulty, we propose the concept of a real-time center of inertia angle reference for the computation of the system phase angle reference [19] that is then used to quantify the extent of phase angle variations away from the system center.

At present, the algorithm analyzes the phase angles in two stages: 1) the angle stability within each control area, and, 2) the angle stability of the entire large system. The principle in each step is similar.

First, let us recall the definition of the Center of Angles (COA) [5], [14]

$$\delta_{COA} = \frac{\sum_{i=1}^N \bar{\delta}_i H_i}{\sum_{i=1}^N H_i} \quad (1.2)$$

where $\bar{\delta}_i$ is the internal machine rotor angle for the i -th machine and H_i is the respective generator inertia time constant. Since the internal machine rotor angle cannot be directly measured in the present day power system, we approximate the internal angle with the phase angle of the high side bus voltage, which is normally monitored by synchrophasors. Similarly, the inertia time constant H_i in (1.2) is difficult to access in real-time because the number of units being dispatched from a generation plant can vary during operation. Therefore, we substitute the weights defined by the inertia constants in (1.2) with the high side active power injections of the generators. The machine inertias are typically proportional to the real power outputs. The modified formula (1.3) presented below is thus readily suited for real-time computation using the synchrophasors.

Let us assume the availability of the high side bus voltage phase angle measurements, say, δ_j^i , from a few key generating plants, say for $j=1,2,\dots,N$ in area i . Then, we introduce the notion of the approximate center of inertia angle reference for the area, say, δ_c^i , by the rule,

$$\delta_c^i = \frac{\sum_{j=1}^N \delta_j^i P_j^i}{\sum_{j=1}^N P_j^i} \quad (1.3)$$

where P_j^i denotes the current MW generation schedule at the plant j in area i . By increasing the number of phase angle measurements within each area in (1.3), we can

improve the accuracy of the computation of the angle reference δ_c^i and we can also improve the redundancy. Also, this rule (1.3) is inherently tolerant of loss of one or more PMU channels as is commonly the case in the real-time synchrophasor framework. Similarly, the center of inertia angle reference for the entire system, denoted δ_c , can be computed with the rule,

$$\delta_c = \frac{\sum_{i=1}^N \delta_c^i P^i}{\sum_{i=1}^N P^i} \quad (1.4)$$

where N is the total number of areas that are available in the control formulation, and P^i denotes the current total generation in Area i . The latest total load P^i of Area i is readily available from routine AGC calculations.

Next, we present a heuristic rule for detecting an angle instability using these concepts in a real-time framework. When the representative angle δ_c^i of an area in (1.3) continuously increases away from the center of inertia δ_c beyond a pre-specified metric, we would heuristically interpret that Area i is moving towards separation from the rest of the system. In this case, a suitable remedial action could be the tripping of generation in that area. Similarly, when the angle δ_c^i continues to decrease beyond a predefined threshold, we would interpret that as a likely separation of Area i that could be countered by load shedding in Area i . These rules need to be crosschecked by analyzing the respective real-time frequency measurements.

In our studies, we set the control trigger heuristics to be similar to the voltage error algorithm Vmag [9]. In the case of phase angles, we define $\Delta\delta_c^i = \delta_c^i - \delta_c$. We then accumulate two integral terms, denoted Ω_a^i and Ω_d^i , respectively, to denote the speeding up or slowing down of Area i with respect to the center of inertia reference frame. First, the term Ω_a^i is the integral for $\Delta\delta_c^i$, whenever $\Delta\delta_c^i$ continuously stays above a threshold, say $\Delta\delta_c^{i*}$. The accumulated error Ω_a^i is reset to zero whenever the angle $\Delta\delta_c^i$ drifts below $\Delta\delta_c^{i*}$. When Ω_a^i grows above a pre-specified value, say Ω_a^{i*} , the Area i is interpreted to be speeding away from the rest of the system and a suitable generation tripping may be initiated in that area. The value of Ω_a^{i*} will be tuned in real-time based on the current total generation and the current spinning reserve in Area i . That is, the smaller the current spinning reserve (relative to the total generation) in Area i , then the lower the threshold value for Ω_a^{i*} . The computation of the Ω_d^i is then similar to accumulating the integral of $\Delta\delta_c^i$ below a threshold, denoted $\Delta\delta_c^{i*}$. When Ω_d^i grows above a pre-specified value, say Ω_d^{i*} , load shedding in Area i may be initiated to mitigate the disturbance event.

We next illustrate the above algorithm in the Kundur two area system [14] (the diagram of the two area system is shown in Appendix A). The system is simply divided into two areas with Gen 1 and Gen 2 in Area 1, Gen 3 and Gen 4 in Area 2, respectively. We define

$$\delta_c^1 = \frac{\delta_1^1 P_{G1} + \delta_1^2 P_{G2}}{P_{G1} + P_{G2}} \quad (1.5)$$

$$\delta_c^2 = \frac{\delta_2^3 P_{G3} + \delta_2^4 P_{G4}}{P_{G3} + P_{G4}} \quad (1.6)$$

where δ_1^1 , δ_1^2 , δ_2^3 , δ_2^4 are the phase angles of the bus voltage of the four generators, respectively. Then, we get

$$\delta_c = \frac{\delta_1^1 P_{G1} + \delta_1^2 P_{G2} + \delta_2^3 P_{G3} + \delta_2^4 P_{G4}}{P_{G1} + P_{G2} + P_{G3} + P_{G4}} \quad (1.7)$$

$$\Delta\delta_c^1 = \delta_c^1 - \delta_c, \quad \Delta\delta_c^2 = \delta_c^2 - \delta_c \quad (1.8)$$

We apply a three phase fault near Bus 8 and we clear the fault and remove three of the four lines between Bus 7 and Bus 8 after certain time, the details of the simulation results are shown below. When the fault-on time is set to be 0.08 sec, 0.10 sec, and 0.11 sec, the curves of $\Delta\delta_c^1$ and $\Delta\delta_c^2$ are shown in Figure 1-1, Figure 1-2 and Figure 1-3, respectively. Figure 1-4 shows the curve of $\Delta\delta_c^1$ near 60 degrees for the simulation in Figure 1.3.

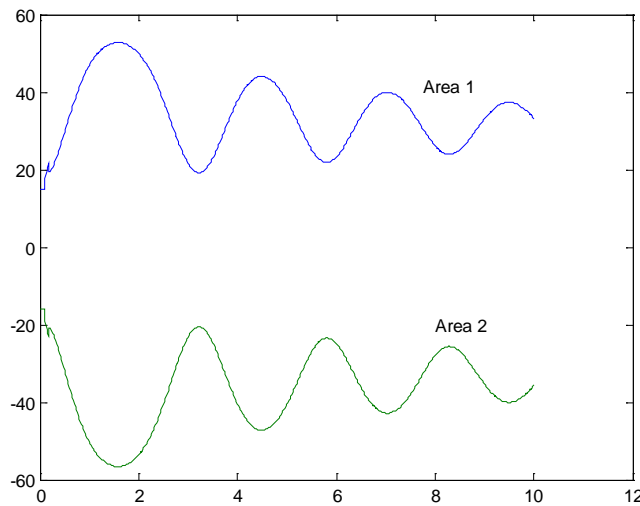


Figure 1-1 Angles of each area (fault-on time=0.08 sec)

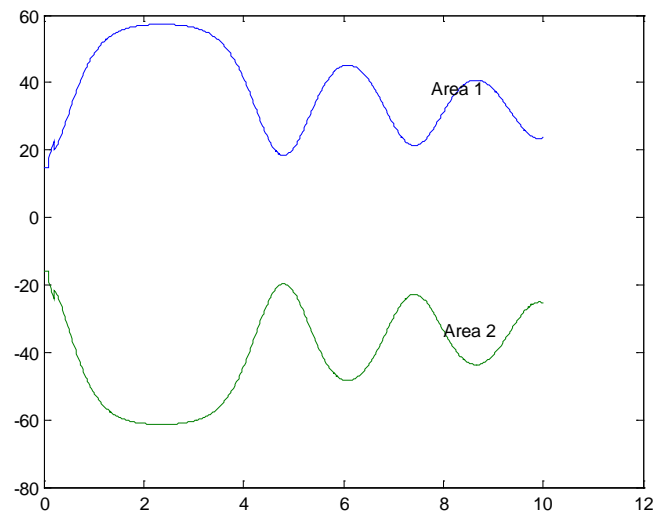


Figure 1-2 Angles of each area (fault-on time=0.10 sec)

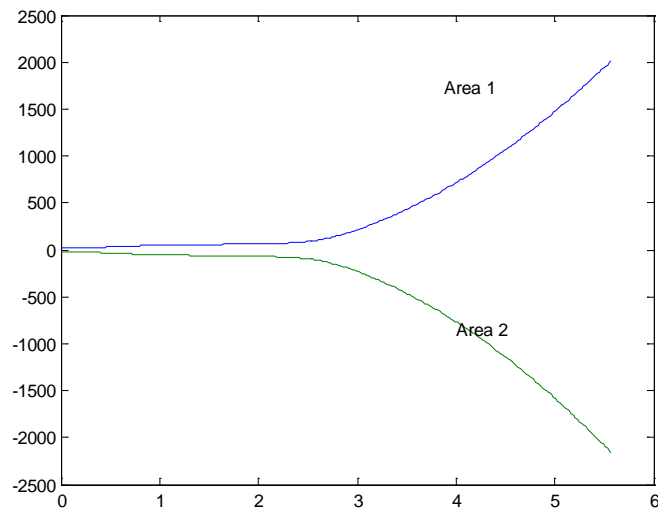


Figure 1-3 Angles of each area (fault-on time=0.11 sec)

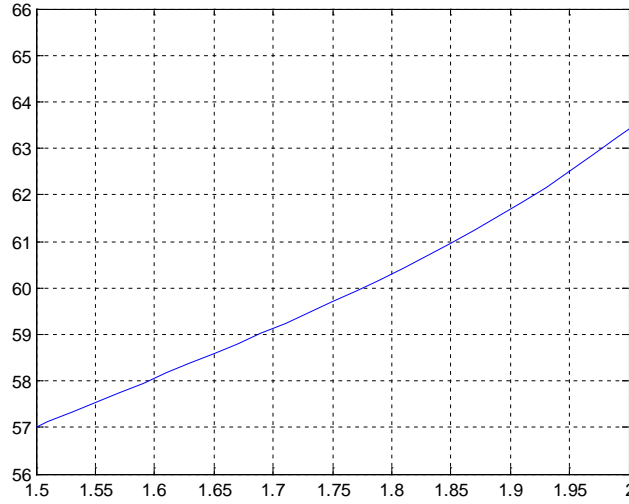


Figure 1-4 Angles of Area 1 (fault-on time=0.11 sec)

From the cases above, we could say that 0.10 sec is the critical fault time for this three-phase fault on Bus 8. Looking into Figure 2-2, we could find that the maximum value of $\Delta\delta_c^1$ is 57.3 degrees and the minimum value of $\Delta\delta_c^2$ is -61.5 degrees for the critically stable case. Therefore, we set the conservative values, $\Delta\delta_a^* = 60$ degrees, and $\Delta\delta_d^* = -65$ degrees. Similarly, we can estimate the values $\Omega_a^* = 5$ and $\Omega_d^* = -5$ from additional studies. Simulation results with different fault-on times are shown in Table 1-1. From the results, we could say Area 1 is moving away from the system earlier than Area 2. When we try to trip some generation of Area 1, we find that the generation tripping action by itself is not enough to stabilize the system. Therefore, we initiate some load shedding action in Area 2 that is decelerating from the center of the system. We trip Gen 1 and 50% of the load at Bus 9 at time 1.83 sec for the second case in Table 1-1. After the control actions, the system can be stabilized. Also, if we trip Gen 1 at time 1.83 sec and 50% load at Bus 9 at time 1.93 sec, the system can still be stabilized.

In Table 1-1, the time duration between T_{start} (the time the phase angle goes above the threshold) and $T_{control}$ (the time the control trigger is issued) can be used to quantify the severity of the disturbance. If the time duration $T_{control} - T_{start} > T^*$, we can interpret the angle instability to be less severe which will be controlled by only generator tripping. Whereas if $T_{control} - T_{start} < T^*$, the instability can be interpreted to be more severe so that both generation tripping and load shedding will be initiated. For the two-area system, we can use a value of say 7 cycles or 0.117 sec for the value of T^* . Further investigation on the tuning of T^* is recommended.

Table 1-1 Simulation results for the two-area system

Fault-on Time (sec)	0.10	0.11		0.12	
Result	Stable	Unstable		Unstable	
Area		Area1	Area2	Area1	Area2
T_start (sec)		1.73	1.89	1.52	1.61
T_contrl (sec)		1.83	1.93	1.62	1.69 s
Int		6.05	-5.23	6.10	-5.33
T_unst		2.4 sec		2.0 sec	

T_start is the time $\Delta\delta_a^l$ increases beyond $\Delta\delta_a^{l}$; T_control is the time Ω_a^l reaches Ω_a^{l*} ; Int is the value of Ω_a^l at T_control. T_unst is the time $\Delta\delta_c^l$ reaches 90 degrees.

Table 1-2 summarizes the benefits provided by the algorithm in improving the transient stability. Taking the first case as example, the critical clearing time without the proposed control is 0.10 seconds (the first entry in Table 2-1). The system becomes transient stable for the clearing time of 0.11 seconds as well as 0.12 seconds. With the automatic generation and load tripping control as proposed, the critical clearing time improves to 0.14 seconds. Compared to the 0.10 seconds for the original system with no control, the automatic controller as proposed provides an improved critical clearing time by a margin of 0.04 seconds (2.4 cycles). These simulations illustrate the fact that the controller as proposed is useful for the two-area system in improving the transient stability of the system for critical contingencies.

Table 1-2 Improvement on the system stability

Fault near Bus	Line Removed	Critical clearing time improvement with the control (cycles)
8	7-8	2.4
7	7-8	1.8

Tests in the two-area system lead to some discussions of the new algorithm.

(1) If we use inertia constants to compute δ_c as formula (1.2) shows, with the 0.11 sec-fault time, Figure 1-5 shows the comparison of the two methods. It shows that the

substitution with power output in place of the inertia constant to compute the center of the system angle δ_c is reasonable.

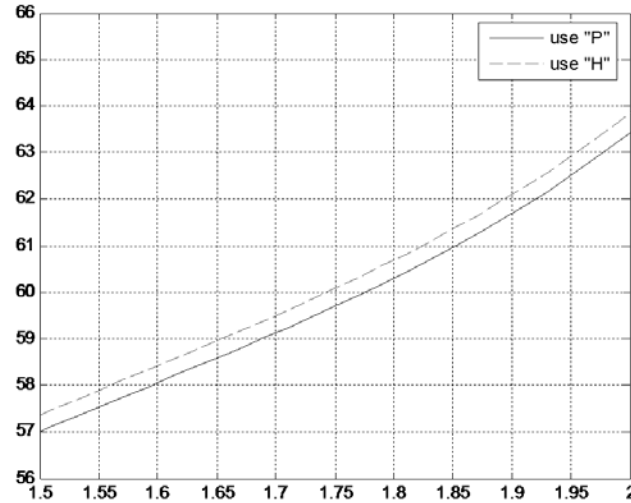


Figure 1-5 Comparison of two methods to compute δ_c (fault-on time=0.11 sec)

(2) The thresholds are set up based on the critical cases and they need to be tuned in order to make the algorithm work reasonably for diverse conditions.

(3) Control actions such as the generation tripping in the accelerating area or load shedding in the decelerating area are the normal methods in system protection. But, the tripping or shedding amounts still need to be determined from further studies in future research works.

Additional simulation results of the algorithm in the 39 bus New England test system can be seen later in the report in Chapter 5.

1.3.2 Algorithm using the Energy Function Concept

Transient energy methods are non linear theoretic techniques for analyzing the interconnected system stability of power system dynamics from swings in generator rotor phase angles. The energy associated with the deviation from system equilibrium point is quantified as a kinetic energy function (KE) that is related to changes in rotor speeds and a potential energy function (PE) that is connected with changes in relative rotor phase angles. In our research, we are trying to establish the relationship between the system transient behavior and the real-time measurements from synchrophasors. The transient energy method is used to analyze the system stability so that PMU based measurements

can be used for detecting the system instability in real-time, and for activating suitable control actions.

Transient energy function methods have a rich history in power system analysis [21-28]. The method to evaluate the transient response of a power system following a large disturbance was proposed in [21-27]. [24-25] used energy functions to quantify the energy of a system disturbance. In 1982, [26] introduced the idea of an individual machine's energy function, and in 1988, Stanton used transient energy function of an individual generator to assess instability of individual sites [26-27]. The Energy Functions are fully described in references such as [24,25,28]. An algorithm using the energy function concept to detect system instability of a transmission tie-line based on PMU can be found in the recent paper [30], where the definition of a critical energy was carried out as a criterion of system stability.

In this report, we apply the energy function concept for a multi-machine power system using heuristic interpretation of the energy function concept as described below. We compute the potential energy as well as the kinetic energy of each machine and define thresholds to decide a) whether the system is progressing towards transient stability and b) to identify the critical generator.

With the energy function analysis, it is possible to compute the swing energy associated with the system disturbances during an event. Also, by using the bus voltage phasor angle and frequency measurements from synchrophasors, it is possible to determine an estimate of the system swing energy in real-time. Thus, the angle separation across the system can be quantified and control actions can be taken to stabilize the system. In [28], the critical energy of each generator in the system is predetermined by the off-line computations. In real-time simulation, the computation of the kinetic energy function of each generator is used to detect whether the generators will remain in synchronism. The recent paper [30] proposed a synchrophasor data based energy function analysis in typical power transfer path with two generators.

In our research, we carry out the potential energy function together with the kinetic energy function to define the total energy of each generator in the system in the spirit of [26]. We introduce heuristic approximations to make the computation of the transient energy easy to implement in a real-time synchrophasor environment. Computation of both potential and kinetic energy functions in real-time is used to detect the system instability for the large power system with no restrictions on the size of the system or on the number of generators.

Algorithm

A partial energy function is one that computes the transient energy of a single generator (or subsystem) in a multi-machine power system. In partial energy function analysis, we interpret the potential energy for generator i as the integral of the power accelerating the generator's rotor,

$$PE_i = \int_{\theta_{i_0}}^{\theta_i(t)} (P_{G_i} - P_{T_i}) d\theta_i \quad (1.9)$$

Similarly, the kinetic energy of machine i is interpreted as

$$KE_i = H_i (\omega_i - 1)^2 \quad (1.10)$$

where

ω_i = rotor speed of the generator

H_i = Inertia time-constant of the generator

P_{T_i} = Mechanical torque

P_{G_i} = MW generation of the generator

θ_i = rotor angle

Next, we approximate the computation for the high side synchrophasors measurements as follows. The rotor angle is approximated by the high side bus voltage phase angle like in Section 1.3. (The same approximation applies for the rotor frequency). The MW power generation is approximated by the MW high side power injection on the transmission line feeding the bus. The machine torque P_{T_i} is approximated by a moving time-window average of this high side power injection. We assume that the system is operating at the pre-contingency stable equilibrium point at the start of the contingency and that the potential energy is measured with respect to the pre-contingency equilibrium state. This is again approximation of the standard definition of potential energy where it is usually defined with respect to the post-contingency stable equilibrium point. Inertia constant H_i is varied proportional to the steady-state power injection. We define the total energy of each generator as TE_i where,

$$TE_i = KE_i + PE_i$$

Now, we simply use TE_i to analyze the stability of the system by observing whether TE_i values are remaining bounded. Simulation results of the algorithm in the 39 bus New England system will be discussed in Chapter 5.

1.3.3 Algorithms based on Action Principle

Principle of Least Action

Principle of Least Action is a powerful conceptual platform for analyzing the dynamics of physical systems such as the power system. The traditional transient stability analysis in the power system has been based on Lyapunov theoretic principles, which emphasize the conservation or dissipation of the total energy of a system. In contrast, there is an alternate philosophy for deriving the dynamics of physical systems, which are based on the notion of Action.

Action is defined as the time integral of the Lagrangian, L , where $L = KE - PE$, is defined as the difference between the Kinetic Energy and Potential Energy. Hamilton's Least Action Principle states that the system follows that specific trajectory that corresponds to the minimum action among all possible trajectories. Hamilton's principle [31] is a classical concept in Physics, and it has received much attention in the recent Physics literature as an alternate candidate to Newtonian laws of Physics in textbooks [32]. In this section, we postulate that the Action Principle may be inherently suited for real-time analysis of angle stability in power systems.

Specifically, as noted by many authors in recent Physics literature (e.g. [32]), Hamilton's Least Action Principle is somewhat misunderstood in that the Action for a system trajectory may not always be a minimum among all possible trajectories. There are instances, when the Action for a system trajectory may be a saddle point among all possible trajectories [32]. That is, Action of a system trajectory may be a minimum along some directions while being a maximum among other directions. It has been postulated that the Action of a physical system trajectory can never be a maximum among candidate trajectories.

In our power system context, the definition of Action (also called Effort by some physicists including Euler) is inherently suited to real-time analysis in that Action or Effort is a time-integral of the Lagrangian. In this paper, we prefer the terminology Effort in place of Action for the integral because we show that the term has a direct physical relevance.

Specifically, we define Effort as

$$EFF = \int_{t_0}^t L dt = \int_{t_0}^t (KE - PE) dt \quad (1.11)$$

As noted earlier, KE can be computed from the speeds of individual machines and potential energy from the sum of potential energy from each machine. That is,

$KE = \sum KE_i$ and $PE = \sum PE_i$. Therefore, the Lagrangian $L = KE - PE$, naturally divides into $L_i = KE_i - PE_i$. We can also decompose the effort EFF into $EFF = \sum_i EFF_i$ where EFF_i is the time-integral of the machine Lagrangian L_i .

The principle of least action is a theoretic tool that is used in physics to predict the system response among many possible trajectories of a model. In our application, we want to use the concept to analyze the real-time trajectory of the power system as observed from synchrophasors to *predict whether the trajectory is leading to a stable response or an unstable response*. The power system application is motivated by two heuristic interpretations of the classical Action principle:

We assume that the Action or Effort for a trajectory depicting a stable response (that converges to an asymptotically stable equilibrium point) is fundamentally different from that of an unstable response (that results in divergence). Specifically, in the context of power system, we assume that the Effort computed as defined above for a transient stable response remains bounded while the Effort computed for a transient unstable response becomes unbounded in some sense. *This motivates us to develop upper thresholds for Effort along trajectories which are used to predict the emergence of unstable system responses.*

Action Principle implies that the system dynamics is along the path of least action or least effort. Therefore, by examining the efforts of individual generators (or components of a system), we postulate that the generators showing the largest effort are the most likely candidates to push the system to an unstable response as compared to the other generators. In other words, since the total effort EFF has to be kept at a minimum, large values of EFF_i by a few generators imply that the other generators have to work that much harder to keep the total effort at a minimum. This motivates our control principle that *when the system is predicted to be going unstable, tripping of generators exerting the largest Effort values will help enhance the overall system stability.*

In the following sections, we show that the two concepts 1) and 2) proposed above appear to work well in power system simulation test cases. In the following

simulations, kinetic and potential energies of machines are calculated using the heuristic approximations summarized in Section 2.2. We can then compute the Lagrangian as the difference $L=KE-PE$, and proceed to evaluate the Effort EFF as the time-integral of Lagrangian L as in equation (1.11).

2. TRANSIENT ENERGY FUNCTIONS

2.1 Introduction

The use of transient energy functions in determining stability has shown promise as seen from previous research [1]. Transient energy functions are a means of estimating the energy in a system. Knowing the energy allows us to understand the behavior of a system without having to run time-domain simulations to determine if the trajectories are stable. Since the trajectories, rotor angle and frequency, are referenced on a center of inertia then the energy is also referenced the same. This makes identifying the critical generators significantly easier since we can directly see if they are accelerating or decelerating away from the rest of the system. We will further assume that the energy of each generator is initially zero for the start of each simulation. This has been shown to be a reasonable assumption in previous work [1][5]. Simulations on the 39 bus system have also shown that the energy changes insignificantly from load changes compared to the energy from sustained faults making any small deviations from the initial energy from zero irrelevant.

2.2 Formulation

To start off the definition of center of inertia is re-stated here. The definition of center of angle using the generator inertia H is given by the following,

$$\delta_{COA} = \frac{\sum_{i=1}^N \delta_i H_i}{\sum_{i=1}^N H_i}$$

In theory the inertia H is computed for each generator and is therefore ready to use for real-time computation. However the generator at a given bus might represent an equivalent group of many generators, in this case making the exact calculation of H for that equivalent generator difficult to compute. A scenario that makes using H difficult is where generators within a plant are committed or de-committed as load changes throughout the day. A new approach using the scheduled power output is used as a weighting in the center of angle was proposed in [19]. The new center of inertia is given in equation 2.1,

$$\delta_{COA}^k = \frac{\sum_{i=1}^N \delta_i P_{T_i}}{\sum_{i=1}^N P_{T_i}} \quad (2.1)$$

In 2.1 δ_i is the bus voltage angle estimate of the rotor angle for the i^{th} generator in area k . For a system represented as one single area, the center of inertia is computed using all the generators online. Once the center of inertia is computed, we then reference the rotor angles to it as shown in 2.2.

$$\theta_i^k = \delta_i^k - \delta_{COA}^k \quad (2.2)$$

The rotor frequency is computed on the center of inertia frame of reference in the same way. This is shown in 2.3 and 2.4,

$$\omega_{COA}^k = \frac{\sum_{i=1}^N \omega_i P_{T_i}}{\sum_{i=1}^N P_{T_i}} \quad (2.3)$$

$$\tilde{\omega}_i^k = \dot{\delta}_i^k - \dot{\delta}_{COA}^k \quad (2.4)$$

To understand the transient energy function better, let us look at the swing equations of the synchronous generator defined on the center of inertia given in [1],

$$M_i \ddot{\omega}_i = P_{mi} - P_{ei} - D_i \tilde{\omega}_i \quad (2.5)$$

Equation 2.5 tells us the acceleration, or deceleration, due to the mismatch between mechanical power P_{mi} on the shaft and the electrical power P_{ei} which opposes it. The damping D_i is assumed to have a negligible effect on the first swing and therefore is set to zero. Another term appearing on the right hand side of 2.5, $-P_{COA}^k$ is used in [1][5] which relates the power mismatch to the center of inertia power mismatch, however the swing equations used in this research will neglect this.

To relate the swing equation 2.5 to energy it is necessary to describe the fundamental relation between work, energy and power. Knowing the force acting on a body tells us the acceleration of that body by Newton's equation $F = m * a$. The torque that causes a body to rotate is proportional to the force by the distance from the center of mass. Noting that the swing equation essentially tells us the net torque on the generator shaft we can then state that it is proportional to a net force. Taking the first integral of motion of the swing equation then gives us work. Work is merely the change in kinetic energy of the system, and since energy is conserved this is also equal to the change in potential energy.

The mathematical derivation given in [5] is similar but instead of multiplying 2.5 by δ to get Work, i.e. $W = \tau * \theta$, we use the time derivative of delta $\dot{\delta}$ giving us power instead of work. This is done to make the integration easier. Integrating with respect to time gives us the work, which is equivalent to energy. Deriving the energy in this fashion makes integration easier since we know that $\dot{\delta}$ is equivalent to ω . Integrating 2.5,

$$\int (M_i \dot{\omega} - P_{mi} + P_{ei}) \dot{\delta} * dt = \int M_i \frac{d\omega}{dt} \omega * dt - \int (P_{mi} - P_{ei}) \frac{d\delta}{dt} * dt$$

Looking at the first integral term on the right hand side, we see that this is merely the chain rule used in differentiation so integrating this gives us $\frac{1}{2} M_i \tilde{\omega}^2$. For the second term we see that dt cancels out so we are left with the integration with respect to angular displacement δ . At this point it, should be mentioned that Equation 2.5 was arranged such that $0 = M_i \dot{\omega} - (P_{mi} - P_{ei})$. Integrating the term (zero) gives us a constant representing the total energy of the system which satisfies the theory of energy conservation. The transient energy function representing a single machine is given by equation 2.6,

$$TE_i = \frac{1}{2} M_i \tilde{\omega}_i^2 - \int_{\delta_s}^{\delta} (P_{mi} - P_{ei}) d\delta \quad (2.6)$$

2.3 Lyapunov's Methods

The premise that transient energy functions are suitable for determining stability of a system is based on Lyapunov's Theorems of stability. Of particular interest is Lyapunov's second method. The second method is based on finding an equation that tells us the behavior of the trajectories without explicitly integrating the differential equations which is computationally tedious. From the point of angle stability this means that the Lyapunov equation gives sufficient conditions on when the rotor angle and rotor frequency trajectories are asymptotically stable in the sense that they return to a stable equilibrium point. The Lyapunov function will be denoted as $V(x)$ in keeping with the traditional notation.

For a function to be considered as a Lyapunov function it must be shown that the following characteristics apply [2],

The function $V(x)$ and its first derivative with respect to time, $\dot{V}(x)$, are continuous within a bounded region Ω .

$V(0) = 0$, $\dot{V}(x) < 0$ (negative definite)

$V(x)$ is positive and bounded within a region Ω surrounding the stable equilibrium point.

There are many variations to this result in practical applications based on the specific aspects of the nonlinear systems being considered. It can be argued as shown in [1], [5], that the transient energy function satisfies these conditions making it a suitable Lyapunov function. The third criterion has been shown to be heuristically true through simulation results as stated in [5]. The second criterion is easily verified by inserting the equilibrium points $\omega_i = \omega_s$ and $\delta_i = \delta_s$ into 2.6.

The main problem in our real-time approximations of transient energy functions based on voltage angle measurements is with the first criterion, that the estimated rotor angle and frequency be continuous. Any type of network changes will cause discontinuities in bus voltage angles and magnitudes. For instance, a line tripping can result in a sudden change in voltage angle differences especially if it is related to a main tie-line. Faults close to any generator will lead to an even larger discontinuity. As a practical solution to this problem, a low pass filter is suggested on the synchrophasor measurements.

2.4 Implementation

The online implementation of the transient energy function is assumed to be done through SCADA (Supervisory Control and Data Acquisition). SCADA gives the control operators a way to monitor the power flows and voltage levels in a system. Traditionally this was done with state estimators but for convenience we will assume that the synchrophasor's measurements monitoring the output of each generator are used instead. This is a reasonable assumption since the generator output is metered anyways. When implementing the transient energy function we compare the computed energy with the known critical amount of energy. If the maximum energy for a given disturbance is less than the critical energy required for the machine to lose synchronism then it is stable. If the machine goes above this limit then it is unstable. For the case where a group of machines beginning to lose synchronism we take the machine that takes the shortest amount of time to go beyond its critical energy limit as the candidate machine where generation shedding should occur.

The critical energy is found through simulating a sustained fault with duration equal to the critical clearing time near the generator of interest. The following example shows the calculation of the critical energy for Generator 4 on the 39-bus 3 Area power system under heavy loading conditions. The maximum total energy for the generator is shown in Figure 2-1,

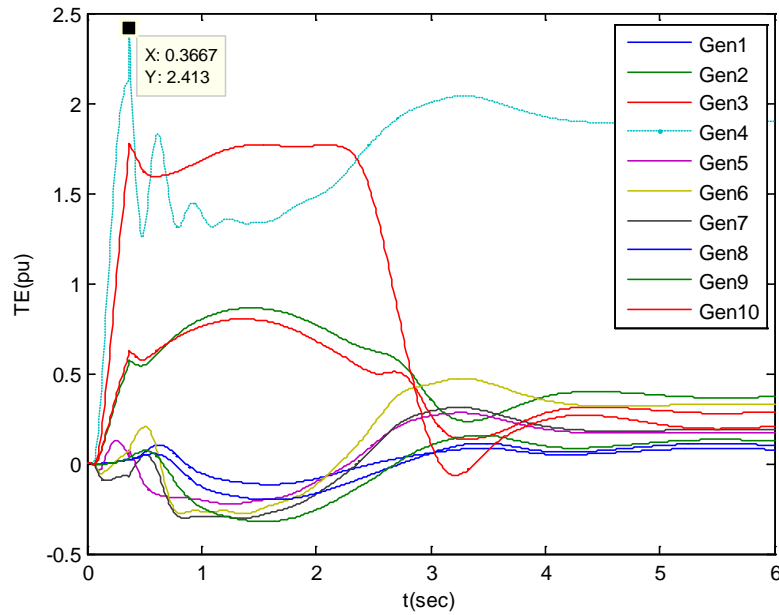


Figure 2-1: TE Threshold Gen4

The total energy of Generator 4 is depicted in Figure 2-1 as the dotted line. The maximum total energy that is reached is 2.41 pu. Looking at Figure 2-1 we see that the total energy does not go to zero. The reason for this is that we are integrating from the pre-fault equilibrium point, not the post-fault equilibrium point. To know the post fault equilibrium point, we would need to do transient simulations for all possible faults, which is impractical for any reasonably sized system. We can see that the total energy remains bounded so it is considered stable even though the second Lyapunov condition is not entirely met. Examining the kinetic energy, we see that it does go to zero as shown in Figure 2-2.

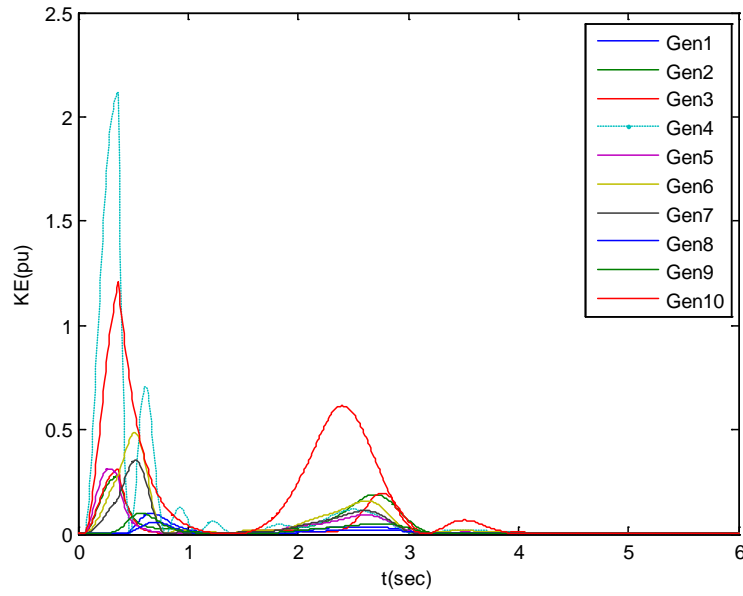


Figure 2- 2: Kinetic Energy Gen 4

When all of the kinetic energy is converted to potential energy, we can say that the system is stable. This can be misleading since in power systems we consider a generator to be unstable when pole slipping occurs. Pole slipping is a phenomenon that we wish to avoid since it causes damage to the synchronous machine and other equipment. In reality there are protection schemes to prevent the machine from pole-slipping, so assuming the machine will trip we need to determine at what point we need to shed generation to prevent the generator from going offline completely.

In Figure 2-3, it is evident that the potential energy stops increasing as the kinetic energy is converted into potential energy. Let us look at the case where Generator 4 remains in synchronism with the system but other generators do not. In Figure 2-4, we observe that the total energy of Generator 4 does not exceed 2 pu, or come close to it.

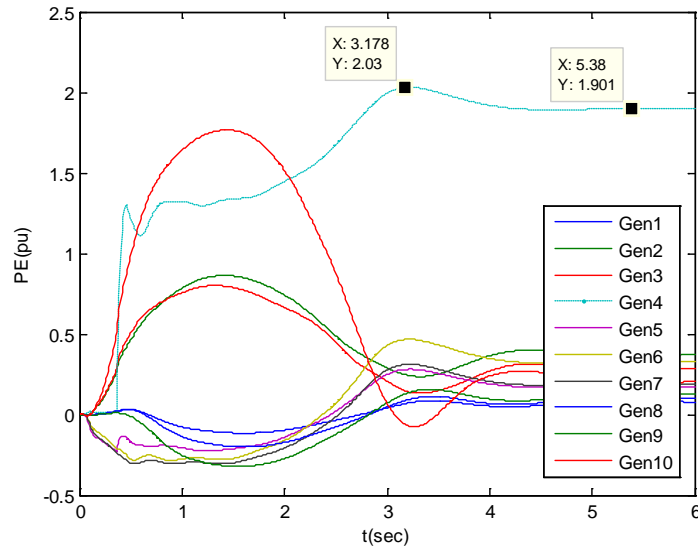


Figure 2- 3: Potential Energy Gen4

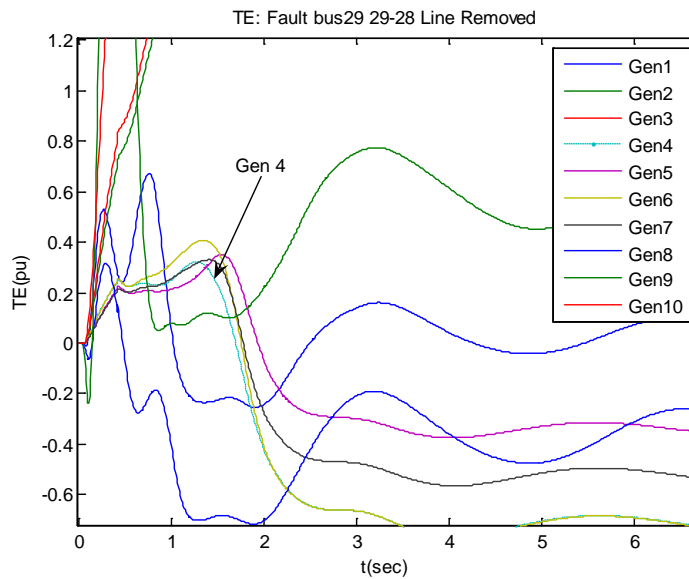


Figure 2- 4: Gen 4 Total Energy, Fault Bus 29

Generators 2, 3, and 10 diverge from the rest of the system where Generator 4 remains in synchronism. Another point that should be made is that the total energy of Generator 4 settles down to a value less than zero whereas the unstable generators do not. In this case, the unstable generators, those located in Area 2 in Figure A -1,

decelerate since the Generation in Area 2 is not sufficient to supply the entire load in that area.

2.5 Conclusions

Determining the stability of a power system using total energy has its challenges. The most notable is that it is slow in determining the critical generators. The results section of this report compares the total energy algorithm with the angle, Lagrangian, and Effort. Here we see that the angle algorithm proposed in [19] is more suitable for use in determining the critical generators since it is much faster than the total energy algorithm.

Compared with the Lagrangian we see that it is slower to respond. One of the major differences lies in the fact that the kinetic energy is at a maximum on the largest swing when the potential energy is at its highest absolute value. Since the kinetic energy is squared, it doesn't tell us if the generator is speeding up or slowing down. So looking at the potential energy we see that when it is most negative, it must be at a higher rotor angle, thus accelerating. Thus negating the potential would mean the Lagrangian would be greater at this point than the total energy. At this point the Lagrangian would be at a maximum whereas the total energy is not, making the Lagrangian a faster algorithm for detecting the instability. Looking at the case where the fault is near the generator we see that the kinetic energy plays a much more significant role than the potential energy during the fault on case. For faults electrically farther away this is not the case.

3. LAGRANGIAN AND EFFORT

3.1 Introduction

The Lagrangian gives us the difference rather than the sum of the energy components. By integrating this difference over time, we find the Action, or Effort. Apart from its use as a clever way to find the Newtonian equations of motion, it has no apparent physical meaning. Since we integrate it to find the Effort, we can simply think of it as the “density” or “intensity” of Effort. The Lagrangian is applied in the same manner as the total energy and as such, we treat it like a Lyapunov function purely for experimental purposes.

The Effort on the other hand represents the minimal amount of action that the system takes from one point in time to another. This is difficult to determine since data on whether or not a line was tripped due to a fault may not be available. We first test the system assuming we know these times, and then we implement a new approach by comparing the Lagrangian of the whole system.

3.2 Formulation

Looking at the difference between the kinetic energy, and potential energy we form the Lagrangian as shown in 3.1,

$$L_i = KE_i - PE_i \quad (3.1)$$

Where KE and PE are the kinetic and potential energy of the i^{th} generator computed in real-time as in 2.6. The Effort is then computed by 3.2,

$$E_{\text{effort}_i} = \int_{t_1}^{t_2} L_i dt \quad (3.2)$$

The integration limits from t_1 to t_2 represent the time frame in which the Effort of the system is of interest. This time frame is represented as the fault on time for transients dealing with faults.

A new way of determining t_1 and t_2 is by looking at the system wide Lagrangian, which is simply the sum of the Lagrangians evaluated for each machine. From simulations it is seen that small changes in load, say +/- 5%, have little effect on the total energy of the system. The effects on the Lagrangian are therefore negligible. A good question to ask is at what point we should declare the system to be in a state of contingency. The short answer to this lies in good engineering judgment at this point rather than mathematical formulation. Further research is needed for theoretical analysis.

From simulation on the 39 bus test system, it was found that a value of around 0.2 pu energy indicated severe problems with the system. A justification of using 0.2 pu of energy is shown below where we examine an unstable fault scenario and a stable case where load is changed in the system.

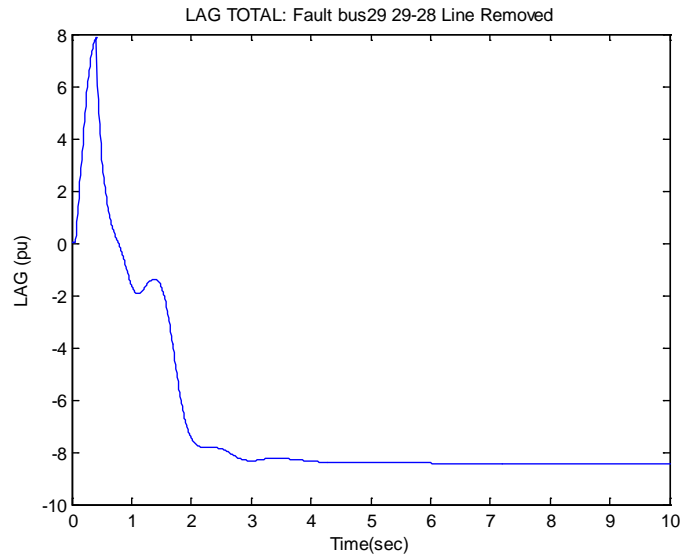


Figure 3- 1: System Lagrangian, Unstable Fault Case

In Figure 3-1 we see that the Lagrangian reaches a maximum of about 8 pu indicating a large disturbance has occurred. For a load change in the system we see in Figure 3-2 that 0.2 pu is a more conservative threshold.

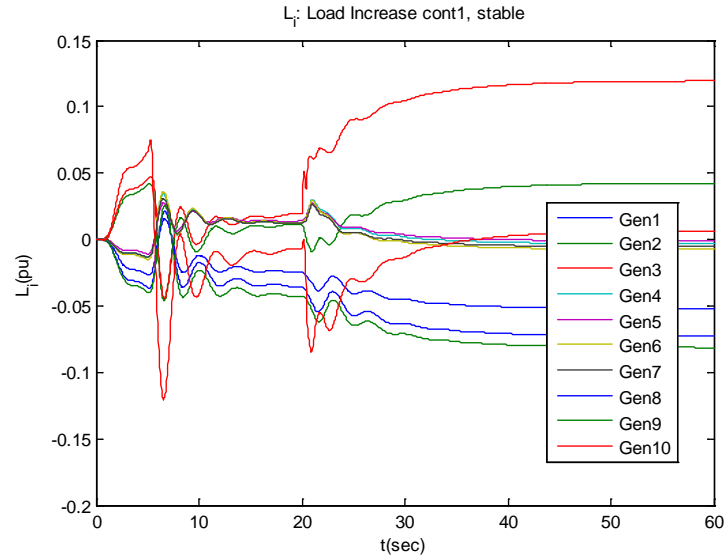


Figure 3- 2: Computation of Lagrange for each generator, no fault simulated

From Figure 3-2, we observe that the Lagrangian for the most effected generator goes to about 0.15. Looking at the sum of L_i over all the individual machines, we see that this sum stays close to zero as shown in Figure 3-3.

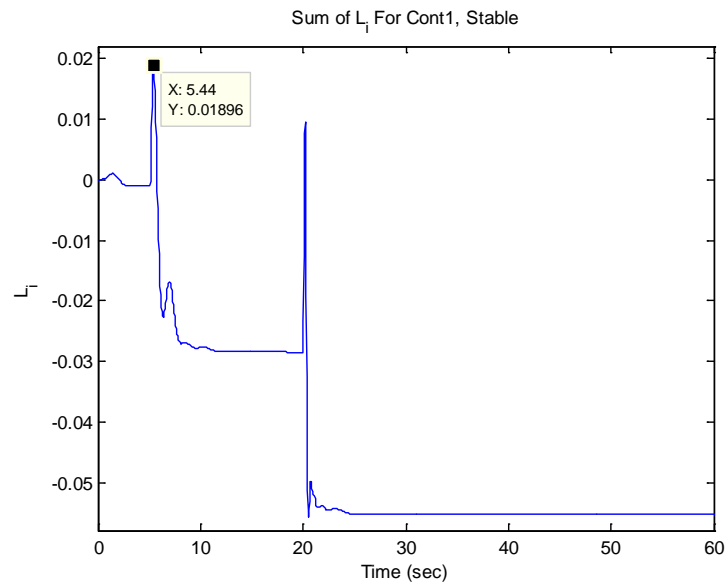


Figure 3- 3: Sum of Lagrangians for Cont1, Stable

Knowing t_1 allows us to define the starting point for the Effort. Let us call this sum TL. Let TL be computed as follows in equation 3.3,

$$TL(t) = \sum_i L_i(t) \quad (3.3)$$

Equation 3.3 is the same as finding the total energy of a system as described in [7] except we use the Lagrangian.

To determine the ending time t_2 we look at the behavior of TL. If TL is decreasing then the phase angle and frequency must be decreasing. At this point, we can conclude that the critical generators are regaining synchronism with the system. If the Effort of the critical machine exceeds the critical amount needed to lose synchronism within the time frame from t_1 to t_2 then the generator is unstable. If Equation 3.3 begins decreasing before the maximum amount of Effort has been exceeded then we can not say for certain whether the machine will lose synchronism.

3.3 Implementation

To determine the efficiency of the Lagrangian and Effort algorithms we will look at two cases. The first case will include a fault and the other an overloaded system will be simulated with no fault. For the faulted cases the system is stable with regard to +/- 5% load fluctuations. The fault is applied long enough for the system to lose synchronism. The method described above in determining t_1 and t_2 for use in 3.2 is compared with the method where we assume we know t_1 and t_2 for a given fault. For simplicity, let us refer to these as method 1 and method 2 respectively. The overloaded system will be analyzed using method 1. A thorough investigation of the Lagrangian and Effort algorithms is left for the results and comparisons section of this report.

For the following fault case, a three phase fault is simulated at bus 4 in the system shown in Figure A-1. Observing the estimated rotor angle, defined on the COI reference frame, in Figure 3-3 below we observe that Generator 3 is the critical generator.

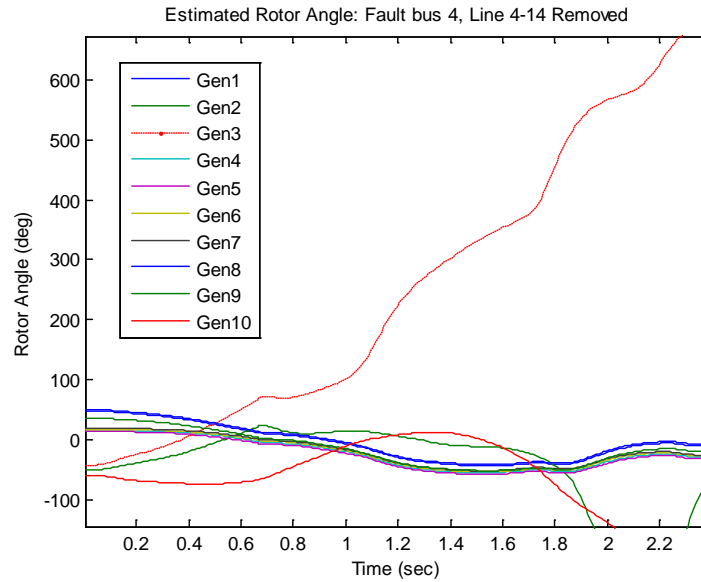


Figure 3- 4: Estimated Rotor Angle from Bus Voltage Angle Measurement

At about 2 seconds, we see that Generators 2 and 10 begin to decelerate from the center of inertia. Area 2, shown in Figure A-1, is clearly losing synchronism with the rest of the system. Computing the load ratio for each area in the system we see that Area 2 has the highest, as shown in Table 3-1 below, thus we shed load at Area 2.

Table 3- 1: Load to Generation Ratio, 39 Bus 3-Area System

Load To Generation Ratio: 39 Bus 3-Area System			
	Area1	Area2	Area3
Load _i (MW)	1647.8	3433	2011.97
Gen _i (MW)	2094.7	2496	2674.3
Load _i / Gen _i	0.787	1.375	0.752
R _{L/G}	0.2268	0.4725	0.2769

Determining how much load and generation to trip to make the system stable depends on several factors. Being able to trip generation and load quickly helps in mitigating the angle instability thus the control action time at which each algorithm picks up has a significant effect on how much load should be tripped. For longer control times we need to trip more load and generation to make the system stable. Further research is needed on these important issues. Another factor has to do with the tie-line transfer limits. If, for instance, we decide to trip generation and load at Area 2 but the amount of

generation is more than the load then the tie-line connecting Area 2 to the grid becomes more stressed. This problem can be overcome by simply shedding the same amount of load as generation. Using Method 1, the Effort is computed as shown in Figure 3-5.

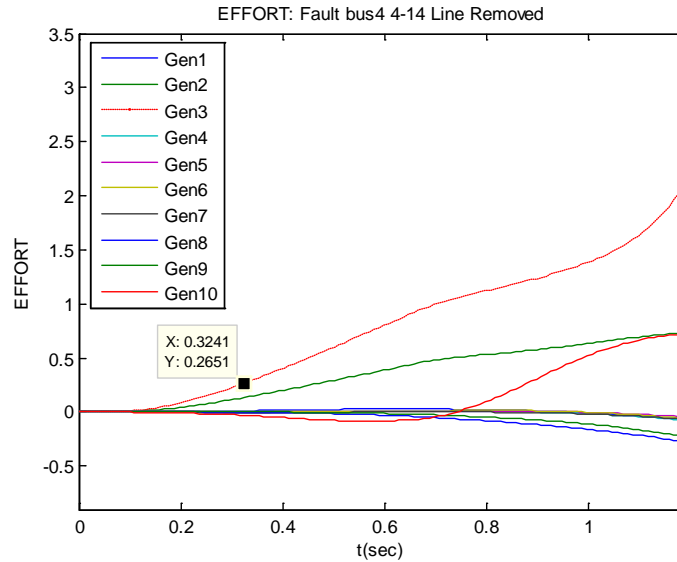


Figure 3- 5: Effort Computed for method 1

At 0.324 seconds, the Effort of Generator 3 exceeds its critical limit. Generators 2 and 10 begin to pull away from the rest of the system but since Generator 3 was the first to be picked up by the Effort algorithm we shed generation there instead of the other generators. If we assume we know the fault duration as described in Method 2 we observe a close approximation with the first method. This is shown in Figure 3-6.

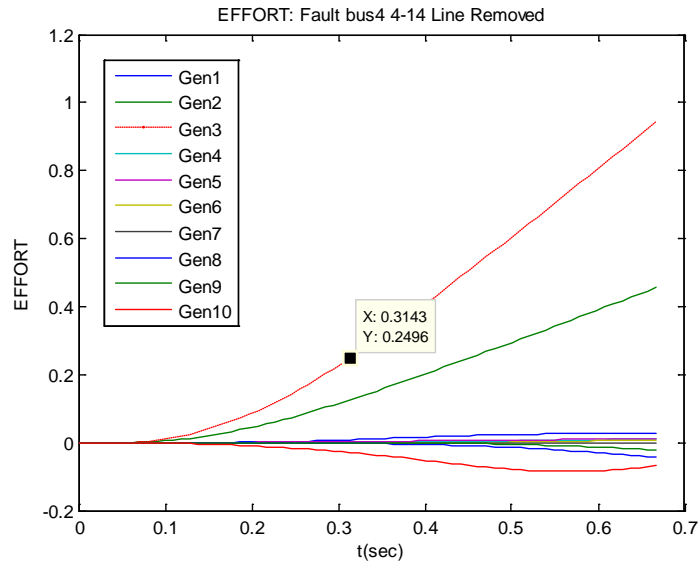


Figure 3- 6: Effort Using Method 2

Comparing Figure 3-5 to 3-6 we see that the time difference in picking up Generator 3 is about 0.01 seconds. Figure 3-7 shows the Effort computation for Generator 3 for both methods.

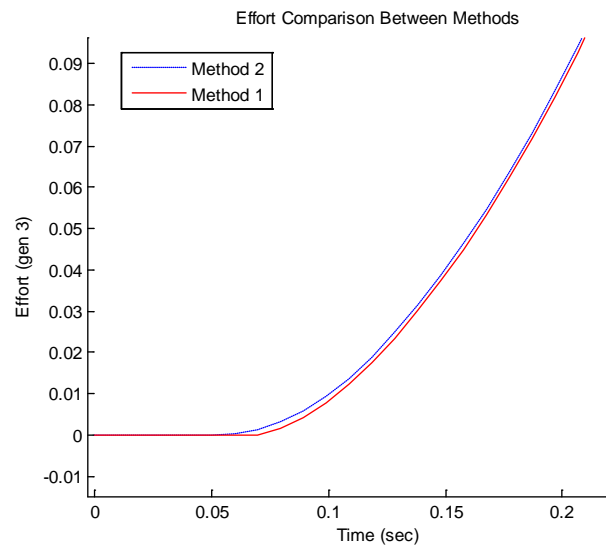


Figure 3- 7: Effort Comparison Between Methods

From Figure 3-7, we see graphically that the two methods give almost identical results with little time delay between the two. Comparing the results from the two

methods for calculating Effort with those obtained from the other algorithms we see that Effort initiates control action the quickest, as shown in Table 3-2.

Table 3- 2: Control Times Comparisons For Fault At Bus 4

Fault Bus 4, Gen 3 Pickup	
	Control Time(sec)
Method 1	0.324
Method 2	0.314
Lagrange	1.057
TE	1.887
Angle	0.657

3.4 Determining Stability Limits

For the Lagrangian, the limits are determined in exactly the same way as with the total energy. A sustained fault is simulated up until the critical clearing time and we find the maximum value that the machine can withstand. This process is shown in Figure 3-8.

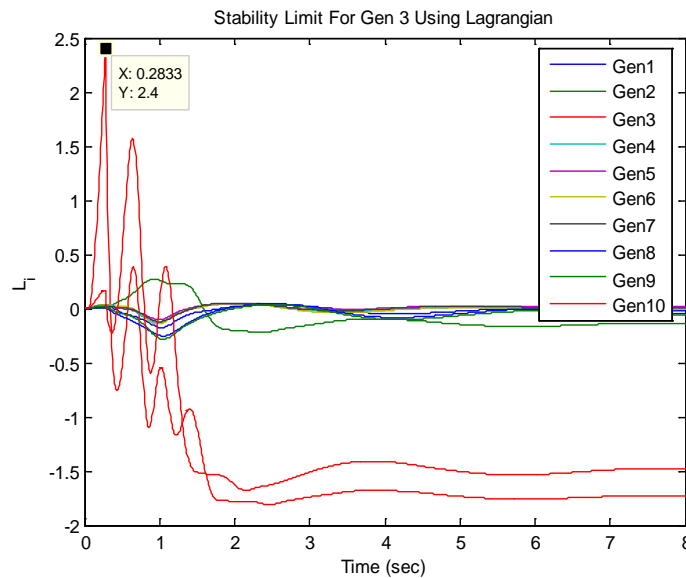


Figure 3- 8: Gen 3 Lagrangian Stability Limit

To find the stability limits as given by the Effort, we use the second method. Since we are looking at the simulations to find the limits we can easily determine t_1 and

t2. For the following simulation shown in Figure 3-9, t1 is 0.05 seconds and t2 is the critical clearing time at 0.283 seconds.

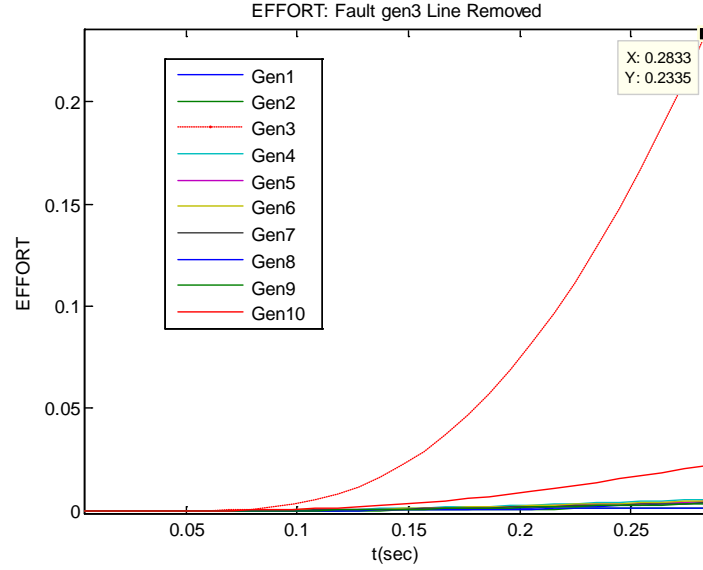


Figure 3- 9: Gen 3 Stability Limit Using Effort

To find the critical Effort for each generator, we look at the Effort computed for the fault on time duration. For Generator 3 we would set this limit to 0.233 as shown in Figure 3-9. This procedure is fairly accurate in determining the limits as long as the loading in the system stays within a reasonable level for which the thresholds were computed on. For changes as much as 20 percent of the total load demand, we need to find a new set of thresholds. In the results section, we look at three load levels, light, medium and heavy and compare the results between each.

3.5 Conclusions

The Lagrangian appears to be a good measure of stability. Its use in determining instability seems to be comparable to the other algorithms and even indicates instability faster than the total energy. Since both frequency and estimated rotor angle data is available in real-time from PMU's, it can be quickly computed. For the computation of the energy components, it is necessary that the data be continuous. Any discontinuities can have an impact on the computations resulting in incorrect control actions. Filtering the data using a low pass filter helps in reducing the effects of any discontinuities and has been shown to have only a minor impact on the speed of detecting angle instability.

Although tripping the same amount of generation as load is a good way to insure that the transfer limits are not exceeded, it may not be optimal in terms of lost revenue. After all, tripping less load while shedding more generation would lead to less revenue being lost. A sensible question to ask is how we can lower the amount of load tripped and at the same time maximize the amount of generation tripped in order to keep the system stable. Load shedding schemes developed in [9][10][11][12] along with countless others deal with optimizing load shedding. A lot of these schemes are well suited for special cases but not for large power grids like the eastern interconnection.

Overvoltage is also a key issue in load shedding. In the August 2003 blackout load shedding actually made the situation worse due to the overvoltage conditions causing overvoltage relays to trip. By tripping less load or by splitting up the amount to trip over a period of time would have alleviated the overvoltage conditions. For simplicity, it is assumed that overvoltage is not a problem with regards to testing the algorithms. In future research, this issue should be studied in greater detail.

4. ANGLE MITIGATION ALGORITHM

4.1 Introduction

The angle algorithm uses a heuristic approach to predicting angle instability based upon observations of the angle trajectories during stable and unstable contingencies. When the rotor angle trajectory exceeds the critical angle θ_c , w.r.t. center of inertia, we then integrate over time the rotor angle. If this integral remains bounded by some predefined quantity then we say that the system is transient stable [19]. Four thresholds, two for the acceleration and deceleration critical angles and two for their time integrals are required for each generation unit. The physical interpretation of the integral is that it represents the generation reserve. Knowing if this reserve is used up during a disturbance is a good indication of the angle stability of the system. Generators with a higher reserve are generally more stable following disturbances [13].

Several advantages from using the angle algorithm include speed of instability detection as well as ease of implementation. Since all trajectories are measured in real-time through PMU's, we can use the algorithm in real-time as well. The estimation of spinning reserve can be updated by noting the change in active power output which can be computed easily from the synchrophasor measurements. For simulations on the New England 39 bus test systems, we use a fixed threshold for the rotor angle θ_c and its integral denoted as Ω .

Although the angle algorithm is fast, it has shown to be over sensitive as we will see from the simulations. This may be because of the fact that the thresholds need better tuning and because the generation reserves have not been computed accurately enough. For systems of reasonable size, say 50k buses, we would have to use more sophisticated methods to determine the thresholds.

4.2 Formulation

The trigger for initiating the computation of the angle algorithm is given by the maximum deviation from the center of inertia in Equation 2.2. The integral of the rotor angle is denoted by Ω_a and Ω_d for acceleration and deceleration respectively and is computed when the critical angle deviation of Equation 2.2 is exceeded. If θ_i starts decreasing (decelerating) before Ω_a is exceeded then we reset the integral to zero. Conversely if θ_i increases before Ω_d is exceeded then Ω is reset. For the simulations in this report, we set $\Omega_a=2.5$ and $\Omega_d=-2.5$.

4.3 Implementation

The implementation on the New England 39 bus system compared with the other algorithms is covered in greater detail in the Results and Comparisons section. Here we will look at the case for a fault at bus 4 with the transmission line connecting bus 4 to bus 14 disconnected to clear the fault. Let us first examine the estimated rotor angles defined on the COI given in Equation 2.2, shown in Figure 4-1 below, simulated on the 3 area New England system shown in Figure A-1. Load shedding is initiated as described in Chapter 3 where Area 2 is given as the best candidate.

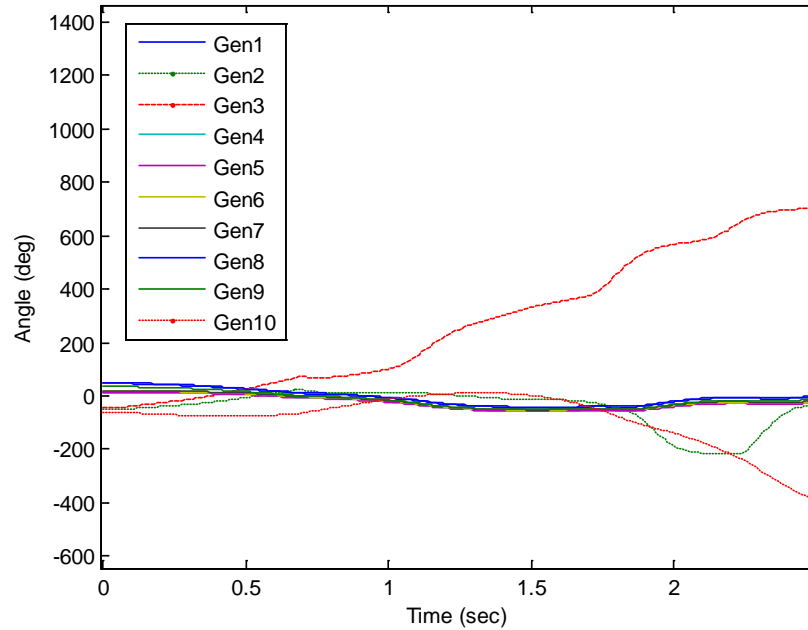


Figure 4- 1: Estimated Rotor Angle From Voltage Angle

The Generators in Area 2 are at first accelerating from the center of inertia however Generators 2 and 3 stay in synchronism with the system for a longer time. Clearly we need to shed load and generation in Area 2 as Figure 4-1 shows. The area where load shedding should occur is not as obvious until about 1.75 seconds. Looking at the load to generation ratio, given in Table 3-1, at the time of generation shedding gives us a good idea of what area to shed load at will have a highest impact on transient stability.

4.4 Conclusions

One of the main issues arising from using the angle algorithm is being able to properly determine the spinning reserves, and thus properly setting the maximum integral limit. This can be accomplished using the operating the real power output and estimating the maximum generation output through offline studies.

Determining the critical groups of generators during a disturbance has been shown for the most part to be one of the strong points of using the angle algorithm, as the results in Chapter 5 will show. The tendency of the angle algorithm to over react is another issue that needs to be addressed in future research.

5. RESULTS AND COMPARISONS

5.1 New England 39 Bus Test System Fault Case

The following tests were done on the original 39 bus system shown in Figure A-2 in the appendix. The thresholds for each algorithm for this case are given in Table 5-1. The maximum limits are given in per unit. In several cases the energy and Lagrange limits are almost identical. For these cases the energy is largely kinetic thus the energy and Lagrangian are almost the same. The spinning reserve integration bounds used in the angle algorithm were set to 2 pu.

Table 5- 1: Unmodified 39 Bus System Thresholds

Thresholds For Unmodified 39 Bus System					
	Lagrangian	Effort	Energy	Angle(deg)	Output(MW)
gen1	11.7463	0.407	12.0478	+/-80°	317.82
gen2	2.5737	0.328	2.5935	+/-80°	760.16
gen3	3.4679	0.428	3.147	+/-80°	826.33
gen4	2.9997	0.476	4.2065	+/-80°	803.45
gen5	1.5347	0.303	1.0928	+/-80°	645.81
gen6	2.101	0.45	2.3051	+/-80°	826.33
gen7	2.589	0.592	1.4071	+/-80°	711.92
gen8	2.6268	0.517	1.5786	+/-80°	686.49
gen9	2.8042	0.156	2.1467	+/-80°	1055.17
gen10	15.8196	1.198	20.0394	+/-80°	1271.28

Table 5 -2, shown below, compares the algorithms between different fault scenarios. Between the Lagrangian, Effort, and angle algorithm we see a strong correlation between algorithms with regards to correctly indicating the most severe generator. In most cases all four algorithms correctly picked up the candidate generator. We can see from the control times that the Lagrangian and energy algorithms are the slowest while the Effort is comparable with the angle algorithm.

With the stable cases we need to make sure that the algorithms do not initiate control actions. The control times are denoted as infinite to indicate that the algorithms correctly classify the system as stable. To be sure that we do not prematurely take control action we compare the Lagrangian, Effort, and angle algorithms to see if all three determine the same generator. Some of the stable cases do pick up stable generators as being unstable but since the other two algorithms did not pick up that generator we do not initiate generation shedding. Let us examine this case. A stable system following a fault at bus 8 with transmission line connecting bus 8 to 9 tripped shows an unstable generator at bus 2. Assuming we know nothing about the stability of the system at that time we

check the output for the other two algorithms and since neither one has confirmed that Generator 2 is unstable we do not hinge. Using the control times given in Table 5-2, we see that the critical clearing times improve, shown in Table 5-3.

Table 5- 2: Control Times For Unmodified 39 Bus System

39 Bus Original System Fault Cases											
Unstable Cases						Stable Cases					
Bus 4 4-14						Bus 4 4-14					
Li		Angle Alg		Effort		Li		Angle Alg		Effort	
2	1.954	2	1.3761	2	1.665	2	2.164	gen2	INF	gen2	INF
3	1.885	3	1.3661	3	1.665	3	2.074	gen3	INF	gen3	INF
Bus 14 4-14						Bus 14 4-14					
Li		Angle Alg		Effort		Li		Angle Alg		Effort	
8	1.083	1	0.7752	9	0.378	5	1.333	2	INF	1	INF
9	0.825	8	0.4969			6	1.443	3	INF	8	INF
		9	0.6261			7	1.373	8	0.33	9	INF
						8	1.333	9	INF		
Bus 5 5-6						Bus 5 5-6					
Li		Angle Alg		Effort		Li		Angle Alg		Effort	
2	1.421	2	0.7951	2	1.034	2	1.63	2	0.75	2	INF
3	1.65	3	1.5703			3	1.829	3	INF	3	INF
Bus 25 2-25						Bus 25 2-25					
Li		Angle Alg		Effort		Li		Angle Alg		Effort	
4	2.333	4	0.339	4	0.568	4	2.773	6	INF	6	INF
5	2.333	5	0.688					7	INF	7	0.88
Bus 2 2-25						Bus 2 2-25					
Li		Angle Alg		Effort		Li		Angle Alg		Effort	
6	1.566	6	1.1567	6	1.396	6	1.815				
7	2.014	7	0.8177			7	1.954				
Bus 16 16-21						Bus 16 16-21					
Li		Angle Alg		Effort		Li		Angle Alg		Effort	
8	2.473	8	0.2985	8	0.995	5	2.333				
9	0.597	9	0.5473	9	0.328	9	0.796				

The critical clearing time improvement varies significantly between different generators as shown in Table 5-3. One reason for this is that the amount of generation shed was set to 50% of the generation active power output which varies by as much as 500 MW as can be seen in Table 5-1. Naturally, the more load and generation removed from the system the less stressed the transmission network becomes. Shedding too much load on the other hand can lead to instability as well so should be avoided.

Table 5- 3: Critical Clearing Time Using Effort Control Times

Fault	Line Removed	CCT (cycles) No Controls	CCT Effort	CCT Angle	CCT Lagrangian	CCT Energy
4	4to14	50	50.8	52.3	51.3	51
14	4to14	32	38.2	38.4	34	34.9
4	4to5	50	50.8	53.1	48	47.6
3	3to4	97	101.12	99	98.2	96.1
4	3to4	50	50.8	52.3	50.6	50.5
5	5to6	41	46.6	45.7	42.7	41.2
6	5to6	37	42.8	43.34	41.1	39.7
2	2to25	51	53.4	54.2	51.9	52
25	2to25	27	39	35	33.2	31
16	16to21	76	76.4	78	76.2	76

5.1.1 New England 39 Bus Test System Overloaded Case

Here we examine contingencies involving high loading in the system along with transmission line and generator outages due to over heating. The unstable cases are examined first. The contingencies were arbitrarily chosen to test the algorithms on various operating conditions. Refer to Table A-1 in the appendix for exact contingencies details. For the first contingency only load increases with line outages are simulated. In these cases, we increase the loading in one area and generation in a different area to simulate an increase in tie-line transfers. Generator 3 is the first to go unstable as can be seen from examining the estimated rotor angles in Figure 5-1 below.

The angle of Generator 3 is the first to increase beyond 90° and the angle algorithm detects instability at about 28 seconds. Generator 2 stays in synchronism with Generator 10 for about 1 second indicating that the load shedding should occur near Generators 10 and 2. We now look at the other algorithms to determine stability. The Effort isn't computed until the total system energy or Lagrangian exceeds 0.2 pu so to determine stability using Effort we must wait a minimum of 27 sec as shown in Figure 5-2. At 27 seconds, we begin computing the Effort until the total energy decreases which occurs at 28.25 seconds. The Effort computed within this time period is shown in Figure 5-3. The Effort of the other 9 generators is negligible compared with Generators 2, 3, and 10. Since Generator 3 exceeds its stability threshold first, we shed generation at that unit. The system Lagrangian and total energy are shown in Figure 5-4 and 5-5 respectively.

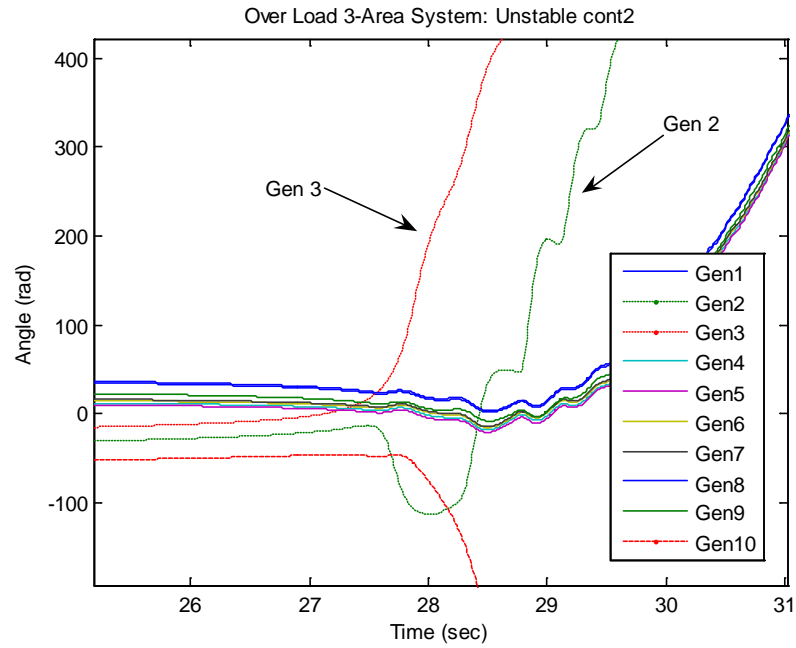


Figure 5- 1: Rotor Angle Estimated From Bus Voltage Angle

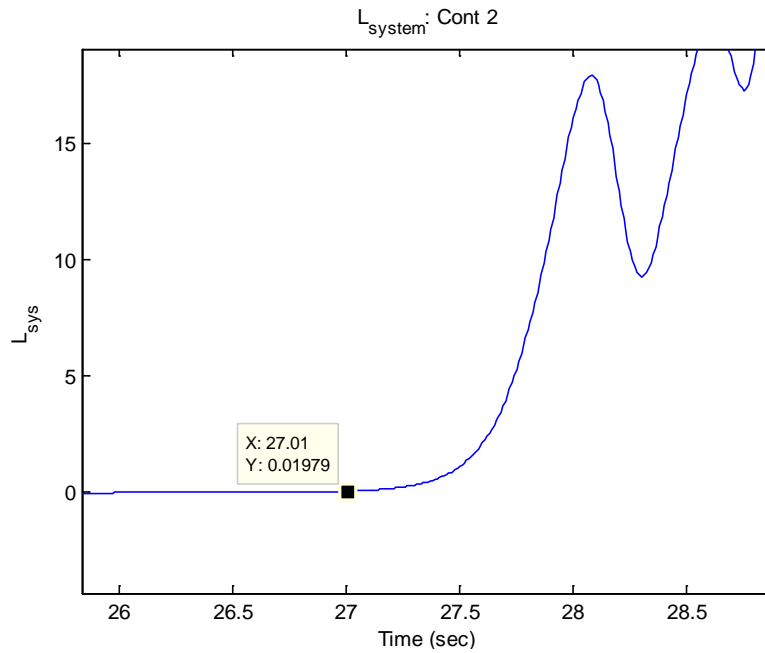


Figure 5- 2: Total System Lagrangian for Unstable Cont2

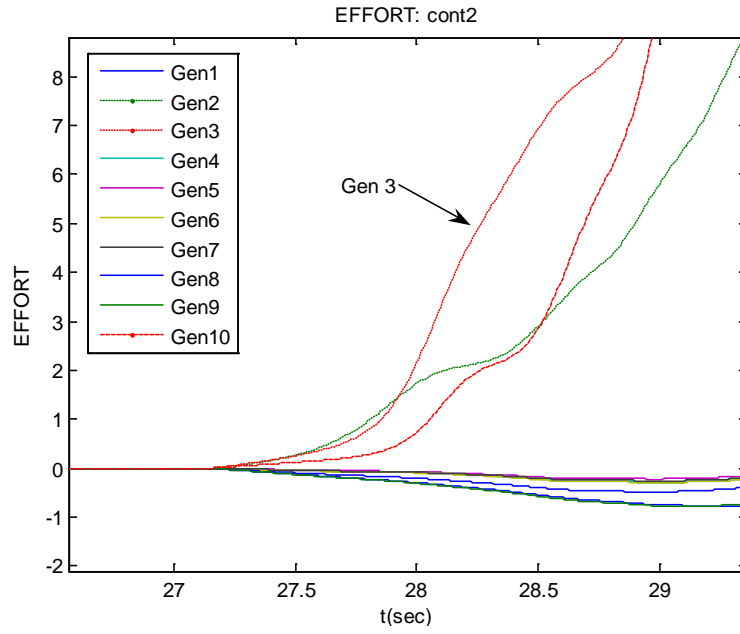


Figure 5- 3: Effort for Unstable Cont2

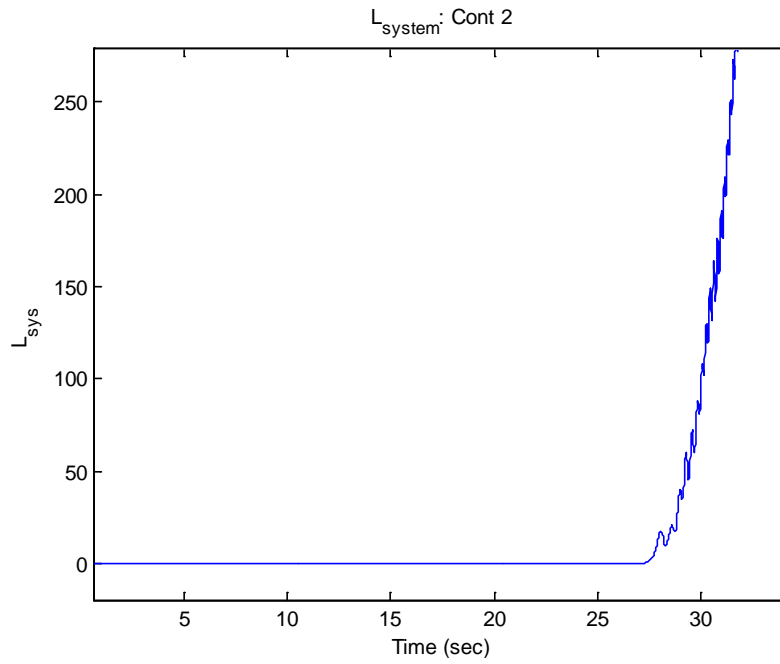


Figure 5- 4: Lagrangian Computation for Unstable Cont1

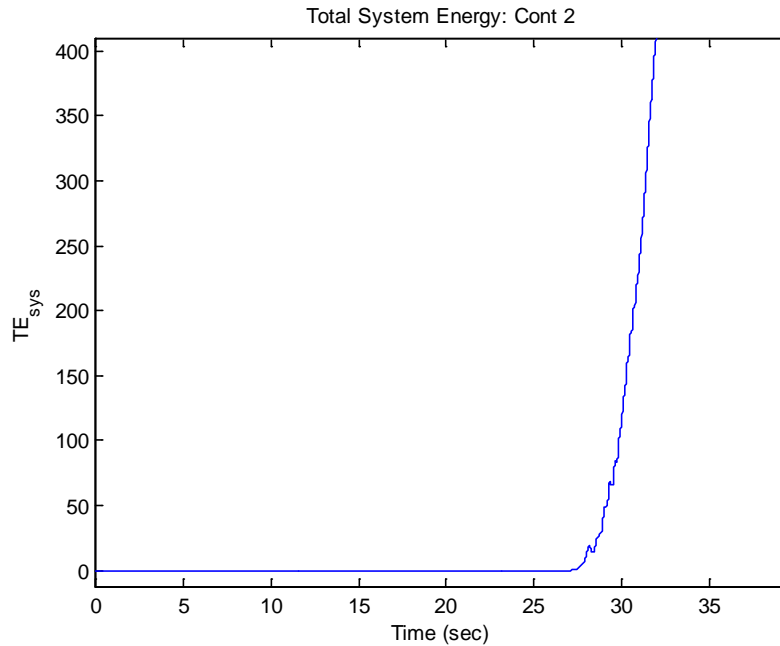


Figure 5- 5 Energy for Unstable Cont1

In this case, we see that all four algorithms detected the correct critical set of generators however, since Generators 2 and 3 are electrically close to each other it becomes difficult to tell which one is the most critical.

Table 5- 4: Unstable Cont 1 Algorithm Comparisons

Unstable Cont 1		
	Gen	Time (sec)
Effort	3	27.49
Energy	2	27.73
Lagrange	2	27.65
Angle	2	27.74

In the previous case, we see that the Effort, energy, and Lagrangian indicated instability quickly and at almost the same time. The Lagrangian is actually the quickest to indicate the critical generator whereas in the fault case we saw that Effort and the angle algorithm were the quickest. One important aspect of using energy is that both angle and frequency is used making it more flexible in determining stability among many different scenarios. Table 5-5 shows the comparisons of 4 stable and unstable Contingencies.

Table 5- 5: High Loading Level Comparisons

Unstable Cont 1			Stable Cont 1		
	Gen	Time (sec)		Gen	Time (sec)
Effort	9	7.7	Effort	-	INF
Energy	5	23.02	Energy	-	INF
Lagrange	9	9.27	Lagrange	-	INF
Angle	8	5.69	Angle	-	INF
Unstable Cont 2			Stable Cont 2		
	Gen	Time (sec)		Gen	Time (sec)
Effort	3	27.49	Effort	-	INF
Energy	2	27.73	Energy	-	INF
Lagrange	2	27.65	Lagrange	-	INF
Angle	2	27.74	Angle	-	INF
Unstable Cont 3			Stable Cont 3		
	Gen	Time (sec)		Gen	Time (sec)
Effort	9	20.63	Effort	-	INF
Energy	2	25.36	Energy	-	INF
Lagrange	3	25.52	Lagrange	-	INF
Angle	8	6.04	Angle	-	INF
Unstable Cont 4			Stable Cont 4		
	Gen	Time (sec)		Gen	Time (sec)
Effort	9	24.870001	Effort	-	INF
Energy	5	50.23	Energy	-	INF
Lagrange	9	30.93	Lagrange	-	INF
Angle	8	21.11	Angle	-	INF

The stable cases show that none of the algorithms initiated a false trip. Since neither the total energy of the system or total Lagrangian of the system exceeded 0.2 pu an event was not detected thus Effort was not computed for any of the four stable contingencies. Other algorithms are used in power systems to detect when an event is occurring, such as frequency decline, however since we are calculating energy it is easy to check and see if it is changing significantly which would indicate an event. The Lagrangian shown in Figure 5-6 clearly shows that each generator settles down to its stable equilibrium.

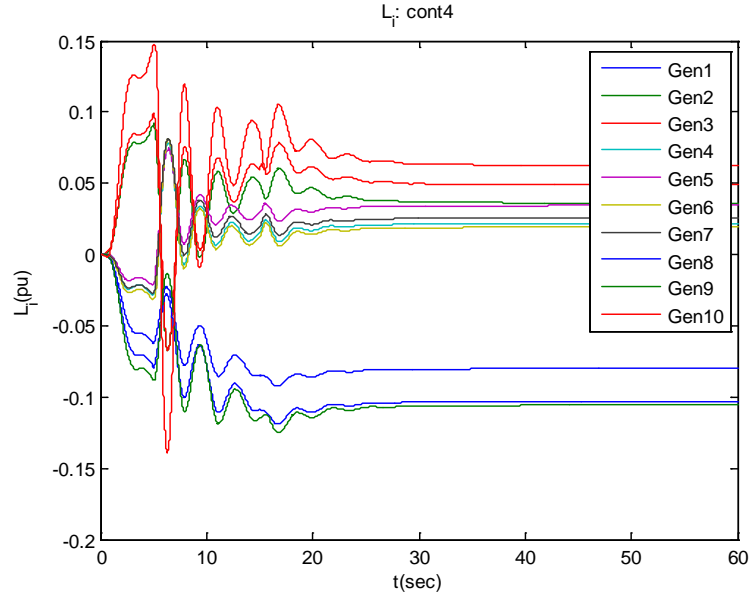


Figure 5- 6: Lagrangian for Stable Cont 4

5.2 39 Bus 3 Area System Fault Case

The simulations for the 39 bus test system separated into 3 areas connected through long transmission tie-lines as shown in Figure A-1 in the appendix. As with the previous test system, we look at cases where faults cause instability and also for heavy loading scenarios. Tables 5-6, 5-7, and 5-8 show the thresholds for various loading levels of the system. These correspond with maximum loading with decrements of 20% of the maximum.

Table 5- 6: Max Loading Thresholds

	Thresholds, Max Loading				
	Effort	Lagrange	Energy	Angle(deg)	Output(MW)
gen1	0.15	1.5971	1.6644	+/-90°	496.19
gen2	0.5	2.1816	2.8869	+/-90°	608.92
gen3	0.23	2.4005	2.6179	+/-90°	698.81
gen4	0.37	2.1046	2.4125	+/-90°	666.65
gen5	0.35	1.125	1.1854	+/-90°	535.85
gen6	0.34	2.1156	2.4022	+/-90°	685.69
gen7	0.46	1.7097	1.9052	+/-90°	590.70
gen8	0.15	2.0554	2.1241	+/-90°	674.58
gen9	0.07	1.4012	1.5821	+/-90°	770.45
gen10	1.02	9.3675	11.4086	+/-90°	1054.41

Table 5- 7: Thesholds For 20% Less Load

	Thresholds, Minus 20% Load/Generation				
	Effort	Lagrange	Energy	Angle(deg)	Output(MW)
gen1	0.28	1.0468	1.045	+/-90°	396.93
gen2	0.48	1.9945	2.4465	+/-90°	440.91
gen3	0.29	2.0464	2.237	+/-90°	559.06
gen4	0.41	1.3643	2.2027	+/-90°	533.26
gen5	0.34	0.7266	0.7782	+/-90°	428.65
gen6	0.44	1.3996	1.6653	+/-90°	548.49
gen7	0.47	1.0812	1.3529	+/-90°	472.51
gen8	0.4	1.9316	1.9916	+/-90°	539.65
gen9	0.28	2.5159	2.745	+/-90°	616.33
gen10	1.56	10.9976	14.1353	+/-90°	843.57

Table 5- 8: Thresholds For 40% Less Load

	Thresholds, Minus 40% Load/Generation				
	Effort	Lagrange	Energy	Angle(deg)	Output(MW)
gen1	0.27	0.5547	0.9211	+/-90°	297.65
gen2	0.35	1.9453	2.386	+/-90°	309.75
gen3	0.35	1.6131	2.3881	+/-90°	419.22
gen4	0.47	1.214	2.3556	+/-90°	399.88
gen5	0.25	0.4158	0.4527	+/-90°	321.43
gen6	0.52	1.3773	2.201	+/-90°	411.27
gen7	0.34	1.5521	2.1847	+/-90°	354.33
gen8	0.42	1.0989	1.621	+/-90°	404.68
gen9	0.53	2.2245	2.4637	+/-90°	462.17
gen10	1.34	8.3141	13.9735	+/-90°	632.61

Generation has been scaled by the same amount as the load. It should be noted that the angle algorithm thresholds were increased to 90° for simulations on the 3 area 39 bus system to reduce its sensitivity to false instability indication.

The tests on the 39 bus 3-area power system include testing three different thresholds, calculated at the 3 loading levels, to determine the algorithms effectiveness in correctly indicating instability with regards to moderate and large load changes. The thresholds used are indicated in the first column of Tables 5-9, 5-10, and 5-11. The actual loading level is indicated in the header of each table. The angle algorithm thresholds are held at 90° for all loading cases.

Table 5- 9: Unstable Cases Using Maximum Loading

Unstable Cases: Max Loading								
Bus 4 4-14								
Threshold	Energy Function		Angle Alg		Lagrange		Effort	
Max	2	1.887	3	0.657	2	2.047	3	0.34
	3	1.267	10	0.119	3	1.057		
-20%	2	1.887			2	2.037	3	0.37
	3	1.257			3	0.637		
-40%	3	1.267			2	2.037	2	0.6
	5	1.087			3	0.304	3	0.4
Bus 5 5-6								
Threshold	Energy Function		Angle Alg		Lagrange		Effort	
Max	2	0.897	3	0.579	2	0.393	2	0.44
	3	0.867	10	0.109	3	0.314	3	0.29
-20%	2	0.877			2	0.314	2	0.43
	3	0.837			3	0.265	3	0.32
-40%	2	0.877			2	0.304	2	0.36
	3	0.847			3	0.216	3	0.34
	5	0.747						
Bus 12 12-11								
Threshold	Energy Function		Angle Alg		Lagrange		Effort	
Max	2	2.197	3	0.969	2	2.307	3	0.43
	3	2.187	10	0.129	3	1.977		
-20%	2	2.187			2	2.307	3	0.48
	3	2.177			3	1.957		
-40%	3	2.177			2	2.307	2	1.13
	5	1.107			3	1.917	3	0.54
Bus 21 21-22								
Threshold	Energy Function		Angle Alg		Lagrange		Effort	
Max	2	1.737	2	0.195	6	0.388	6	0.37
	3	1.577	10	0.108	7	3.448		
-20%	2	1.727			6	0.224	6	0.42
	3	1.547			7	0.233		
-40%	2	1.717			5	0.388	7	0.44
	3	1.557			6	0.224		

Table 5- 10: Unstable Cases Using Maximum Loading(continued)

Bus 23 23-24								
Threshold	Energy Function		Angle Alg		Lagrange		Effort	
Max	2	1.747	2	0.195	6	3.518	6	0.4
	3	1.587	10	0.108	7	0.195	7	0.37
-20%	2	1.737			6	0.253	6	0.45
	3	1.557			7	0.127	7	0.38
-40%	2	1.737			6	0.253	7	0.32
	3	1.567			7	0.175		
Bus 24 24-16								
Threshold	Energy Function		Angle Alg		Lagrange		Effort	
Max	2	1.62	2	0.21	2	1.53	6	0.41
	3	1.48	10	0.11	3	1.44	7	0.5
-20%	2	1.61			6	0.29	6	0.47
	3	1.45			7	0.22	7	0.51
-40%	2	1.61			5	0.45	6	0.51
	3	1.46			6	0.29	7	0.42
Bus 26 26-28								
Threshold	Energy Function		Angle Alg		Lagrange		Effort	
Max	3	1.547	1	0.166	1	0.233	8	0.28
	9	0.262	8	0.146	9	0.195	9	0.2
-20%	3	1.427			1	0.166	1	0.34
	9	0.339			9	0.262	9	0.31
-40%	1	0.233			1	0.118	1	0.33
	9	0.32			8	0.195	9	0.39
Bus 26 26-29								
Threshold	Energy Function		Angle Alg		Lagrange		Effort	
Max	9	0.262	8	0.146	1	0.233	1	0.26
			10	0.118	9	0.195	9	0.2
-20%	9	0.339			1	0.166	1	0.34
					9	0.262	9	0.31
-40%	1	0.233			1	0.118	1	0.33
	9	0.32			8	0.195	9	0.39
Bus 29 29-28								
Threshold	Energy Function		Angle Alg		Lagrange		Effort	
Max	9	0.243	8	0.166	9	0.156	1	0.33
			10	0.127			9	0.18
-20%	9	0.301			1	0.497	9	0.27
					9	0.224		
-40%	9	0.282			1	0.156	1	0.45
					9	0.204	9	0.34

Table 5- 11: Unstable Cases Using 20% Less Load Of Maximum

Unstable Cases: -20% Load/Generation								
Bus 4 4-14								
Threshold	Energy Function		Angle Alg		Lagrange		Effort	
Max	2	2.25	2	2.18	3	1.53	3	0.42
	3	1.43	3	0.75				
-20%	2	2.23			3	1.52	3	0.47
	3	1.42						
-40%	2	2.23			3	1.51	3	0.52
	3	1.43						
Bus 5 5-6								
Threshold	Energy Function		Angle Alg		Lagrange		Effort	
Max	2	1.25	3	0.63	2	1.07	2	0.67
	3	1.19	10	0.39	3	1.02	3	0.35
-20%	2	1.24			2	1.06	2	0.64
	3	1.17			3	1	3	0.39
-40%	2	1.24			2	1.06	2	0.52
	3	1.18			3	0.39	3	0.42
Bus 12 12-11								
Threshold	Energy Function		Angle Alg		Lagrange		Effort	
Max	2	3.317	2	2.127	2	3.517	2	2.03
	3	2.567	3	1.411	3	2.307	3	0.61
-20%	2	3.297			2	3.507	2	1.97
	3	2.547			3	2.267	3	0.75
-40%	2	3.297			2	3.507	2	1.68
	3	2.557			3	2.107	3	0.89
Bus 21 21-22								
Threshold	Energy Function		Angle Alg		Lagrange		Effort	
Max	3	1.537	2	0.373	-	-	6	0.46
			6	0.422	-	-	7	0.69
			10	0.304				
-20%	3	1.467			-	-	6	0.53
					-	-	7	0.7
-40%	3	1.497			1	1.237	6	0.59
					5	1.367	7	0.56
Bus 23 23-24								
Threshold	Energy Function		Angle Alg		Lagrange		Effort	
Max	3	1.577	7	0.314	-	-	6	0.5
			10	0.314	-	-	7	0.46
-20%	3	1.507			7	0.167	6	0.58
							7	0.46
-40%	3	1.537			5	1.437	6	0.65
					7	0.295	7	0.38

Table 5- 12: Unstable Cases Using 20% Less Load Of Maximum (continued)

Bus 24 24-16								
Threshold	Energy Function		Angle Alg		Lagrange		Effort	
Max	3	1.757	2	0.393	-	-	6	0.55
			7	0.432	-	-	7	0.7
			10	0.324				
-20%	3	1.677			-	-	6	0.65
					-	-		
-40%	3	1.707			1	1.627	7	0.56
					5	1.497		
Bus 26 26-28								
Threshold	Energy Function		Angle Alg		Lagrange		Effort	
Max	1	0.827	1	0.285	1	0.737	1	0.3
	9	0.324	8	0.246	9	0.246	9	0.23
			9	0.353				
-20%	1	0.777			1	0.226	1	0.42
	9	0.539			9	0.363	9	0.36
-40%	1	0.767			1	0.138	1	0.41
	9	0.451			9	0.334	9	0.46
Bus 26 26-29								
Threshold	Energy Function		Angle Alg		Lagrange		Effort	
Max	1	0.847	1	0.285	1	0.747	1	0.3
	9	0.324	8	0.246	9	0.246	9	0.23
			9	0.353				
-20%	1	0.787			1	0.226	1	0.42
	9	0.539			9	0.363	9	0.36
-40%	1	0.767			1	0.138	1	0.41
	9	0.451			9	0.334	9	0.46
Bus 29 29-28								
Threshold	Energy Function		Angle Alg		Lagrange		Effort	
Max	1	0.887	1	0.383	1	0.807	1	0.46
	9	0.285	8	0.334	9	0.207	9	0.2
			9	0.314				
-20%	1	0.837			1	0.727	9	0.32
	9	0.402			9	0.295		
-40%	1	0.827			1	0.667	1	0.69
	9	0.373			9	0.275	9	0.4

Table 5- 13: Unstable Cases With 40% Less Load From Maximum

Unstable Cases: -40% Load/Generation								
Bus 4 4-14								
Threshold	Energy Function		Angle Alg		Lagrange		Effort	
Max	-	-	2	1.637	-	-	2	1.74
	-	-	3	1.178	-	-	3	0.55
-20%	-	-			-	-	2	1.7
	-	-			-	-	3	0.65
-40%	1	2.854			3	3.513	2	1.45
	5	2.126					3	0.78
Bus 5 5-6								
Threshold	Energy Function		Angle Alg		Lagrange		Effort	
Max	2	1.407	3	0.781	2	1.257	2	0.85
	3	1.387	10	0.169	3	1.257	3	0.4
-20%	2	1.397			2	1.247	2	0.81
	3	1.377			3	1.237	3	0.46
-40%	2	1.387			2	1.227	2	0.63
	3	1.357			3	1.177	3	0.51
Bus 12 12-11								
Threshold	Energy Function		Angle Alg		Lagrange		Effort	
Max	3	5.16	3	3.44	2	5.34	3	0.94
			10	5.6	3	4.96	10	2.22
-20%	3	5.15			2	5.32	2	2.21
					3	4.9	3	1.13
-40%	3	5.14			2	5.28	2	1.74
					3	4.67	3	1.3
Bus 21 21-22								
Threshold	Energy Function		Angle Alg		Lagrange		Effort	
Max	9	1.37	2	0.36	9	1.34	6	0.6
	1	1.45	10	0.22			7	0.92
			6	0.48				
-20%	1	1.28			1	1.31	6	0.72
	3	1.45					7	0.93
-40%	1	1.2			5	1.04	6	0.82
	2	1.48			1	1.19	7	0.75
Bus 23 23-24								
Threshold	Energy Function		Angle Alg		Lagrange		Effort	
Max	1	1.63	2	0.4	-	-	6	0.71
	3	1.67	7	0.34	-	-	7	0.57
			10	0.24				
-20%	1	1.45			1	1.49	6	0.85
	3	1.61			7	0.28	7	0.58
-40%	1	1.36			4	1.16	6	0.96
	3	1.57			5	1.11	7	0.46

Table 5- 14: Unstable Cases With 40% Less Load From Maximum (continued)

Bus 24 24-16								
Threshold	Energy Function		Angle Alg		Lagrange		Effort	
Max	3	1.69	2	0.42	-	-	6	0.83
			7	0.51	-	-	7	0.98
			10	0.28				
-20%	1	1.62			-	-	6	0.99
	3	1.64			-	-	7	0.99
-40%	1	1.43			1	1.35	7	0.79
	3	1.59			5	1.54		
Bus 26 26-28								
Threshold	Energy Function		Angle Alg		Lagrange		Effort	
Max	1	1.07	8	0.19	1	1.03	1	0.36
	9	0.55	9	0.33	9	0.36	9	0.27
-20%	1	1.06			1	1.02	1	0.56
	8	1.24			8	1.09	9	0.43
-40%	1	1.05			1	0.17	1	0.53
	5	0.66			9	0.44	9	0.56
	9	1.49						
Bus 26 26-29								
Threshold	Energy Function		Angle Alg		Lagrange		Effort	
Max	1	1.07	8	0.19	1	1.03	1	0.36
	9	0.55	9	0.33	9	0.36	9	0.27
-20%	1	1.06			1	1.02	1	0.56
	8	1.25			8	1.1	9	0.43
-40%	1	1.05			1	0.17	1	0.53
	5	0.66			9	0.44	9	0.56
	8	1.2						
Bus 29 29-28								
Threshold	Energy Function		Angle Alg		Lagrange		Effort	
Max	1	1.81	8	0.27	1	1.75	1	0.45
	9	1.52	9	0.28	9	0.13	9	0.14
-20%	1	1.8			1	1.06	1	0.74
	9	1.55			9	0.3	9	0.26
-40%	1	1.79			1	0.25	1	0.7
	9	1.53			9	0.2	9	0.36

The following tables show some interesting correlations between thresholds and loading levels. For the maximum loading case shown in Table 5-9 the thresholds computed on each of the load levels produced similar results. However, using thresholds computed at a lower loading level on a system with increased load causes the algorithms to be less sensitive. Conversely, if we use thresholds computed on a system that has a greater loading amount than what is actually being used in the system then the algorithm generally tends to be more sensitive in detecting instability. For load fluctuations that are

small, say +/-5% of total load demand, we wouldn't need to update the thresholds. Load fluctuations in excess of +/-20% would mean that a new set of thresholds would need to be used in order to correctly identify critical generators. This should be a concern only in systems operating near maximum loading since faults are usually cleared in much less time than the c.c.t. for lightly loaded systems. We now compare the improvements in c.c.t. shown in Tables 5-12, 5-13, and 5-14.

Table 5- 15: CCT at Max Loading Using Different Threshold Sets

Simulations At Max Loading					
Simulations Using Thresholds From Max Loading					
Contingency	CCT	Energy	Angle	Lagrange	Effort
bus 4 4-14	33.29	33.43	33.72	33.44	34.6
bus 5 5-6	23.91	24.61	24.9	25.19	25.19
bus12 12-11	63.05	63.06	87.93	63.06	66.82
bus26 26-29	9.80	18.98	16.38	20.14	20.14
bus29 29-28	9.95	19.56	15.34	20.28	20.14
bus26 26-28	10.82	19.13	16.96	20.28	20.28
bus21 21-22	17.80	18.11	30.68	19.7	20
bus23 23-24	17.80	18.26	29.96	21	20
bus24 24-16	22.17	22.59	34.15	22.59	26
Simulations Using Thresholds From -20% Loading					
Contingency	CCT	Energy	Angle	Lagrange	Effort
bus 4 4-14	33.29	33.81	33.72	33.5	33.94
bus 5 5-6	23.91	24.24	24.9	24	24.89
bus12 12-11	63.05	63.1	87.93	64.22	65.94
bus26 26-29	9.80	17.8	16.38	19.54	19.86
bus29 29-28	9.95	18.9	15.34	19.81	19.37
bus26 26-28	10.82	18.5	16.96	19.81	19.34
bus21 21-22	17.80	17.2	30.68	19.2	18.11
bus23 23-24	17.80	18.03	29.96	20.34	19.93
bus24 24-16	22.17	22.25	34.15	21.27	25.52
Simulations Using Thresholds From -40% Loading					
Contingency	CCT	Energy	Angle	Lagrange	Effort
bus 4 4-14	33.29	33.06	33.72	34.95	34.01
bus 5 5-6	23.91	24.14	24.9	24.39	25.24
bus12 12-11	63.05	64.2	87.93	66.9	66.87
bus26 26-29	9.80	17.2	16.38	18.31	19.73
bus29 29-28	9.95	16.76	15.34	18.02	19.24
bus26 26-28	10.82	18.53	16.96	17.36	18.96
bus21 21-22	17.80	18.9	30.68	17.22	17.94
bus23 23-24	17.80	18.47	29.96	18.92	19.17
bus24 24-16	22.17	23.66	34.15	23	24.78

Table 5- 16: CCT at -20% Loading Using Different Threshold Sets

Simulations At -20% Loading					
Simulations Using Thresholds From Max Loading					
Contingency	CCT	Energy	Angle	Lagrange	Effort
bus 4 4-14	51.94	52	52.08	52.11	53.11
bus 5 5-6	34.54	35.94	34.04	34.53	34.97
bus12 12-11	104.67	104.11	104.7	104.45	106.1
bus26 26-29	17.95	23.23	21.87	18.11	23.54
bus29 29-28	18.24	23.19	24.04	22.74	23.74
bus26 26-28	18.67	23.99	24.47	24	25.62
bus21 21-22	24.94	25.14	28.38	-	28.67
bus23 23-24	25.52	25.34	33	-	32.11
bus24 24-16	29.59	30.27	32.86	-	32.64
Simulations Using Thresholds From -20% Loading					
Contingency	CCT	Energy	Angle	Lagrange	Effort
bus 4 4-14	51.94	51.93	52.08	51.93	52.65
bus 5 5-6	34.54	34.59	34.04	34.59	34.88
bus12 12-11	104.67	104.54	104.7	104.54	104.98
bus26 26-29	17.95	24.47	21.87	18.11	23.17
bus29 29-28	18.24	22.74	24.04	22.74	22.74
bus26 26-28	18.67	24.62	24.47	19.27	24.62
bus21 21-22	24.94	24.76	28.38	-	28.09
bus23 23-24	25.52	25.48	33	32.28	29.82
bus24 24-16	29.59	29.53	32.86	-	31.56
Simulations Using Thresholds From -40% Loading					
Contingency	CCT	Energy	Angle	Lagrange	Effort
bus 4 4-14	51.94	51.5	52.08	51.89	52.45
bus 5 5-6	34.54	35.13	34.04	34.25	34.29
bus12 12-11	104.67	104.3	104.7	104.61	104.72
bus26 26-29	17.95	23.92	21.87	18.96	23.33
bus29 29-28	18.24	22.47	24.04	21.49	23.12
bus26 26-28	18.67	24.31	24.47	19.31	24.51
bus21 21-22	24.94	25.1	28.38	26.1	28.23
bus23 23-24	25.52	25.82	33	32.06	32.43
bus24 24-16	29.59	30.75	32.86	31.68	31.97

Table 5- 17: CCT at -40% Loading Using Different Threshold Sets

Simulations At -40% Loading					
Simulations Using Thresholds From Max Loading					
Contingency	CCT	Energy	Angle	Lagrange	Effort
bus 4 4-14	167.80	-	132.88	-	135
bus 5 5-6	49.30	51.05	52.56	50.03	5.22
bus12 12-11	264.90	217.99	218.9	217.69	221.03
bus26 26-29	24.40	30.62	34.8	33.41	32.77
bus29 29-28	26.40	34.19	33.5	35.22	35.82
bus26 26-28	25.00	33.89	35.1	31.76	34.27
bus21 21-22	35.69	49.43	49.5	48.36	49.07
bus23 23-24	39.96	51.97	53.44	-	55.82
bus24 24-16	44.05	58.2	58.97	-	59.34
Simulations Using Thresholds From -20% Loading					
Contingency	CCT	Energy	Angle	Lagrange	Effort
bus 4 4-14	167.80	132.59	132.88	133.01	133.21
bus 5 5-6	49.30	52.36	52.56	50.87	52.67
bus12 12-11	264.90	218.76	218.9	218.32	218.5
bus26 26-29	24.40	30.94	34.8	33.09	32.23
bus29 29-28	26.40	32.37	33.57	35.97	36.9
bus26 26-28	25.00	33.32	35.15	34.11	34.1
bus21 21-22	35.69	46.9	49.5	46.38	49.16
bus23 23-24	39.96	53.54	53.44	52.74	55.89
bus24 24-16	44.05	54.73	58.97	57.35	57.51
Simulations Using Thresholds From -40% Loading					
Contingency	CCT	Energy	Angle	Lagrange	Effort
bus 4 4-14	167.80	132.9	132.88	132.88	134
bus 5 5-6	49.30	51.98	52.56	51.98	52.3
bus12 12-11	264.90	218.9	218.9	218.88	218.9
bus26 26-29	24.40	31.7	34.8	32.77	32.77
bus29 29-28	26.40	32.63	33.5	35.68	36
bus26 26-28	25.00	32.48	35.1	33.35	33.36
bus21 21-22	35.69	48.49	49.5	48.64	49.36
bus23 23-24	39.96	52.41	53.44	52.7	55.47
bus24 24-16	44.05	58.09	58.97	58.1	58.82

In the each of the previous tables, the loading in the system is held constant while the threshold sets are varied. The results indicate that each algorithm performs differently between areas as the loading changes. This could be from the stress on the system at high loading being reduced as the loading is reduced. As an example let us examine Table 5-12. The last three cases with faults in Area 1 show that the angle algorithm has the greatest improvement in critical clearing time, whereas in Area 3, the Effort shows a greater improvement over the angle algorithm. The effects load changes have on the thresholds are not clearly understood and further research is needed.

5.2.1 39 Bus 3 Area System Heavy Loading Case

For the heavy loading cases simulated on the 39 bus 3 area system we look at the maximum loaded system as the base load demand. Four stable and unstable cases are shown in Table 5-15. The thresholds computed using offline transient simulations are given in Table 5-6, using the heaviest loading scenario.

Table 5- 18: Excessive Loading, 3-Area System

Unstable Cont 1			Stable Cont 1		
	Gen	Time (sec)		Gen	Time (sec)
Effort	3	29.28	Effort	NAN	INF
Energy	3	29.56	Energy	NAN	INF
Lagrange	3	29.28	Lagrange	NAN	INF
Angle	3	29.68	Angle	NAN	INF
Unstable Cont 2			Stable Cont 2		
	Gen	Time (sec)		Gen	Time (sec)
Effort	3	26.52	Effort	NAN	INF
Energy	3	26.84	Energy	NAN	INF
Lagrange	3	26.6	Lagrange	NAN	INF
Angle	3	26.88	Angle	NAN	INF
Unstable Cont 3			Stable Cont 3		
	Gen	Time (sec)		Gen	Time (sec)
Effort	3	41	Effort	NAN	INF
Energy	3	41.36	Energy	NAN	INF
Lagrange	3	41	Lagrange	NAN	INF
Angle	3	41.36	Angle	NAN	INF
Unstable Cont 4			Stable Cont 4		
	Gen	Time (sec)		Gen	Time (sec)
Effort	3	10.56	Effort	NAN	INF
Energy	3	10.8	Energy	NAN	INF
Lagrange	3	10.52	Lagrange	NAN	INF
Angle	3	10.92	Angle	NAN	INF

The stable cases all indicate that the system remains stable as predicted from all four algorithms. Looking at the unstable cases we see that the four algorithms detect the critical generators with control times almost identical to each other. It also appears that in the three area system the angle algorithm detects instability better. This could be due to the fact that with higher loading the system in the 3 area case the system is beyond marginally unstable where as in the unmodified system the loading leads to marginal instability with only one generator losing synchronism. The excessive loaded cases do cause the system to break apart as seen from the rotor angle measurements shown in Figure 5-7 below.

In fact, we see that area 2 loses synchronism from the rest of the system with Generators 2 and 3 accelerating and Generator 10 decelerating. Examining the

Lagrangian and Effort we see that both Generator 2 and 3 would be candidates for tripping since they remain in synchronism with each other. The Lagrangian, Energy, and Effort are shown in Figures 5-8, 5-9, and 5-10 respectively.

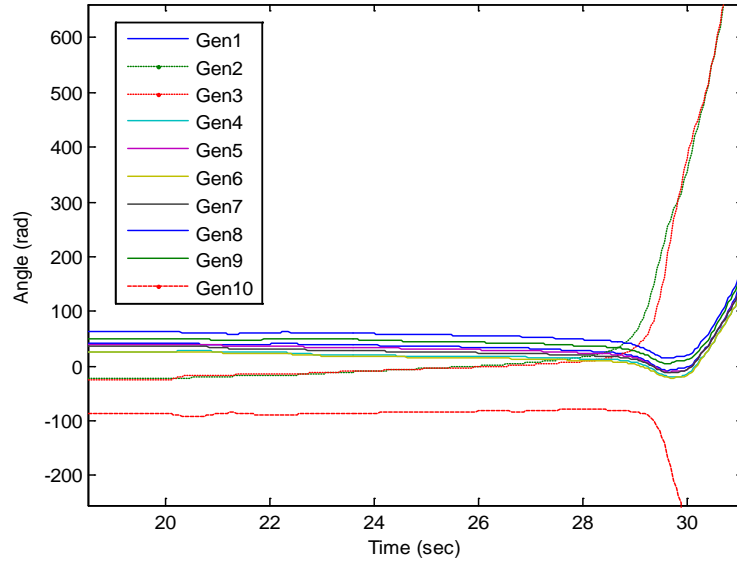


Figure 5- 7: Rotor Angle For 3-Area Over Load Case

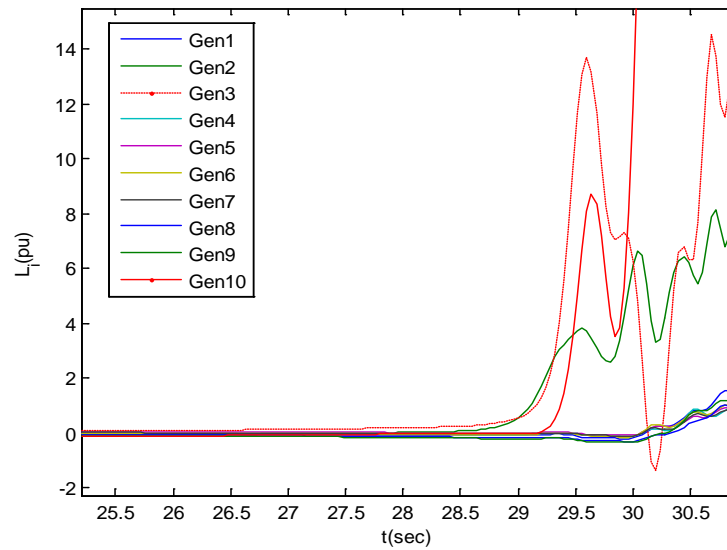


Figure 5- 8: Lagrangian Computation for Unstable Cont4

For the Lagrangian, we see little difference between Generator 2 and 3 between 28 and 29.25 seconds. Generator 3 losses synchronism the fastest as you can see from the dotted line in Figure 5-8.

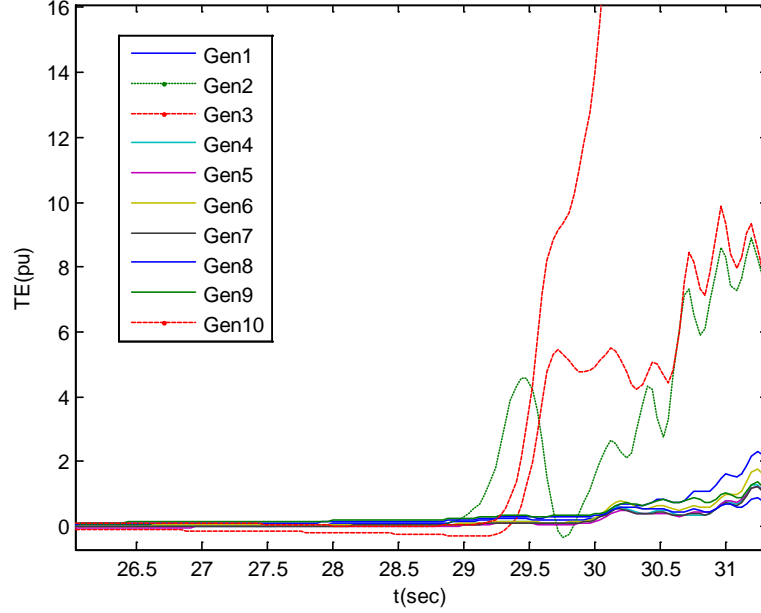


Figure 5- 9: Energy Computation for Unstable Cont4

The total energy in Figure 5-9 shows that Generator 2 is the critical generator, rather than Generator 3. This error is due to the kinetic energy not being corrected as explained in [5], where the energy not contributing to the instability should be subtracted out. Without correcting the kinetic energy, we end up with a phase shifted signal as can be observed in Figure 5-9. Correcting for the non contributing kinetic energy is not easily accomplished in real-time since it requires the trajectories to be computed.

The Effort computed in Figure 5-10 indicates that both Generator 2 and 3 are critical generators thus generation shedding should be initiated at both of them. This agrees with the results from the angle and Lagrangian algorithms.

To make the previous cases stable, it is necessary to shed a significant amount of load. From results on the 39 bus 3-area system it was required to shed at least half the load in that area to regain stability, with regards to the excessive loading cases. The problem with shedding this much load is that voltage levels tend to spike excessively. In real life applications this can be a serious issue since over voltage protection equipment may cause unnecessary tripping of transformers and lines.

As an example, let us look at the unstable case 2 in Table 5-15. For the control action we shed the same percentage of real power demand as with the reactive power. The control time for the Effort in this case is 26.52 seconds. To make the system stable we need to shed loading at specific load buses as discussed in the thesis [20].

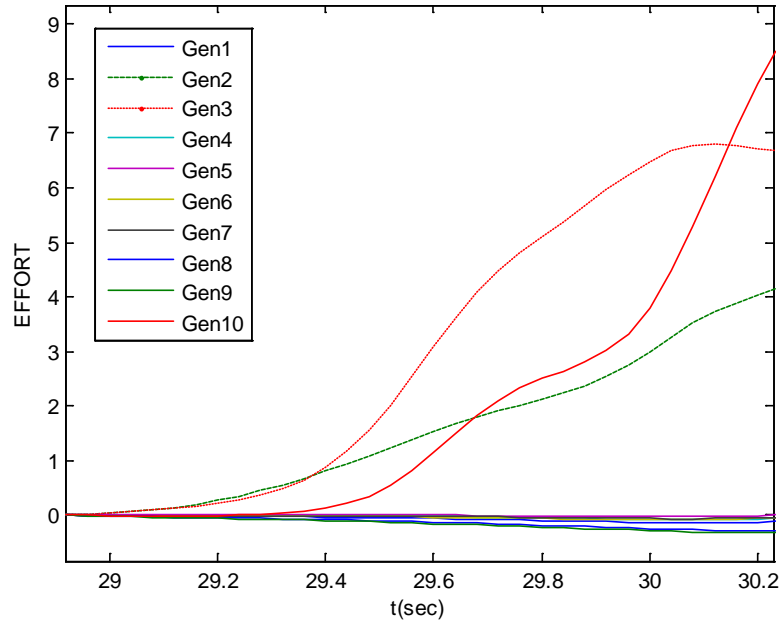


Figure 5- 10: Effort Computation Unstable Cont4

In this case, it was necessary to disconnect Generators 2 and 3 from the system thus causing a huge deficit in MVAR output in Area 2. To compensate for this it was required that over 2000 MW of load needed to be shed. Looking at the rotor angle in Figure 5-11 we see that Generator 10 stays in synch with the system. The frequency observed in Figure 5-12 indicates that Generator 10 has some damping issues with some large oscillations. The oscillations do damp out however the frequency goes beyond 60.5 Hz. With frequency relays set to operate at 0.2 Hz deviations we see that Generator 10 would have been disconnected from the system leading to a complete isolation of Area 2.

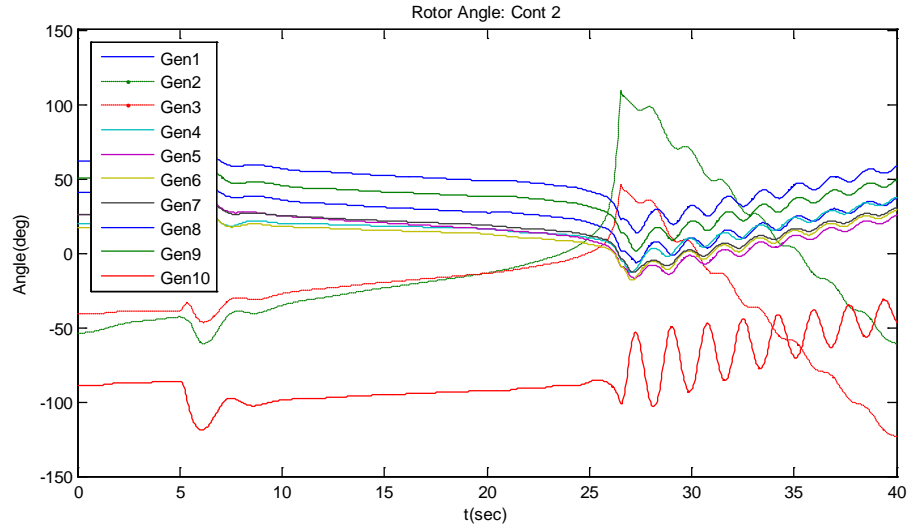


Figure 5- 11: Unstable Cont. 2 Rotor Angle

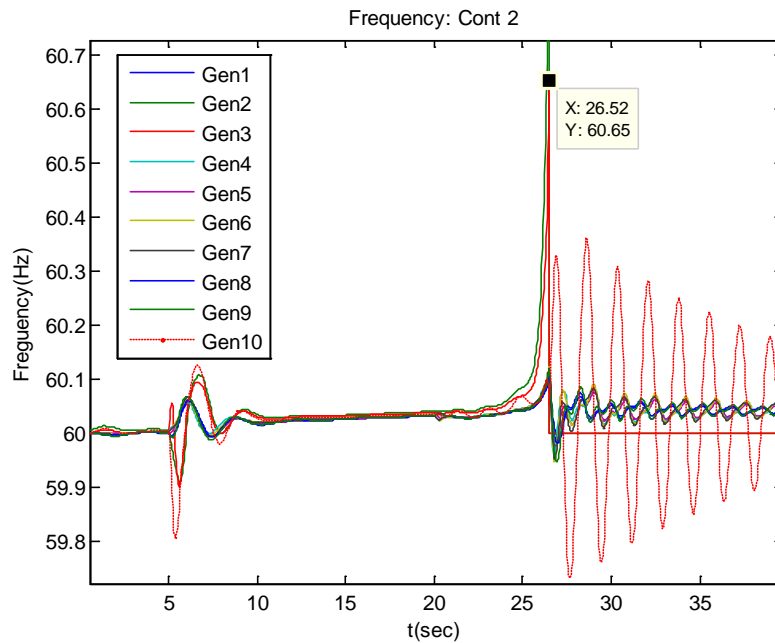


Figure 5- 12: Unstable Cont. 2 Rotor Frequency

Since we would expect frequency relays to operate sooner than what the control times indicate we could find the energy of each machine at 60.2 Hz and use it as a threshold instead of looking at the maximum stability limit. This of course would make

the algorithm more sensitive but we would gain more time in implementing the control action thus reducing the amount of load shed needed to keep the system synchronized. The other issue is over/under voltage relays. Figure 5-13 shows the voltage magnitude during the transients. At the control time near 26 seconds we see that the voltage spikes to almost 1.2 pu. In some instances this may be enough to trigger voltage relay devices.

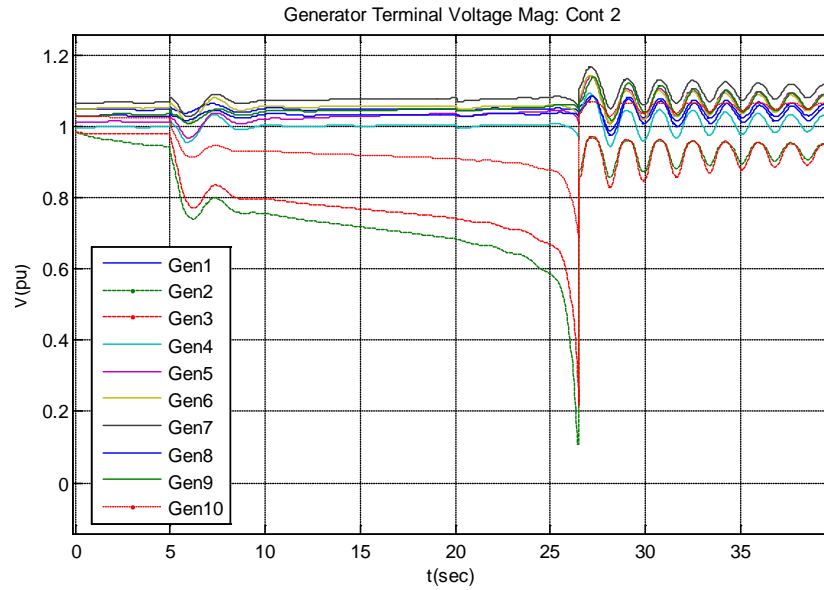


Figure 5- 13: Voltage Magnitude, Unstable Cont 2

IEEE standards indicate that voltage protection should have a delay of 1s when the spikes are between 1.1 pu and 1.2 pu [15] so for this system we would see some of the relays operate. The following table indicating average voltage protection relay settings was taken from [15].

Table 5- 19: Recommended Voltage Protection Delay Times

Voltage range (% of base voltage ^a)	Clearing time (s) ^b
$V < 50$	0.16
$50 \leq V < 88$	2.00
$110 < V < 120$	1.00
$V \geq 120$	0.16

^aBase voltages are the nominal system voltages stated in ANSI C84.1-1995, Table 1.

^bDR \leq 30kW, maximum clearing times; DR > 30kW, default clearing times.

Table 5-17 [15] tells us that for a normal frequencies we would also expect Generator 10 to trip since its frequency stays above 60.5 Hz for a greater amount of time than 0.16 seconds. Since Generators 2 and 3 clearly exceed 60.5 Hz as seen in Figure 5-13 they would be disconnected before the control actions could be initiated. Future research is recommended.

Table 5- 20: Frequency Relay Delay Times

DR size	Frequency range (Hz)	Clearing time (s) ^a
$\leq 30\text{kW}$	>60.5	0.16
	< 59.3	0.16
$> 30\text{kW}$	> 60.5	0.16
	$< \{59.8 - 57.0\}$ (adjustable set point)	Adjustable 0.16 to 300
	< 57.0	0.16

^aDR $\leq 30\text{kW}$, maximum clearing times; DR $> 30\text{kW}$, default clearing times.

The previous tables were based on connections between transmission systems and distribution level machines. Such an example would be the WSU steam plant. Plants connected through transmission networks in general require tighter tolerances so the values in Tables 5-16 and 5-17 may be underestimated.

5.3 Communication Delay Effect

One of the issues of concern in power systems is the time it takes for a measurement to be sent from the PMU to the communication center. Computations are made to determine the control action which also takes time. The control action decided at the communications center is then sent to the corresponding plants where generation shedding/disconnection are required. Using high speed communications the total time delay between the time data is collected and control action initiated is less than 100 ms, or about 6 cycles. This estimate is made assuming perfect operation, as well as open communication channels at all times. PMU's constitute a new technology so it is difficult to guess how they will be used in the future. So taking into account these issues we simulate the results from the 39 bus 3 Area system using a time delay of 5, 10, and 15 cycles. To judge the effects that the time delay has on the security of the system, we compute the critical clearing time and determine how many cycles it decreases for the given contingency. The impact on algorithm performance is evaluated by comparing the critical clearing time for the base case with the case where delay is added. The critical clearing times for the added communication delays are shown in the Tables 5-18, 5-19, 5-20, and 5-21.

Table 5- 21: Time Delay, Effort Algorithm

Cont.	Communication Delay: Effort			
	Critical Clearing Time (Cyc)			
	No Delay	5 Cyc.	10 Cyc.	15 Cyc.
4 4-14	34.88	34.45	34.16	34.00
5 5-6	25.34	25.20	25.20	25.11
12 12-11	67.26	66.39	65.81	65.33
26 26-29	21.15	19.56	18.12	16.79
29 29-28	20.72	19.85	18.84	17.37
26 26-28	21.29	19.70	18.55	16.99
21 21-22	20.14	19.85	21.73	21.63
23 23-24	20.14	19.99	21.29	21.63
24 24-16	26.04	25.90	25.32	24.84

Table 5- 22: Time Delay, Lagrangian Algorithm

Cont.	Communication Delay: Lagrangian			
	Critical Clearing Time (Cyc)			
	No Delay	5 Cyc.	10 Cyc.	15 Cyc.
4 4-14	40.08	39.79	39.65	39.51
5 5-6	30.25	31.70	29.53	29.24
12 12-11	69.86	69.86	69.86	69.86
26 26-29	20.28	18.84	17.53	16.38
29 29-28	22.01	20.43	18.98	17.54
26 26-28	20.43	18.98	17.68	16.53
21 21-22	20.28	19.85	19.42	19.13
23 23-24	22.31	21.44	20.86	20.43
24 24-16	20.73	20.73	20.87	20.87

Table 5- 23: Time Delay, Angle Algorithm

Cont.	Communication Delay: Angle Alg.			
	Critical Clearing Time (Cyc)			
	No Delay	5 Cyc.	10 Cyc.	15 Cyc.
4 4-14	33.87	33.72	33.58	33.58
5 5-6	25.05	24.91	24.76	24.76
12 12-11	63.93	63.64	63.49	63.35
26 26-29	19.27	18.11	17.10	16.24
29 29-28	17.97	17.39	16.67	15.80
26 26-28	19.42	18.41	17.39	16.38
21 21-22	20.57	19.85	19.27	18.84
23 23-24	20.57	20.00	19.42	18.98
24 24-16	23.31	22.74	22.45	22.02

Table 5- 24: Time Delay, Energy Algorithm

	Communication Delay: Energy			
	Critical Clearing Time (Cyc)			
Cont.	No Delay	5 Cyc.	10 Cyc.	15 Cyc.
4 4-14	33.44	33.44	33.43	33.29
5 5-6	24.76	24.62	25.48	25.48
12 12-11	63.06	63.06	63.06	63.06
26 26-29	19.85	18.41	17.10	15.95
29 29-28	20.00	19.13	17.83	16.53
26 26-28	20.00	18.55	17.25	16.24
21 21-22	17.68	17.83	17.97	17.97
23 23-24	17.97	18.11	18.11	18.26
24 24-16	22.59	22.59	22.59	22.59

The largest decrease in critical clearing times occur at the first five cycles of time delay. At 10 and 15 cycles, the delay effect is less severe for most of the cases. Looking at the previous tables, we see that this change is on average only a few tenths of a cycle. The critical clearing time decreases by about 1 cycle on average for a time delay of 10 cycles. This would suggest that the maximum effectiveness of the algorithms can be achieved if the communications delay is less than 10 cycles. In some of the cases, we can even see an increase in critical clearing time as the time delay increases as is evident in Table 5-21. Since power systems are nonlinear, it is important to consider the state of the system when initiating control action.

6. CONCLUSIONS

This report studies the usefulness of several synchrophasor based angle instability monitoring and control algorithms proposed by the authors earlier. From the simulations on the New England 39 bus system, we show that the algorithms are generally beneficial in maintaining angle stability. With the exception of the individual machine total energy functions, the Angle, Lagrangian, and Effort algorithms were capable of determining the critical generators for both fault scenarios and excessive loading cases, most notably the new algorithm based on the effort concept [20]. Transient disturbances where low voltages lead to angle instability are of significant importance. Under such circumstances, it may not be possible to prevent blackouts entirely, but their severity can be reduced. The algorithms presented here show promise in reducing the severity of blackouts.

The use of Effort concept in determining the real-time status of a disturbed system is a new technique proposed in the thesis [20]. Its use as an indicator of system stability need not be the only use. With more research, it may be possible to implement it in to load shedding schemes. Other possible uses may include spin reserve estimation, dynamic security assessment, or generation re-scheduling. Out of the four algorithms presented here, the Effort [20] and Angle [19], [7] algorithms have been shown to be well-suited for mitigating angle stability.

The time it takes for data to be measured and be ready for use at control centers is one of the main limitations in real-time implementation of proposed algorithms. With new advances in communication structures such as the proposed NASPInet in the North American power system, it is possible to limit this total delay to say less than 100 milliseconds. Since power systems are highly nonlinear, no assumption can be made on whether the angle instability gets worse from delays up to 100 ms. Future research is indicated on determining the sensitivity of synchrophasor real-time applications such as the angle instability control methods of this report to transducer and communication delays. It is important to carry out prior studies on how large these values can be while preserving the usefulness of wide-area dynamic data for futuristic control applications such as angle stability mitigation. It is important to have a clear insight into critically tolerable values of communication delays with respect to advanced control designs before we embark on the design and implementation of communication structures such as NSAPInet that is planned in the near future.

7. REFERENCES

- [1] "Power System Transient Stability Using Individual Machine Energy Functions," Anthony N. Michel, A.A. Fouad, Vijay Vittal, IEEE Transactions May 1983
- [2] "Theory of Nonlinear Control Systems", Nicolai Minorsky, Mcgraw Hill
- [3] "Blackout of 2003: Description and Responses", Dennis Ray PSERC, Nov. 5th 2003
- [4] "Final Report on the August 14th Blackout in the United States and Canada," U.S.-Canada Power System Outage Task Force
- [5] "Power System Transient Stability Analysis Using the Transient Energy Function Method," A.A. Fouad, Vijay Vittal, Prentice Hall, 1992.
- [6] "Mechanics and Electrodynamics," L.D. Landau, E.M. Lifshitz, Addison-Wesley Publishing 1972
- [7] "A Wide-Area Control For Mitigating Angle Instability In Electric Power Systems," Dongchen Hu, MS dissertation, Washington State University, Dec 2006
- [8] "Theoretical Concepts In Physics," M.S. Longair, Cambridge University Press 1984
- [9] "Adaptive Control of Load Shedding Relays Under Generation Loss Conditions", B. Fox, J.G. Thompson, C.E. Tindall, The Queens University of Belfast IEEE Transactions
- [10] "Design of Load Shedding Schemes Against Voltage Instability", C. Moors, D. Lefebvre, T. Van Cutsem, IEEE Transactions 2000
- [11] "Automatic Load Shedding in Power Systems", N. Perumal, A. Che Amran, National Power and Energy Conference 2003, Bangi, Malaysia
- [12] "An Intelligent Load Shedding (ILS) System Application in a Large Industrial Facility", F. Shokooh, J.J. Dai, S. Shokooh, J. Tastet, H. Castro, T. Khandelwal, G. Donner, IEEE 2005
- [13] "Power Generation Operation and Control," Wood, Allen J. Wollenburg, Bruce F., John Wiley and Sons 1996

- [14] "Power System Stability and Control" P. Kundur, McGraw-Hill 1994
- [15] "IEEE Standard for Interconnecting Distributed Resources with Electric Power Systems", IEEE-SA Standards Board, June 12th 2003
- [16] "Synchronized Phasor Data Based Energy Function Analysis of Dominant Power Transfer Paths in Large Power Systems", Joe H. Chow, Aranya Chakraborty, Murat Arcak, Bharat Bhargava, and Armando Salazar, IEEE TRANSACTIONS ON POWER SYSTEMS
- [17] "E-SIME- A Method for Transient Stability Closed-Loop Emergency Control: Achievements and Prospects", Mania Pavella, Louis Wehenkel, Daniel Ruiz-Vega, Damien Ernst, Mevludin Glavic, Bulk Power System Dynamics and Control - VII, August 19-24, 2007
- [18] "Real-Time Detection of Angle Instability using Synchrophasors and Action Principle", Michael Sherwood, Dongchen Hu, Vaithianathan "Mani" Venkatasubramanian, Bulk Power System Dynamics and Control-VII, August 19-24, 2007
- [19] "WACS-Wide-Area Stability and Voltage Control System: R&D and Online Demonstration", Carson W. Taylor, Dennis C. Erickson, Kenneth E. Martin, Robert E. Wilson, Vaithianathan Venkatasubramanian, IEEE Proceedings, Vol. 93, No. 5, May 2005
- [20] "Least action principle for mitigation of angle instability in power systems", M.S. thesis, School of EECS, Washington State University, Pullman, WA 99164, December 2008.
- [21] "The Energy Integral Criterion of Transient Stability Limits of Power Systems." P.D. Aylett, *Proceedings IEEE*, 105(C), pp. 527-536, 1958.
- [22] "Power System Stability", E.W. Kimbark, John Wiley & Sons, Inc., New York, NY. 1945.
- [23] "A Practical Method for Direct Analysis of Transient Stability", T. A. Athay, V. R. Sherket, R. Podmore, S. Virmani, and C. Puech, *IEEE Trans. PAS-98*, pp. 573-584, 1979.

- [24] “Transient Stability of a Multi- machine Power System, Part I: Investigation of System Trajectories,” A. A. Fouad and S. E. Stanton, *IEEE Transactions PAS-100*, pp. 3408-3416, 1981.
- [25] “Transient Stability of a Multi- machine Power System, Part II: Critical Transient Energy,” A. A. Fouad and S. E. Stanton, *IEEE Transactions PAS-100*, pp. 3417 - 3424, 1981.
- [26] “Power system transient stability using individual machine energy functions”, Michel, A. Fouad, A. Vittal, V., *IEEE Transactions on Circuits and Systems*, Volume 30, Issue 5, pp. 266 – 276, May 1983.
- [27] “Transient Stability Monitoring for Electric Power Systems Using Partial Energy Functions,” S. E. Stanton, *IEEE Transactions on Power Systems*, Vol. 4, No. 4, pp. 1389-1395, 1989.
- [28] “Analysis of a Local Transient Control Action by Partial Energy Functions,” S. E. Stanton and W. P. Dykas, *IEEE Transactions on Power Systems*, Vol. 4, No. 3, pp. 996-1002, 1989.
- [29] “Application of phasor measurements and partial energy analysis in stabilizing large disturbances”, S.E. Stanton, C. S. Livinsky, K. Martin, and J. Nordstrom, *IEEE Transactions on Power Systems*, Volume 10, Issue 1, pp. 297 – 306, Feb 1995.
- [30] “Synchronized Phasor Data Based Energy Function Analysis of Dominant Power Transfer Paths in Large Power Systems”, J.H. Chow, A. Chakraborty, M. Arcak, B. Bhargava, and A. Salazar, *IEEE Summer Power Meeting*, Montreal, Canada, June 2006.
- [31] *Theoretical Physics*, G. Joos and I. M. Freeman, Hafner Publishing Company, New York, 1950.
- [32] “When action is not least”, C.G. Gray and E.F. Taylor, accepted by *Journal of Physics*, at <http://www.eftaylor.com/pub/Gray&TaylorGK.pdf>.

8. APPENDIX

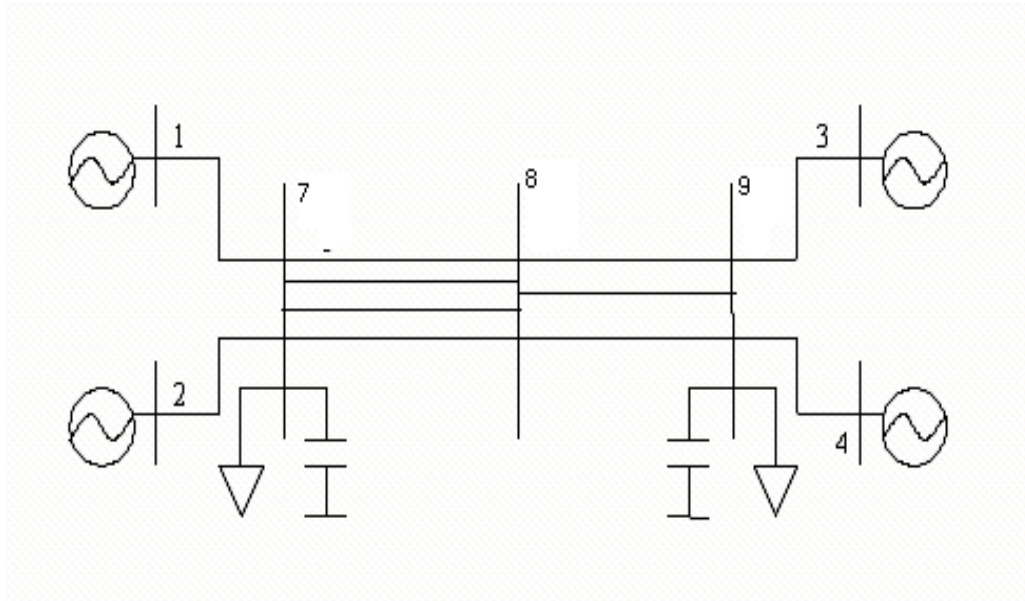


Figure A- 1: Two-area test system [14]

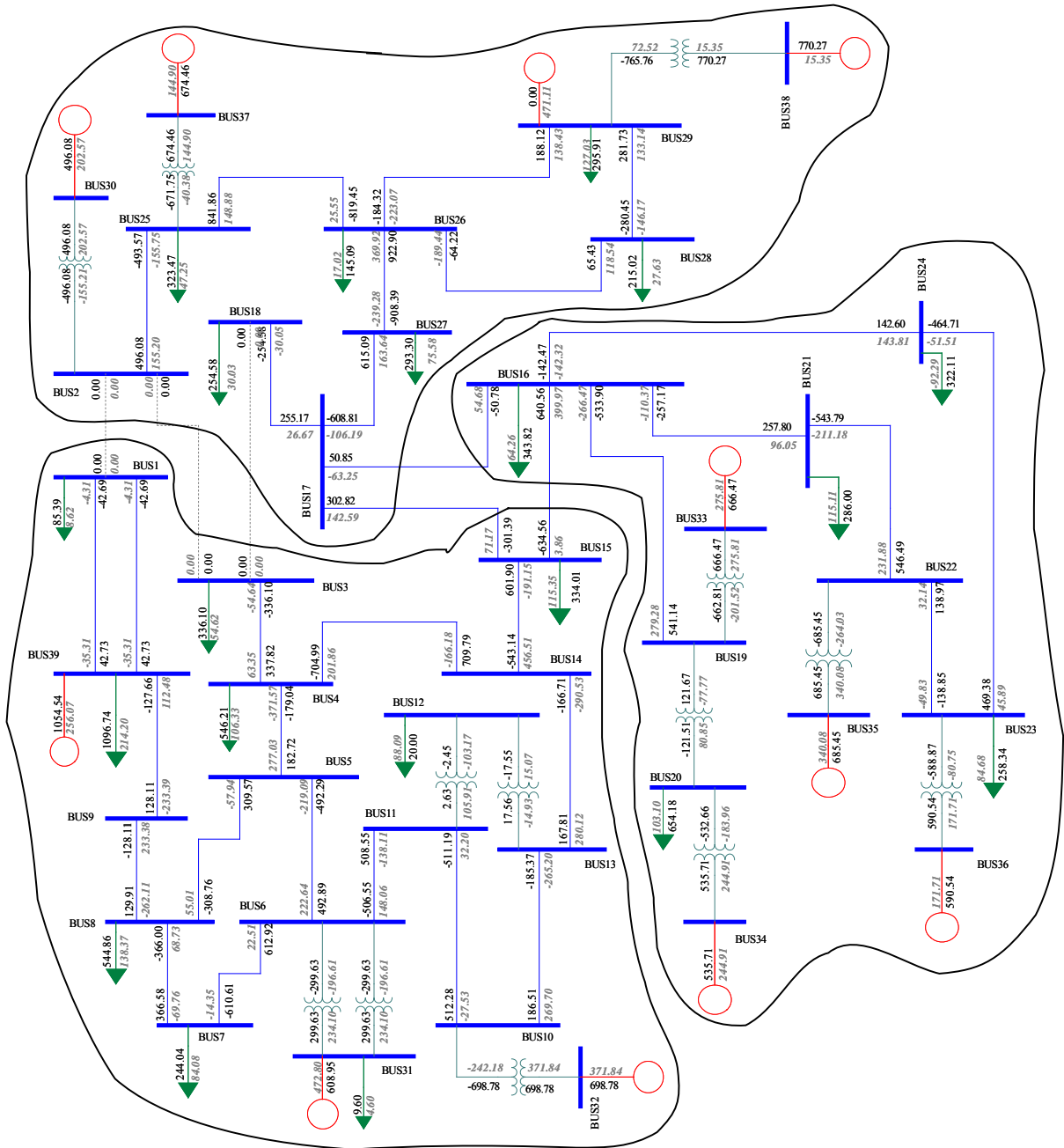


Figure A- 2: 39 Bus 3 Area Test Case

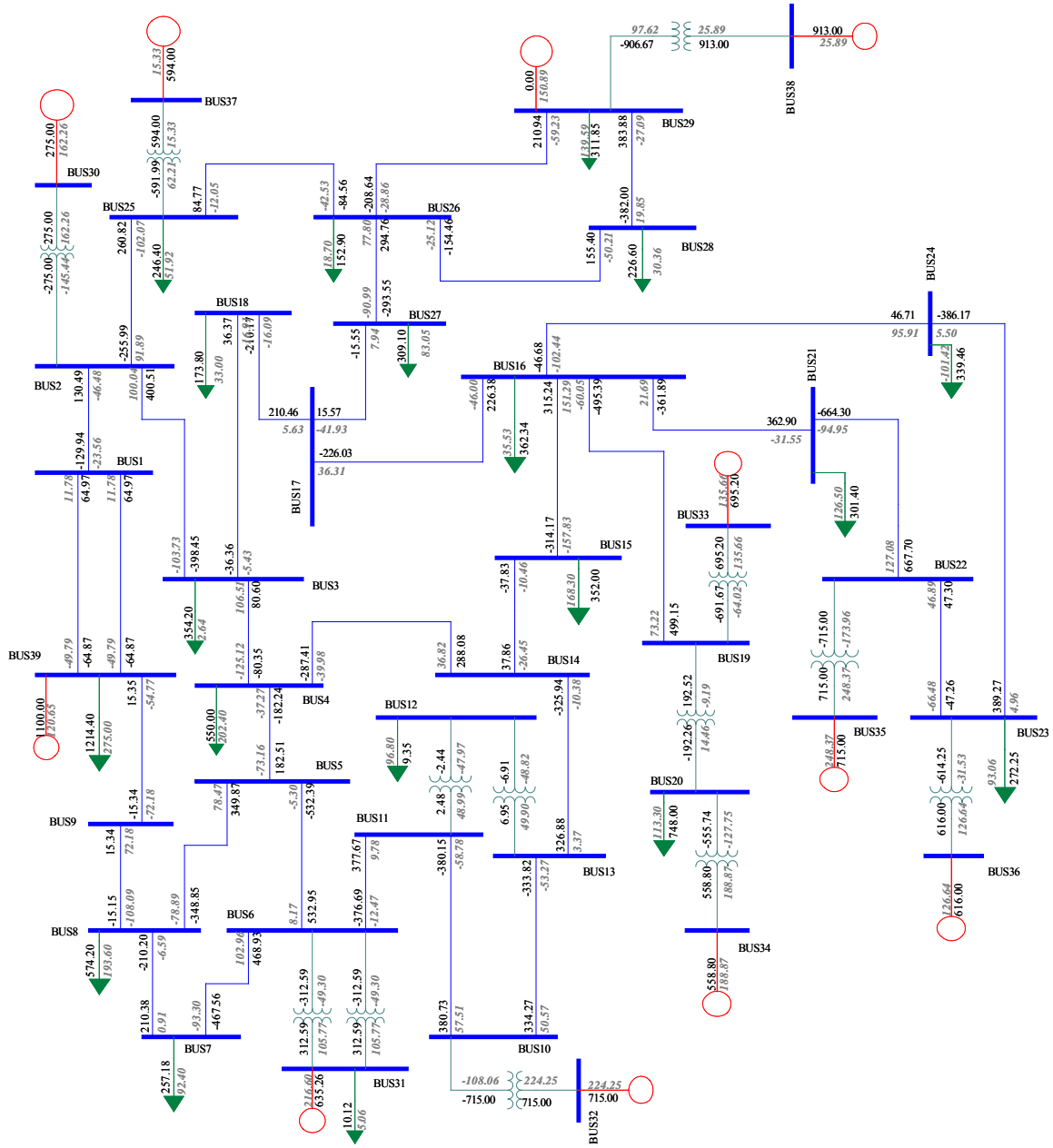


Figure A- 3: Original New England 39 Bus System

Table A- 1: 39 Bus Overload Contingencies

	39 Bus Overload Contingencies		
	Unstable Contingencies		Stable Contingencies
Cont 1	At Time 5 Seconds	Cont 1	At Time 5 Seconds
	Remove Line 16 to 17		Remove Line 17 to 15
Cont 2	At Time 5 Seconds	Cont 2	At Time 5 Seconds
	Ramp Load bus 4 15%		Ramp Load bus 4 15%
	Change Governor Reference bus 35 40MW		Change Governor Reference bus 35 40MW
	Remove Line 4 to 14		At Time 10 Seconds
	At Time 10 Seconds		Remove Line 10 to 13
	Remove Line 10 to 13		
	Remove Line 7 to 8		
Cont 3	At Time 5 Seconds	Cont 3	At Time 5 Seconds
	Change Governor Reference bus 38 60MW		Change Governor Reference bus 38 60MW
	Ramp Load bus 16 10%		Ramp Load bus 16 10%
	At Time 20 Seconds		At Time 20 Seconds
	Remove Line 15 to 16		Remove Line 17 to 15
Cont 4	At Time 5 Seconds	Cont 4	At Time 5 Seconds
	Change Governor Reference bus 36 40MW		Change Governor Reference bus 36 40MW
	Change Governor Reference bus 34 40MW		Change Governor Reference bus 34 40MW
	Ramp Load bus 15 40%		Ramp Load bus 15 40%
	At Time 15 Seconds		At Time 15 Seconds
	Remove Line 13 to 14		Remove Line 13 to 14
	Remove Line 10 to 13		Remove Line 10 to 13
	At Time 20 Seconds		
	Remove Line 16 to 17		

Table A- 2: Exciter Parameters

39 Bus Exciter Data													
IBUS	KA	TA	VRMAX	VRMIN	KE	TE	KF	TF	E1	SE(E1)	E2	SE(E2)	MVA Base
38	5	0.06	3	-3	1	0.25	0.04	1	3.55	0.08	4.73	0.26	100
37	40	0.02	10.5	-10.5	1	1.4	0.03	1	4.26	0.62	5.68	0.85	100
36	5	0.02	4	-4	1	0.528	0.0854	1.26	3.19	0.072	4.26	0.282	100
35	40	0.02	6.5	-6.5	1	0.73	0.03	1	2.8	0.53	3.74	0.74	100
34	5	0.02	5	-5	1	0.471	0.0754	1.25	3.59	0.064	4.78	0.251	100
33	40	0.02	10	-10	1	0.785	0.03	1	3.93	0.07	5.24	0.91	100
32	5	0.06	3	-3	1	0.5	0.08	1	2.87	0.08	3.82	0.314	100
31	5	0.06	3	-3	1	0.5	0.08	1	2.34	0.13	3.12	0.34	100
30	6.2	0.05	3	-3	0	0.405	0.057	0.5	3.03	0.66	4.05	0.88	100

Table A- 3: 39 Bus Governor Parameters

Governor Parameters											
IBUS	PFL	R	T1	T2	T3	VMIN	Dt	Pgen	Pmax		
38	100	0.35	0.1	0	0	0	0	770.3	9999		
37	100	0.26	0.1	0	0	0	0	674.5	9999		
36	100	0.24	0.1	0	0	0	0	590.5	9999		
35	100	0.24	0.1	0	0	0	0	685.5	9999		
34	100	0.2	0.1	0	0	0	0	535.7	9999		
33	100	0.25	0.1	0	0	0	0	666.5	9999		
32	100	0.3	0.1	0	0	0	0	698.8	9999		
31	100	0.3	0.1	0	0	0	0	631.1	9999		
30	100	0.22	0.1	0	0	0	0	535.1	9999		

Table A- 4: Generator 1 to 9 Parameters

Two Axis Model Parameters for Generators 1 to 9													
IBUS	T'do	T''do	T'qo	T''qo	H	D	Ra	Xd	Xq	X'd	X'q	Xl	MVA Base
38	4.79	0	1.96	0	34.5	1	0.0015	0.211	0.205	0.057	0.059	0.03	100
37	6.7	0	0.41	0	24.3	1	0.0015	0.29	0.28	0.057	0.091	0.028	100
36	5.66	0	1.5	0	26.4	1	0.0015	0.295	0.292	0.049	0.186	0.032	100
35	7.3	0	0.4	0	34.8	1	0.0015	0.254	0.241	0.05	0.081	0.022	100
34	5.4	0	0.44	0	26	1	0.0015	0.67	0.62	0.132	0.166	0.054	100
33	5.69	0	1.5	0	28.6	1	0.0015	0.262	0.258	0.044	0.166	0.03	100
32	5.7	0	1.5	0	35.8	1	0.0015	0.25	0.237	0.053	0.088	0.03	100
31	6.56	0	1.5	0	30.3	1	0.0015	0.295	0.282	0.07	0.17	0.035	100
30	5.3	0	1.5	0	20	1	0.0015	0.262	0.258	0.044	0.166	0.03	100

Table A- 5: Generator 10 Classical Model Parameters

Generator 10 Parameters					
IBUS	MVA	Ra	X'd	H	KD
39	100	0	0.02	70	0

Part II

Online Voltage Stability Margin Monitoring Using Synchrophasor Measurements and Statistical Multi-Linear Regression Models

Venkataramana Ajjarapu, Professor

Bruno Leonardi, Ph.D. Student

Iowa State University

Information about this project

For information about this project contact:

Venkataramana Ajjarapu

David C. Nicholas Professor

Department of Electrical and Computer Engineering

Iowa State University

Ames, Iowa, 50011

Ph: 515-294-7687

E-mail: vajjarap@iastate.edu

Power Systems Engineering Research Center

The Power Systems Engineering Research Center (PSERC) is a multi-university Center conducting research on challenges facing the electric power industry and educating the next generation of power engineers. More information about PSERC can be found at the Center's website: <http://www.pserc.org>.

For additional information, contact:

Power Systems Engineering Research Center

Arizona State University

577 Engineering Research Center

Tempe, Arizona 85287-5706

Phone: 480-965-1643

Fax: 480-965-0745

Notice Concerning Copyright Material

PSERC members are given permission to copy without fee all or part of this publication for internal use if appropriate attribution is given to this document as the source material. This report is available for downloading from the PSERC website.

© 2010 Iowa State University. All rights reserved.

Table of Contents

1.	Introduction.....	1
1.1.	Overview of the Problem	1
1.2.	Relationship Between Reactive Power Reserves and Voltage Stability Margin..	3
1.2.1.	Q_{RCM} - Constant Maximum Reactive Power.....	3
1.2.2.	Q_{RCC} – Capability Curve	4
1.2.3.	Q_{RVL} – Minimum Voltage Limit	5
1.2.4.	Q_{RCL} – Voltage Collapse Limit	6
1.3.	Background on Phasor Measurement Unit (PMU).....	6
1.3.1.	Historical Developments	7
2.	Proposed Methodology	10
2.1.	MLRM for Online VSM Estimation.....	10
3.	Theoretical Background.....	17
3.1.	Multi-Linear Regression Models (MLRM)	17
3.2.	Artificial Neural Networks (ANN)	21
3.3.	Data Pre-Processing and Feature Extraction.....	25
3.4.	Data Flow along ANN and MLRM	26
3.5.	Online Implementation of the Methodology.....	27
4.	Studied Cases and Discussion.....	29
4.1.	IEEE 30 – Bus Test Case	29
4.2.	PSS/E Bench [®] - Bus Test Case.....	37
5.	Conclusions.....	53
	References	54
	Project Publications	58
	Appendix A.....	59

List of Figures

FIG 1: FIRST QUADRANT OF A CAPABILITY CURVE OF SYNCHRONOUS MACHINE	4
FIG 2: PV-CURVE DISPLAYING POINTS OF INTEREST	5
FIG 3: BLOCK DIAGRAM OF FIRST PMU PROTOTYPE DEVELOPED [39].....	8
FIG 4: PMU BLOCK DIAGRAM MODEL [36]	8
FIG 5: STEADY STATE STABILITY BOUNDARY IN LOAD SPACE.....	12
FIG 6: ONE MLRM COVERING ALL POSSIBLE SCENARIOS AND CONTINGENCIES	13
FIG 7: MLRMS FOR DIFFERENT SCENARIOS AND CONTINGENCY.....	13
FIG 8: LINEAR DEPENDENCE CHECKING.....	20
FIG 9: FLOWCHART DESCRIBING THE WHOLE METHODOLOGY.....	21
FIG 10: ARTIFICIAL NEURAL NETWORK STRUCTURE	22
FIG 11: ANN PARAMETER REPRESENTATION.....	23
FIG 12: DATA FLOW ACROSS ANN AND MLRM	26
FIG 13: OFF/ONLINE OVERALL METHODOLOGY.....	27
FIG 14: RESIDUAL DISTRIBUTION.....	30
FIG 15: RESIDUAL HISTOGRAM	31
FIG 16: REGRESSED VSM VERSUS ACTUAL VSM	32
FIG 17: CONFIDENCE BOUNDS OF A NORMALLY DISTRIBUTED RANDOM VARIABLE [40].	34
FIG 18: AREA 2 AND ITS NEIGHBORING AREAS	38
FIG 19: RESIDUAL DISTRIBUTION.....	40
FIG 20: RESIDUAL HISTOGRAM	40
FIG 21: REGRESSED VARIABLE VS. ACTUAL VARIABLE	41
FIG 22: RESIDUAL DISTRIBUTION.....	44
FIG 23: RESIDUAL HISTOGRAM	45
FIG 24: REGRESSED VALUES VS. ACTUAL VALUES OF VSM.	46
FIG 25: OUTPUT ERROR OF ANN FOR DIFFERENT CONDITIONS AND MEANS SQUARED TRAINING ERROR.....	51

List of Tables

TABLE I: MLRM DEFINITION	16
TABLE II: CONTINGENCY GROUPING METHODOLOGY	25
TABLE III: POWER SYSTEM DESCRIPTION	29
TABLE IV: DISTRIBUTION PARAMETERS	31
TABLE V: ANOVA TABLE.....	32
TABLE VI: CONFIDENCE INTERVALS	33
TABLE VII: MLRMs TESTING	34
TABLE VIII: ANN TESTING	36
TABLE IX: POWER SYSTEM DESCRIPTION	37
TABLE X: SELECTED REACTIVE POWER RESERVES (RPR)	38
TABLE XI: DISTRIBUTION PARAMETERS	41
TABLE XII: ANOVA	42
TABLE XIII: CONFIDENCE INTERVALS	43
TABLE XIV: ESTIMATED VALUES.....	43
TABLE XV: DISTRIBUTION PARAMETERS	45
TABLE XVI: ANOVA	46
TABLE XVII: CONFIDENCE INTERVALS	47
TABLE XVIII: ESTIMATED VALUES	48
TABLE XIX: ARTIFICIAL NEURAL NETWORK TESTING	50

1. Introduction

1.1. Overview of the Problem

Although voltage instability phenomenon has been studied for many years and much insight has been obtained on the phenomenon, it is still a threat to modern power systems all around the world. Recent blackouts such as the ones that occurred in North America on July 1996 and August 2003 and in Chile on May 1997 clearly evidenced that voltage instability remains a threat, and that proper reactive power management is essential for safe, reliable and continuous operation of the bulk power system.

Many of the tools utilized for voltage stability analysis are computationally demanding and hardly implemented in real-time operations. Voltage stability assessment is usually performed by stressing the system load/generation along a specific load/generation increase scenario and repeating the process for a few different network topologies. Such approach certainly does not cover many of the uncertainties involved in real-time operations and a comprehensive analysis cannot be obtained. Therefore, new tools that would account for some of the uncertainties involved in real-time operations and provide proper monitoring of voltage stability margin seem to be necessary.

Due to all the uncertainties involved in daily operations in a control center, the development of an online voltage stability monitoring tool becomes a challenging task. Such online voltage stability margin (VSM) monitoring tool must consider several possible network topologies, generation dispatch conditions and load levels that can occur during a time span. It must also be fast enough to provide quick estimations of VSM and should also be able to model errors involved in VSM estimation, by providing operators with confidence bounds of the estimated VSM values.

The smart grid initiative, which is a key portion in the Energy Independence and Security Act of 2007 [1]-[2], is expected to bring innovation and new practices to the power grid. In order to keep the pace of technical evolution and deployment of new devices across the power system, a new niche of monitoring and control applications are on the verge to be developed. Such modernization of the grid will require new applications to handle operational issues created by the deployment of those new devices and practices.

After the 2003 North American blackout [3], the Federal Energy Regulatory Commission (FERC) and the North American Electric Reliability Corporation (NERC) have issued standards in order to better monitor the amount of reactive power resources and closely control voltage within a specified region of the system [4]-[5].

The reactive power reserve monitoring initiative definitively improved the awareness of operators by qualitatively linking large amounts of reactive power reserves (RPRs) to safe operation. However, it did not provide any quantitative information about how much VSM a specific area has based on the amount of RPRs that is available. In addition to that, many ISOs, RTOs and utilities are inquiring themselves about what to do with the large amount of raw data (voltage magnitudes,

active/reactive power flow in lines, reactive power reserves, breaker statuses, etc) daily gathered in their SCADA/EMS.

Given the challenges and needs presented above, it would be helpful to have tools that can transform raw data (e.g., voltage values, reactive power reserves) into meaningful information to system operators. The objective is to develop a tool that processes a large amount of raw data and provides more quantitative, meaningful and concise information.

Many data driven techniques have been proposed in order to estimate VSM. Artificial neural networks (ANN) have been successfully used for that purpose [6]-[11]. Although good accuracy is achieved by these ANN techniques, a neural network is used for each system topology (or for a few different topologies), which makes the practical implementation cumbersome, as a large number of network topologies can emerge on real-time operations, requiring therefore a large number of ANNs. Another, despite the fact that the ANNs are capable of generalizing for unforeseen load patterns, the output value does not contain any information or confidence bounds about the error in estimation. So once the ANN produces the estimation, the user has no idea of how much that estimated amount can be off.

Other voltage collapse detection techniques do not attempt to predict the amount of VSM but rather, they try to verify if the proximity of collapse by the calculation of indexes. Several PMU based techniques and Thevenin equivalent techniques fall into this category [12]-[15]. The idea supported by those techniques is to calculate an index in real-time and compare it to a threshold. Based on the comparison, the system is classified as secure or insecure. Although accurate and fast indexes have been developed, such techniques are mainly applied locally at load buses or radial transmission corridors and are not suitable to assess wide area voltage stability. Also, they are not capable of estimating how much voltage stability margin is still available in the system in MW.

Techniques based on the singular value decomposition of the Jacobian matrix are also employed to obtain a proximity to voltage collapse. These techniques are based on the calculation of the minimum singular value of the Jacobian and instability is characterized when the smallest singular value becomes zero, implying singularity of the Jacobian matrix. It requires a current power flow solution of the system from time to time, which is sometimes hard to obtain in an online environment due to state estimator convergence issues or problems to find proper correspondence among elements in node/breaker model and bus/branch model after topology processing [16]. Another restriction to these methods is that each linearization of the Jacobian represents a unique system condition. It could slow down the analysis since system condition changes all the time and the process must be iteratively repeated.

The technique proposed in this research intends to create several MLRM for online VSM monitoring. It was inspired by a previous work where reactive power reserves were linked to voltage stability margin by an equivalent reactive power reserve [19]. In our approach, the MLRMs will correlate the amount of RPRs available at critical machines with the amount of VSM of a certain area of the system. Each MLRM is designed for a specific set of contingencies with similar VSM and is expected to

estimate VSM with reasonable accuracy for a wide range of operating conditions (several possible load increase patterns around a central one).

The MLRM are designed offline and are intended to cover a wide range of possible day/week/month-ahead load and generation patterns, as well as large number of system contingencies. A selection of what MLRM needs to be used at each moment will be carried out by an ANN. Such ANN will analyze current system data collected from PMUs in the system and define what MLRM is more appropriate to be used at each instant, depending on current system condition. A more detailed description of MLRMs and ANNs is given in section 3.

1.2. Relationship Between Reactive Power Reserves and Voltage Stability Margin

Although a relationship between reactive power reserves and voltage stability margin has been observed, there is no mathematical correspondence between these two variables. In order to confirm the relationship between reactive power reserves and voltage stability margin, several studies were carried out trying to create a model that could represent such relationship. The first step was to investigate how different reactive power reserve definitions relate themselves with voltage stability margin. After identified the most appropriate definitions of RPR, they are used on the development of the MLRM for real-time VSM estimation.

Aiming to identify the most useful forms of RPR, four different RPR definitions were investigated in this work [17]:

- Q_{RCM} - w.r.t constant maximum reactive power.
- Q_{RCC} - w.r.t capability curve.
- Q_{RVL} - w.r.t minimum voltage limit.
- Q_{RCL} - w.r.t voltage collapse limit.

1.2.1. Q_{RCM} - Constant Maximum Reactive Power

This type of definition of RPR is the one generally used in power flow studies. A maximum and minimum limit of reactive power that each machine can supply is defined. Those values are constant during the power flow solutions and the RPR is can be defined as:

$$Q_{RCM}^i = Q_{\max}^i - Q_{\text{current}}^i \quad (1.1)$$

Where: Q_{RCM}^i - Reactive reserve of machine i .

Q_{\max}^i - Maximum reactive power of machine i .

Q_{current}^i - Current reactive power dispatched by machine i .

Fig 1 shows the first quadrant of a capability curve of a synchronous machine. Only the first quadrant of the capability curve was shown in detail because generators are usually providing reactive power under high loading conditions, although some of them may be operating in the 4th quadrant and consequently,

absorbing reactive power.

This definition of RPR can be seen in Fig 1 as the distance from point *a* to the horizontal line where Q_{rated} is defined on the ordinate. The value chosen to be the maximum reactive power limit is usually the reactive power that can be supplied at rated power factor. The rated power factor of the machine is shown in Fig 1 as the intersection of the armature and field heating limits. This definition of reactive power reserve may underestimate the real reactive power reserve available for it limits the maximum reactive power capability before the field heating limit constraint is reached.

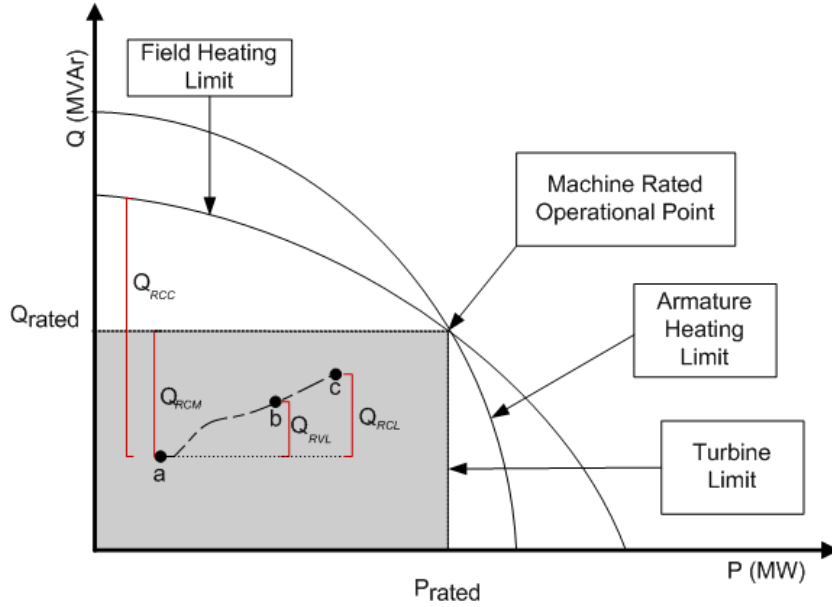


Fig 1: First quadrant of a capability curve of synchronous machine

1.2.2. Q_{RCC} – Capability Curve

Another definition of reactive reserve can be made by using the capability curve. This definition better represents the true amount of reactive power reserve available because it considers the capability curve of the machine. This approximation is used by some utilities for providing more realistic information about the amount of reactive power available. This and the previous definition are also termed as *technical* reactive power reserve [18]. The reactive reserve using the capability curve can be defined as:

$$Q_{RCC}^i = Q_{maxcc}^i(P) - Q_{current}^i \quad (1.2)$$

Where: Q_{RCC}^i - Reactive reserve of machine *i*.

$Q_{\max cc}^i(P)$ - Maximum reactive power of machine i at active power dispatch P .

$Q_{current}^i$ - Current reactive power dispatched by machine i .

This definition of RPR can be seen in Fig 1 as the distance between point a and the field heating limit. In this definition, the maximum reactive power that can be provided by the machine varies as function of the active power being dispatched. This definition usually provides extra reactive power reserve when compared to the constant maximum reactive power reserve definition as seen in Fig 1.

1.2.3. Q_{RVL} – Minimum Voltage Limit

This reserve definition was created in order to address the required amount of RPR needed in order to maintain proper voltage profile across the system. Fig 2 represents a typical PV curve. The x-axis represents the total load increased in a specific area whereas the y-axis represents the voltage magnitude at any load bus inside that area. The points specified as a , b and c in Fig 2 are the same points a , b and c defined in Fig 1.

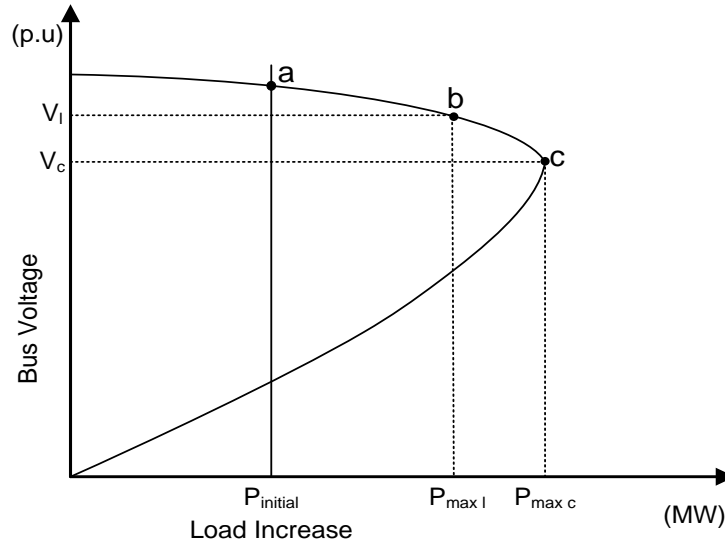


Fig 2: PV-curve displaying points of interest

Q_{RVL} is defined as the reactive power dispatched by the machine at point b (the point where the voltage hits a defined low limit V_l) in Fig 1 and Fig 2, minus the reactive power dispatched by the machine at point a in Fig 1 and Fig 2. This definition can be used to predict how much RPR is necessary to be maintained to avoid voltage violations in the system.

$$Q_{RVL}^i = Q_{vlim}^i - Q_{current}^i \quad (1.3)$$

Where: Q_{RVL}^i - Reactive reserve of machine i with respect to voltage.

Q_{vlim}^i - Reactive power dispatched from machine i at the point of minimum voltage limit.

$Q_{current}^i$ - Current reactive power dispatched from machine i .

1.2.4. Q_{RCL} – Voltage Collapse Limit

Similar to the previous definition, if we consider the point of collapse as the limit, the RPR can also be defined as the amount of reactive power dispatched by the machine at point of voltage collapse (point c in Fig 2) minus the current reactive power dispatched by the machine (point a in Fig 2). This is called *effective* reactive power reserve according to [18]. This definition takes into account the fact that some generators still have reactive power reserves when the system faces voltage collapse. Although that remaining reactive power reserve is available, it cannot be used. This reactive power reserve definition is given by (1.4) below.

$$Q_{RCL}^i = Q_{vcol}^i - Q_{current}^i \quad (1.4)$$

Where: Q_{RCL}^i - Reactive reserve of machine i .

Q_{vcol}^i - Maximum reactive power of machine i at point of voltage collapse.

$Q_{current}^i$ - Actual reactive power dispatch of machine i .

This definition of RPR is important because it considers the reactive power dispatch at the point of collapse.

After having presented all four definitions of RPR, the relationship of each one of them with VSM was investigated. It was observed that the RPR definitions with respect to voltage limit and voltage collapse limit have better linearity and accuracy compared to the other two definitions. Although higher accuracy is achieved, real-time implementation of those two definitions cannot. The reason is because the maximum operational point used in those two definitions (Q_{vlim} and Q_{vcol}) is unknown during online applications. Therefore, the constant maximum reactive limit and the capability based definition will be used in this work for online applications, for they can be easily monitored.

1.3. Background on Phasor Measurement Unit (PMU)

This section provides information about the historical developments of PMU devices as well as the basic description of its functional operation.

1.3.1. Historical Developments

PMUs have its origins in the development of the Symmetrical Component Distance Relay (SCDR) in the early 1970s. The invention of the symmetrical component distance relay (SCDR) was due to the fact that microcomputers could not handle the requirements of a distance relay algorithm at that time. The SCDR used symmetrical components of voltages and currents in order to convert the 6 fault equations of a three phase transmission line into a single equation using symmetrical components.

In early 1980s, the deployment of GPS satellites was already significant. This fact enabled engineers to use GPS time signals as inputs to the sampling clocks in the measurement system of digital relays. This would offer a common time base for all the measurements across a wide area of the system.

After the catastrophic failure of the North-Eastern power grid in North America in 1965, intense research was conducted on techniques for determining the state of the power system in real-time based on real-time measurements. However, the possibility of obtaining synchronized waveform measurements in those days was practically remote. Therefore, there was a need to develop a technique that could estimate the current state of the power system. This technique relied on measurements obtained by sequential scans of system's variables. By utilizing those measurements, the state of the power system could be estimated by a non-linear state estimator [37]-[38].

The first practical PMU prototype was developed at the Power System Research Laboratory of Virginia Tech and the first commercial unit was built by Macrodyne[®] in the early 90s. The block diagram of the PMU prototype built at Virginia Tech is presented in Fig 3, while the PMU block diagram of the Macrodyne[®] 1620 is presented in Fig 4.

Phasor Measurement Unit (PMU) utilizes a GPS clock signal to synchronize the sampled measurements obtained from the system. By doing so, all the measurements will have a time tag with the same time reference. The accuracy of the synchronization is estimated to be around $1\mu\text{s}$ theoretically. This accuracy could not be achieved in practical applications. Despite the theoretical accuracy could not be achieved, the error in PMU's time synchronization was still small enough for most power system applications.

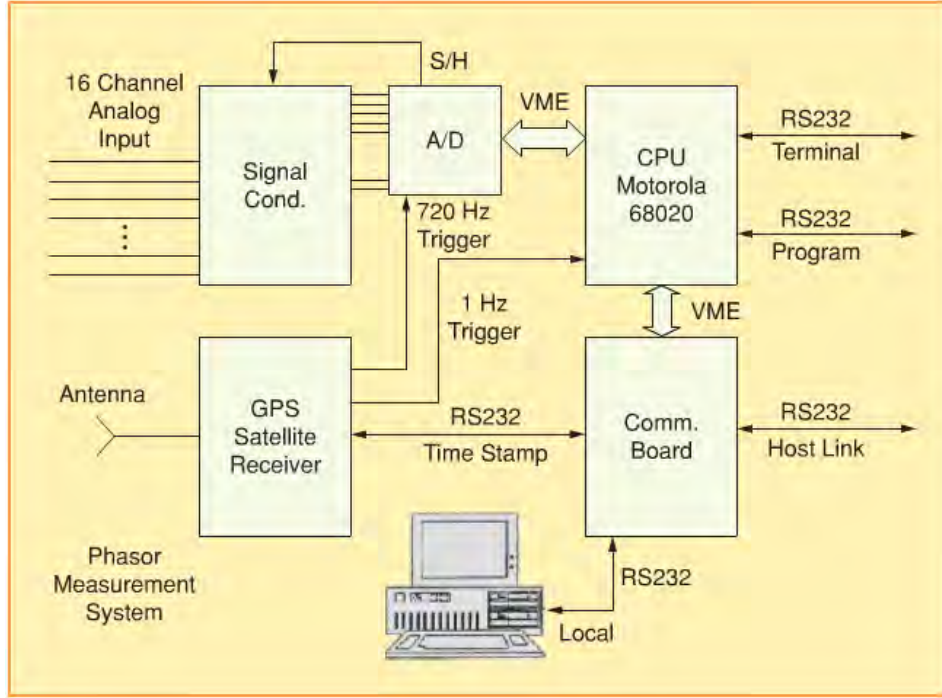


Fig 3: Block diagram of first PMU prototype developed [39]

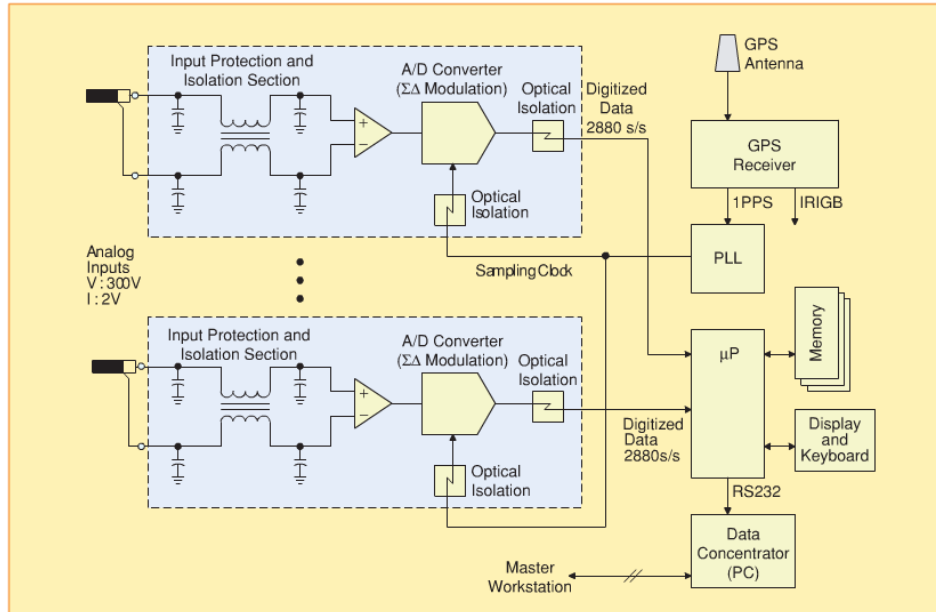


Fig 4: PMU Block diagram model [36]

A basic description of how a PMU works is given in the sequence. Analog voltage and current magnitudes are stepped down using potential and current transformers respectively. Once the magnitudes of the signals have a reduced amount of energy, they go through the preprocessing stage. This preprocessing stage

includes anti-aliasing filters, noise filters and other specific preprocessing stages as required. After the waveforms are pre-processed, they are sampled and digitalized using an A/D converter. The sampling event tags the samples with a time stamp provided by the GPS clock. Once the data is synchronized and digitalized, it can be utilized in a local working station or made available to a computer network. Once a considerable amount of measurements from a wide area of the system are made available, computer applications that make use of such measurements in real-time can be developed.

After presenting the basic operation of a PMU unit, a detailed description of the objectives of this project and the problem of real-time voltage stability analysis using PMU data is given in the sequence.

2. Proposed Methodology

2.1. MLRM for Online VSM Estimation

After years of collecting information and carefully analyzing data about voltage collapse events, IEEE/CIGRE created a task force on stability to classify voltage stability accordingly to the specific causes of perturbation and time duration of occurrence [20]-[22]. As far as the causes of voltage instability are concerned, two main categories were created: large disturbance or small disturbance voltage instability. On the other hand, time duration of the phenomenon has originated two different classifications of the phenomenon named short term and long term voltage instability.

After voltage stability scenario is classified using the definitions above, appropriate applications and techniques can be used to analyze the disturbance depending on its classification. PV curve, continuation power flow, QV curve, long term dynamic simulations, quasi steady state simulation, Thevenin equivalent reduction and eigenvalue analysis are amongst the most popular techniques to analyze voltage stability of a power system.

Since many of those techniques are computationally demanding, their application in the real-time environment becomes a challenging task. Several new algorithms with improved processing speed have been proposed for the aforementioned techniques. However, due to the large number of scenarios and possible load patterns that need to be analyzed in real-time, simulation of a large number of system conditions still poses a limitation to most of those techniques. Also, the intrinsic deterministic properties of those tools do not enable them to account for probabilistic characteristic of the phenomena, such as how system load varies around forecasted load values.

The main motivation behind this work was to define an approach that would be suitable to estimate VSM in real-time. Such tool was designed with the intention to fulfill the following requirements:

- It must make use of the data (including PMU data if available) that is brought into the control centers and should not rely on a current power flow case in real-time.
- It must also be flexible enough to cover a wide range of operating scenarios (load increase patterns) and system network topologies.
- It must represent wide-area voltage stability proximity estimation, in contrast to local indexes that have been proposed in the literature.
- It should properly model the error implicit in the estimated voltage stability margin value.

With all the requirements aforementioned in mind, an attempt was made to develop this voltage stability monitoring methodology utilizing MLRM. The design of the MLRMs is performed off line, thereby considering a wide spectrum of operating conditions that could reflect the most probable scenarios in the short term operations.

The first step of the methodology is based on the calculation of several PV curves for a large set of contingencies and load increase patterns. These scenarios will represent futuristic operating conditions and data will be collected from simulations to generate the database. Once the data base is created, the design of MLRMs and ANN will follow. In order to reduce the computational burden for many scenarios need be considered, a steady state model of the system is used. Long term acting devices such as OLTCs and switchable capacitors/inductors were modeled in the simulations. The dynamic modeling of components could be utilized and dynamic simulations could have been performed, at the price of a longer simulation time to cover all the desired conditions.

- *System Stress and Data Base Generation*

In order to stress the system up to the point of voltage collapse, system load will be increased in the system using a PV curve type of stress. As load increases, bus voltage magnitudes in the load buses start to reduce. Generators and other reactive power sources start to produce more reactive power to maintain proper voltage levels.

Since more reactive power needs to be produced to maintain system voltage profile, the amount of RPR on each generator and other reactive power sources will consequently drop. Such reactive power reserve reduction can be visualized on the upper quadrant of Fig 1. When the operational point at the base load (point *a*) moves towards a high loading condition (point *c*), the RPR of the generator is reduced for the operational point moves closer to the reactive power limits.

The above described scenario is a common situation that can be faced daily as system's load ramps up. In this project, we focused in modeling the relationship between VSM and RPR as system operating condition changes. For instance, a daily system scenario could be represented by the path from point *a* towards point *c* in Fig 1 and Fig 2. The objective was to develop a MLRM that would closely model such relationship. This MLRM would further help operators to estimate VSM by monitoring RPRs in an online fashion. After analyzing the steady state stability boundary in the load space presented in Fig 5, two distinct effects need to be captured by the technique.

When a severe contingency takes place in the system and assuming here that the system is transiently stable, the steady state stability boundary moves, for instance, from an outer curve to an inner curve as shown in Fig 5

The first effect that can reduce VSM is the stability boundary movement. Fig 5 represents a two dimensional load space used just to facilitate conceptual understanding. As can be seen, the total load that the system can supply before a contingency takes place (outer stability boundary) is usually greater than the total load that can be supplied after the contingency takes place (inner stability boundary), reinforcing the fact that contingencies affect the amount of VSM of a system.

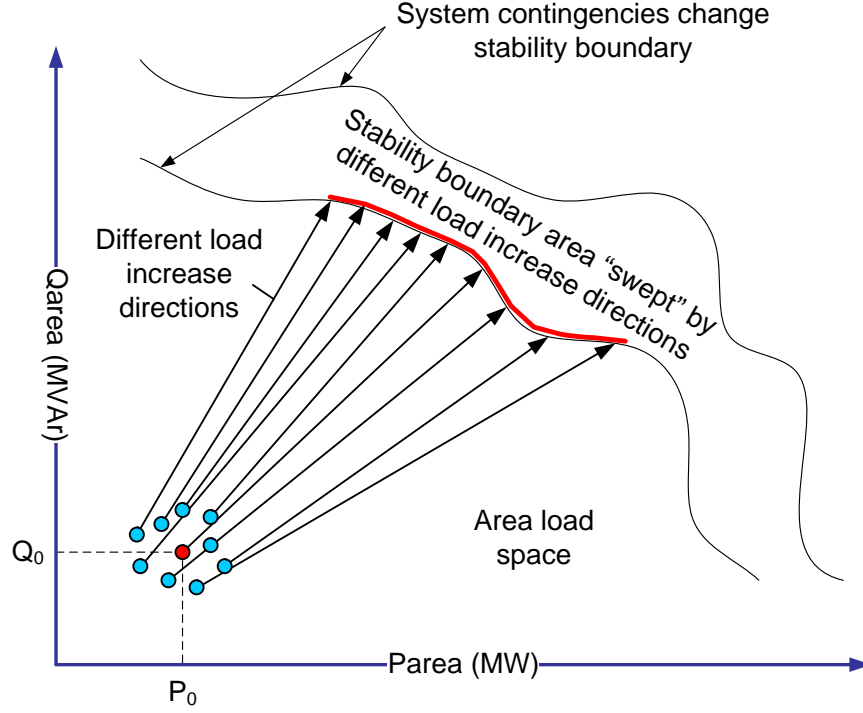


Fig 5: Steady state stability boundary in load space

Another important effect that influences VSM is the load increase direction. Depending on which direction is selected, the distance from the current loading point, represented in 0 to the steady state stability boundary differs. Simulations have shown that small perturbations on the load increase direction do not usually affect the VSM considerably, i.e. assuming the load increases at a constant rate and maintains the same rate until it reaches the stability boundary. This is an indication that the steady state stability boundary is locally smooth although its structure has not been well established yet [25]-[27]

Fig 6 shows how a RPR of a particular generator varies accordingly to VSM. Each of the dotted lines represents a contingency and each dot represents a converged power flow solution along the calculated PV curves. As can be seen, the amount of RPR reduces linearly with the amount of VSM of the system. Therefore, lower RPR situations imply in lower VSM.

Since the relationship was apparently linear, one MLRM was used in order to capture the relationship between VSM and RPR. In this first attempt, the MLRM failed to properly and accurately relate VSM with RPR. The main problem was the wide spread of data around the fitted line (solid line), which would cause large estimation errors for some scenarios, as can be seen in Fig 6.

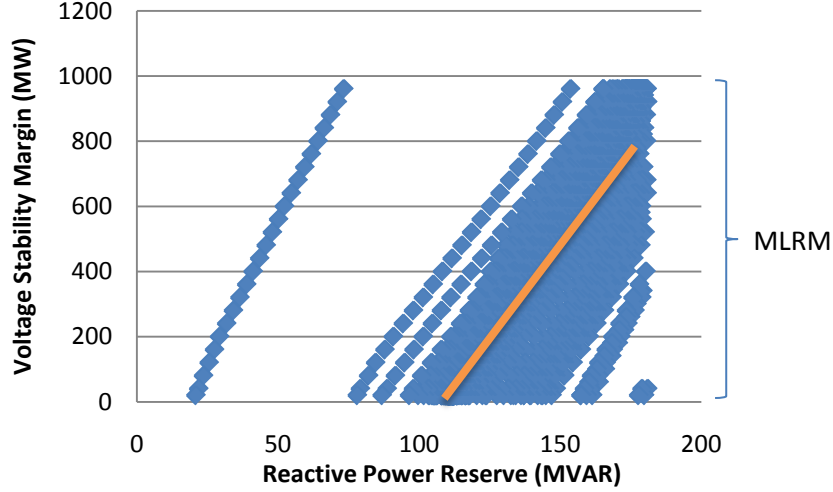


Fig 6: One MLRM covering all possible scenarios and contingencies

Therefore, it was necessary to divide the VSM range into several sub ranges as shown in Fig 7. Each one of the MLRM is expected to be used only for contingencies whose VSM is within a specified range. Ten different ranges were defined in this first approach but the amount of models can vary accordingly to the needs of the system. The ten different MLRM can be seen in Fig 7.

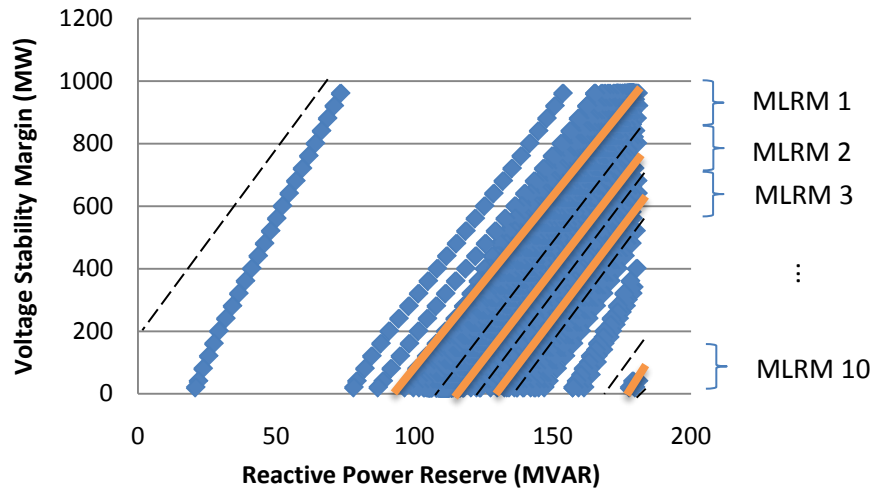


Fig 7: MLRMs for different scenarios and contingency

Once the contingencies are divided in subgroups and all the data is collected, the design of the MLRM starts. Each MLRM will be used to estimate VSM for a wide range of operating points and a defined set of critical contingencies. Each contingency set was created by grouping contingencies with similar VSM. It means

that those contingencies cause a similar variation in the stability boundary, at least locally.

Once the VSM range is divided in few sub-ranges, the accuracy problem related to data spread around the estimation lines was practically solved, as seen in Fig 7. Now each MLRM (solid line) is utilized to estimate VSM only for points within the dashed lines. However, another problem was raised by the creation of more than one model: what model should be chosen considering there is more than one MLRM available?

In order answer that question, a pattern recognition tool based on an ANN design was proposed. A multi-layered perceptron (MLP) ANN was used to identify the proper MLRM at each point in time, based on measurements taken from the system. Since the focus of this project was to develop applications that would make use of PMU measurements, bus voltages magnitudes and angles were utilized as inputs to the ANN. The output of the ANN is an index which represents what MLRM should be used.

Other real-time system measurements available in EMS/SCADA system are being investigated in order to extend the technique to system with low PMU penetration.

- *Load Increase Patterns*

The data base is generated through several PV curve calculations for a comprehensive contingency list and several load increase directions. Load increase is varied from a low load condition \mathbf{L}_L (for instance, winter forecasted load) to a high load value \mathbf{L}_H (for instance, summer forecasted load). The load increase vector is represented by the difference between \mathbf{L}_L and \mathbf{L}_H :

$$\mathbf{L}_{inc} = \mathbf{L}_H - \mathbf{L}_L = [L_1, L_2, \dots, L_N] \quad (2.1)$$

This vector is considered the central load increase direction value, represented by the vector emerging from (P_0, Q_0) in Fig 5. Since load forecasting tools usually predict the total load in a determined area of the system rather than the load at each one of the buses, there is a need to model the uncertainty involved in the load increase direction once it needs to be estimated. In order to model such uncertainty in load growth, each load bus in the load vector above was considered as a random variable with mean equal to the central load increase direction and standard deviation equal to 15% of the central load increase direction.

Once a few load increase directions are used, the stability boundary represented in the load space is swept locally as can be seen in Fig 5. A statistical analysis of the load on each bus would be interesting to determine how to model the probability distribution of each load more properly, but it is left here as a suggestion for future studies.

Network topology also plays an important role in the amount of voltage stability of a system. In order to cover several possible scenarios, a contingency list containing the most common/harmful contingencies is elaborated. PV curves are calculated considering the contingency list and all the load increase scenarios.

Since the computational effort to perform all the above mentioned calculations is cumbersome, commercial grade software was required to perform such task. In this project, we have automated PSS/E[®] using the python language to cover a large amount of scenarios. Python is a powerful interpreted, object-oriented computer language that can be used to automate PSS/E[®]. The Python interpreter is embedded in PSS/E and several functions are already built-in PSS/E[®].

A python script was developed to run all the PV curves for all the different contingencies and load increase directions and collect data for the data base. It makes the data output from PSS/E more flexible since any variable can be used as output, allowing the user to select the ones that he wants to have available. This automation has two main advantages: it speeds up the computational process and enables users to collect any desired data from any converged power flow solution along the PV curves. Another good thing about the automation process is that any system variable can be pulled out during system simulation, either for steady state or dynamic simulations.

▪ *Contingency Ranking for MLRM Development*

In order to classify the severity of each contingency with respect to VSM, a performance index (PI) was utilized for contingency ranking purposes [24].

$$PI_i = \frac{\lambda_{bc} - \lambda_i}{\lambda_{bc}} \quad (2.2)$$

Where:

- λ_{bc} : Voltage stability margin of base case
- λ_i : Voltage stability margin of contingency i

A PV curve is run for each contingency and each load increase direction. Bus voltage magnitudes/angles and reactive power reserves are sampled on each run and a PI_i is calculated for each contingency. Based on the PI value, the data collected from each contingency will be placed in one of the data base files used to design the MLRM for that specific PI range. The data is divided following the methodology described in Table I. The higher the PI value is, the more severe the contingency is. Therefore, MLRM 1 models the effects of the least harmful contingencies whereas MLRM 10 models the effects of the most severe ones.

Since the MLRM are created from data collected based on contingency severity, it is important to have contingencies with PIs ranging from 0 to 1, i.e., contingencies with a varied range of impact. By doing so, there will be data available to generate all the necessary MLRM.

Table I: MLRM Definition

<i>Model Number</i>	<i>PI</i>	<i>Model Number</i>	<i>PI</i>
<i>MLRM 1</i>	0.1-0.0	<i>MLRM 6</i>	0.5-0.6
<i>MLRM 2</i>	0.1-0.2	<i>MLRM 7</i>	0.6-0.7
<i>MLRM 3</i>	0.2-0.3	<i>MLRM 8</i>	0.7-0.8
<i>MLRM 4</i>	0.3-0.4	<i>MLRM 9</i>	0.8-0.9
<i>MLRM 5</i>	0.4-0.5	<i>MLRM 10</i>	0.9-1.0

Once all the data gathered from system simulation is properly separated accordingly to the PI index of each MLRM, the design process of those models can start.

Since each MLRM has its range of prediction, an ANN will then be trained to select the proper MLRM at each instant. To train the ANN a target was assigned to the its output. The target represents each model and its value represents the exact middle point of each MLRM PI range. This subject will be discussed in detail in section 3.

3. Theoretical Background

This section presents all the theoretical background and tools utilized on the development of the project.

3.1. Multi-Linear Regression Models (MLRM)

Multi-linear regression models are among the most popular statistical models used for statistical inference. They relate two groups of variables named the dependent variable, represented by the y variable, and the independent variables, represented by the x variables. In this work, the independent variables x_s represent reactive power reserves (RPRs) and the dependent variable y represents the amount of voltage stability margin (VSM) in the system. The multi-linear regression model can be represented as follows:

$$y_i = \beta_0 + \beta_1 x_{1i} + \beta_2 x_{2i} + \dots + \beta_p x_{pi} + \varepsilon \quad i=1, 2 \dots n \quad (3.1)$$

This is the classical formulation of a multi-linear regression model for the i^{th} observation. In some cases, a more complex structure can be added to the model if polynomial terms and combined terms. A second order polynomial model on the regressors can still be treated as a multi-linear regression on the regression coefficients β_i 's, and thus can still be solved using the method of least square.

A second order multi-linear regression model can be defined as follows [28]-[30]:

$$y = \beta_0 + \beta_1 x_1 + \beta_2 x_2 + \beta_3 x_1 x_2 + \beta_4 x_1^2 + \beta_5 x_2^2 \dots + \beta_{n-1} x_n + \beta_n x_n^2 + \varepsilon \quad (3.2)$$

In case we have several observations available, equation (2) can be put in the vector/matrix form as represented below:

$$\mathbf{y} = \mathbf{X}\boldsymbol{\beta} + \boldsymbol{\varepsilon} \quad (3.3)$$

In the above equation, \mathbf{y} is a vector of VSM observations and \mathbf{X} is a matrix of monitored RPR. The objective is to find a vector of coefficients β_i s that minimizes the error ε . Thus the search for the best β_i s can be state as an optimization problem as follows:

$$\underset{\boldsymbol{\beta}}{\text{Min}} \|\boldsymbol{\varepsilon}\|^2 = \underset{\boldsymbol{\beta}}{\text{Min}} \|\mathbf{y} - \mathbf{X}\boldsymbol{\beta}\|^2 \quad (3.4)$$

The optimum solution of equation (3.4) is defined as the least square solution and is described in appendix 1. The result of the above optimization problem is given as:

$$\hat{\boldsymbol{\beta}} = (\mathbf{X}^T \mathbf{X})^{-1} (\mathbf{X}^T \mathbf{y})^T \quad (3.5)$$

The MLRM regression model is then described by:

$$\hat{\mathbf{y}} = \mathbf{X} \hat{\boldsymbol{\beta}} \quad (3.6)$$

The residual $\boldsymbol{\varepsilon}$ represents the difference between the correct value of VSM and the actual value.

$$\boldsymbol{\varepsilon} = \mathbf{y} - \hat{\mathbf{y}} \quad (3.7)$$

Once the regression coefficients are obtained ($\boldsymbol{\beta}$ vector), an instant estimation of VSM ($\hat{\mathbf{y}}$) can be obtained by multiplying the RPRs (\mathbf{X} vector) by the regression coefficients. Throughout the paper, the variables with a superscripted hat ($\hat{}$) denote estimated value of the variable.

Once the multi-linear regression model is obtained, statistical tests are required to assess the adequacy of the model. Model adequacy checking using residual analysis is a traditional method to identify violations of basic regression assumptions. Therefore, it is advisable to perform model adequacy checking on obtained MLRM before they are used in practice [29].

According to [29]-[30], some of the most important characteristics that a MLRM must hold are the following:

- I. y is a random variable with a certain probability distribution for any combination of X_i s variables.
- II. The y observations are statistically independent from one another.
- III. The mean value of y at each specific combination of combination of X_i s is a linear function of X_i s.
- IV. The variance of $\boldsymbol{\varepsilon}$ has constant variance for any value of y (homoskedasticity).
- V. For any fixed combination of X_i s, the $\boldsymbol{\varepsilon}$ follows a normal distribution with mean zero and variance equals to σ^2 .

The first three assumptions are reasonably easier to be obtained whereas assumptions IV and V are the ones whose violation causes serious inadequacies to model validity.

Assumption V is not mandatory but it is usually required for general inference making. If the assumption of normality is not severely violated (assumption V), the conclusions reached by using the model are generally reliable and accurate. In other words, the F hypothesis tests to check if the model coefficients properly represent the model is more robust if the normality assumptions are hold, therefore validating the model [28].

In case the residual ε fails to follow a normal distribution, variable transformation applied on the y variable are employed so that the residuals of the transformed variable y' , denoted by ε' , have a normal probability distribution. Several kinds of transformations can be utilized such as $\log(y)$, power (y) and so on. Box-Cox is a popular procedure to improve normality of the residual (ε) distribution. It selects the best exponent for a power transformation of the type $y^{\hat{\alpha}}$ on the dependent variable y , where α is a number usually varying from -2 to 2.

After the Box-Cox procedure is applied, popular normally checking test can be used to verify normality of data distribution. Shapiro-Wilk/Francia test and Kolmogorov-Smirnov are among the most popular test [29]-[30]. Although useful, normality test failure does not directly imply that the normal distribution assumption cannot be made. Even if the data fails the normality test, normality can be assumed in case the residual histogram follows has a normal curve with well behaved distribution tails. More details regarding normality issues will be given in section 4.

▪ *Model adequacy checking through hypothesis test*

After the MLRMI is developed, a hypothesis test for significance of overall regression can be done to accept or reject the MLRM. The test is described in the following manner:

H_0 : All independent variables (x_i) considered do not explain a significant amount of the variation in y . In other words, $\beta_1 = \beta_2 = \dots = \beta_p = 0$.

H_a : The model is well explained by the obtained variables (x_i). In other words, not all β_i 's are equal to zero.

The F statistics is defined as:

$$F = \frac{MSR}{MSE} \quad (3.8)$$

MSR, MSE and other statistical variables are defined in the appendix1. After calculating the F statistics, its value is compared with the critical point of the F-distribution $F_{k,n-k-1,1-\alpha}$, where α is the preselected significance level, k is the number of regressors and n is the total number of samples used. If the calculated value for the F statistics exceeds the critical point, then the null hypothesis (H_0) is rejected:

$$\text{If } F = \frac{MSR}{MSE} > F_{k,n-k-1,1-\alpha}, \quad \square \text{ reject } H_0 \quad (3.9)$$

▪ *Multicollinearity*

If two or more independent variables in the model present some sort of linearly dependence, the matrix $(\mathbf{X}^T \mathbf{X})$ cannot be inverted and the regression coefficients cannot be obtained from (3.5). If close to linear dependence occurs, the matrix $(\mathbf{X}^T \mathbf{X})$ becomes

ill-conditioned and may present some anomalies such as a high variance of the estimated regression coefficients $\hat{\beta}_i$ s.

To correct for such problem, variables that exhibit closeness to linear dependence were eliminated in our approach. In order to verify if two variables are close to linear dependence, the aperture angle between them was calculated. If that angle θ is smaller than minimum threshold θ_{min} , then the variables are considered linearly dependent and one of them must be eliminated from matrix \mathbf{X} [29]-[30]. Fig 8 gives an idea of the approach:

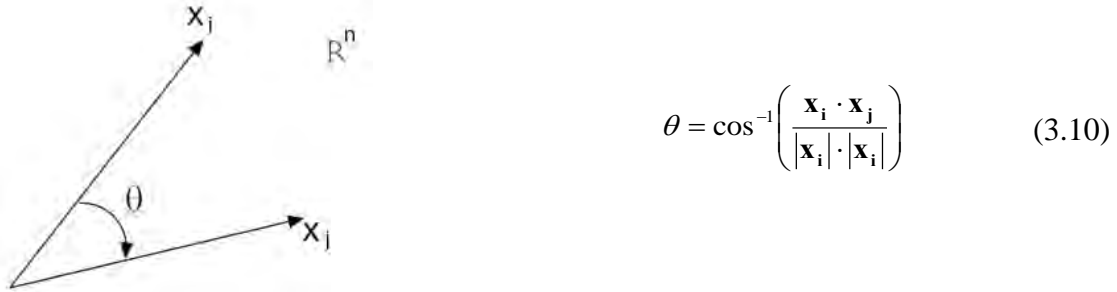


Fig 8: Linear dependence checking

▪ *Heteroskedasticity*

Another problem that may be encountered in the MLRM is the violation of assumption IV. If the variance of the residual vector ε does not hold a constant value for all the y range ($Var(\varepsilon) = \sigma^2 \mathbf{I}$), then heteroskedasticity is said to occur.

This problem is frequently encountered in the statistical literature. There are several techniques to address it with the y variable transformation being one of the most popular ones. Although there are tests employed to identify heteroskedasticity, they will not be used for it goes beyond the scope of this text. Visual inspection of the residual plots is usually sufficient to identify homoskedasticity violations [28]-[32].

▪ *Conceptual flowchart for multi-linear regression*

The following flowchart describes the required steps for MLRMs development. Initially, a wide range of operating scenarios and an extensive list of contingencies must be created. After that, offline PV curve calculations are run in order to obtain RPRs, VSMs and PMU data to create the data base. Once all data is collected and stored in a data base, the MLRM development starts.

After the optimal coefficients of the MLRM are calculated, the validation process is used to identify major violations on the regression assumptions. If no violations of the assumptions are found, then the MLRMs are ready to be used in online voltage stability margin monitoring, otherwise model correction and MLRM redesign must be necessary.

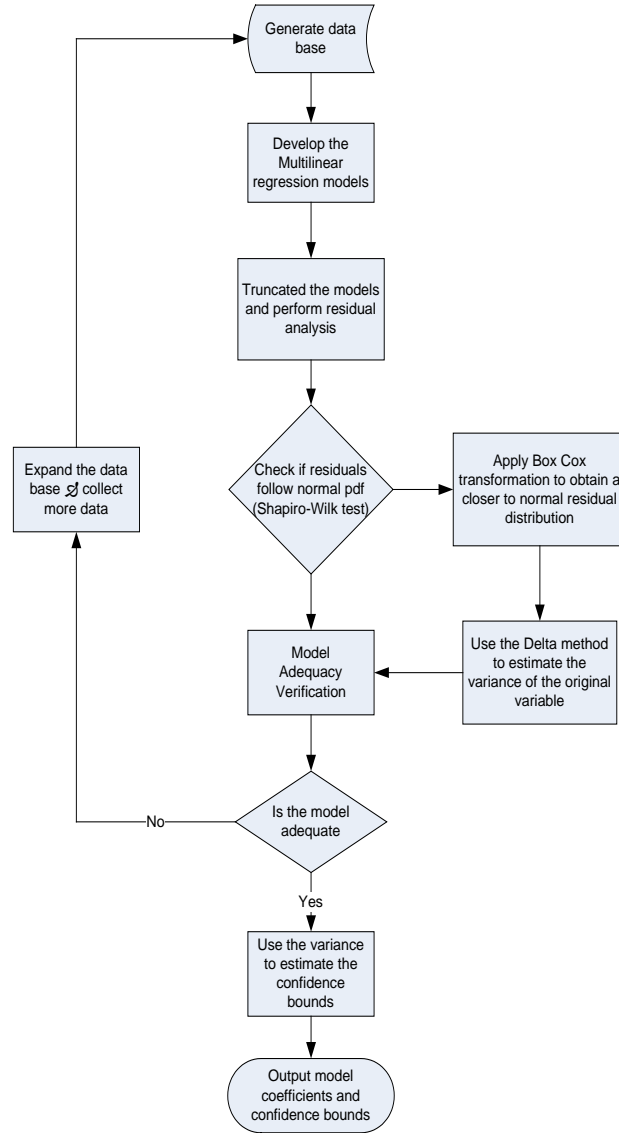


Fig 9: Flowchart describing the whole methodology

If either the normality or the homoskedasticity assumptions are violated, Box Cox transformation is first tried in order to eliminate the violations. If it cannot satisfactorily resolve the problem, then more data needs to be obtained and the more simulations are required.

3.2. Artificial Neural Networks (ANN)

Artificial neural network has its origins on the search for a mathematical description of information processing in biological systems. The focus of this chapter is present neural networks that are efficient models for pattern recognition. After an analysis of the different types of ANNs designed along the years, we shall focus our attention on the one that has proven greatest practical value: the multilayer perceptron neural network [35]. A functional form of the neural network model will be presented along with the

parameterization of the basis functions. Later, it will be shown how the search for the best parameters of the network involves the solution of a nonlinear optimization problem.

A neural network model is described in Fig 10. Three main layers compose a typical ANN: the input layer, the hidden layer (also called intermediate layer) and the output layer. Except for the input and output layers, an ANN can have as many hidden layers as necessary. Each layer has a certain number of neurons. Each neuron is composed of nodes (biologically equivalent to dendrites and represented in Fig 10 as the circles) and connection links (biologically equivalent to axons and represented in Fig 10 as the lines).

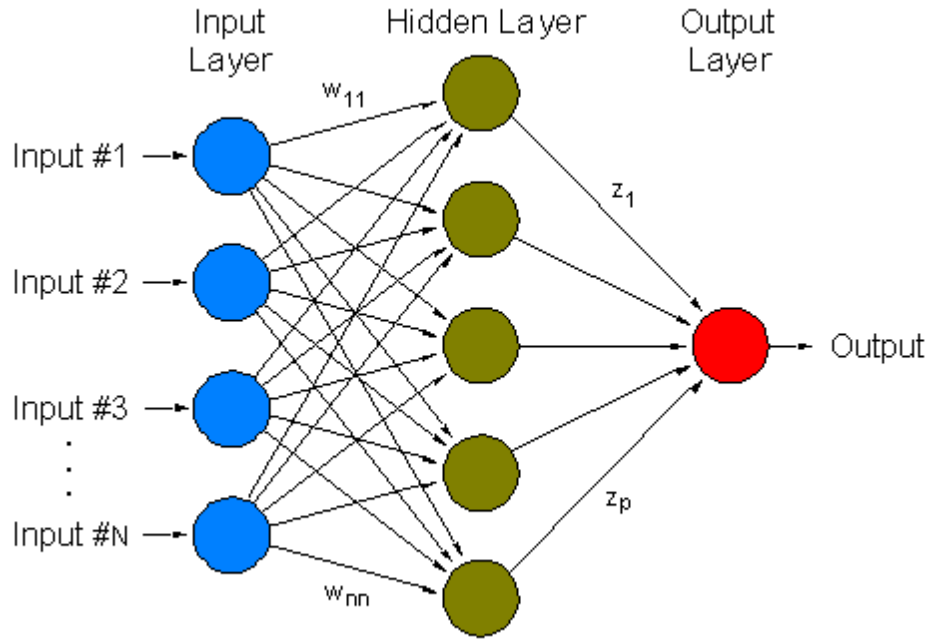


Fig 10: Artificial neural network structure

Data are supplied to input nodes and output node and an adjustment of the weighting factors is performed in order to minimize the error between the real output value (y) and the estimated output value (\hat{y}). A more mathematical representation of the ANN of utilized in this work is give in Fig 11.

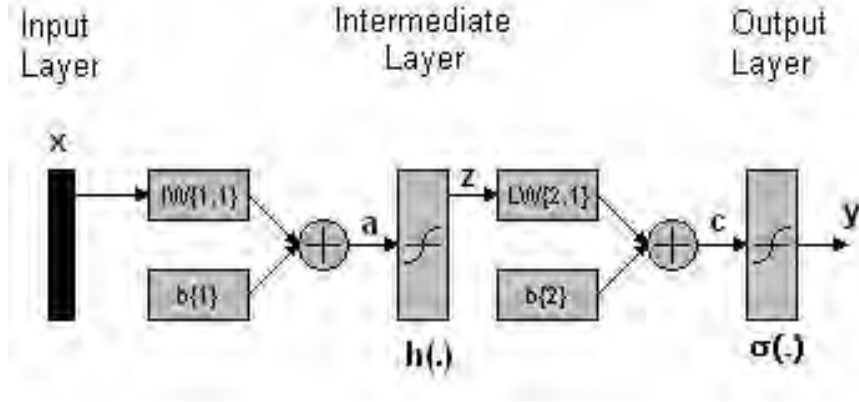


Fig 11: ANN parameter representation

The data processing on an ANN follows the following pattern: Data presented at the input layer and multiplied by a weighting factor vector w_{ji} and summed up with a bias factor b_i as described in the equation (3.11).

$$a_j = \sum_{i=1}^D w_{ji}^{(1)} x_i + b_i^1 \quad (3.11)$$

The quantities a_j are known as *activations*. Once the vector \mathbf{a} is obtained, it will be transformed using a nonlinear activation function $h(.)$. The transformation generates the \mathbf{z} vector where each element is given by equation (3.12).

$$z_j = h(a_j) \quad (3.12)$$

Many functions can be used to represent $h(.)$ and the tangent sigmoid function was the one selected for presenting the best performance in this case. The tangent sigmoid function is defined as:

$$h(a_j) = \frac{2}{1 + e^{-2a_j}} - 1 \quad (3.13)$$

After having calculated the vector \mathbf{z} , the variables go through another weighted summation to generate the vector \mathbf{c} as can be seen in Fig 11 and eq. (3.14).

$$c_k = \sum_{j=1}^M w_{kj}^{(2)} z_j + b_j^2 \quad (3.14)$$

Finally, the output vector y is generated by transforming vector \mathbf{c} using another sigmoid function $\sigma(.)$ as described below.

$$y_k = \sigma(c_k) \quad (3.15)$$

The final formulation representing the MLP ANN model is given as:

$$y_k(x, w) = \sigma \left(\sum_{j=1}^M w_{kj}^{(2)} h \left(\sum_{i=1}^D w_{ji}^{(1)} x_i + w_{j0}^{(1)} \right) + w_{k0}^{(2)} \right) \quad (3.16)$$

After describing how the ANN works, the application of ANN for MLRM is given on the sequence:

- *MLRM selection from ANN*

As mentioned before, more than one MLRM was created in order to cover all the possible scenarios and contingencies. Therefore a MLRM needs to be selected at each moment to estimate VSM. The ANN will be trained by supplying the PMU data (bus voltage angles and magnitudes) to its inputs and the respective MLRM PI target to its output. The idea is to have the ANN producing the MLRM assigned PI target by processing real-time PMU data. In that way the MLRM selection is done automatically, reducing thus the burden on system operators. Before we go into details of how the ANN works as MLRM selector, we will briefly remember how the data base for each MLRM model is organized.

Each contingency will be assigned a level of severity based on its performance index (PI). Since the PI varies from 0 p.u (non severe contingency), to 1 p.u (severe contingency), we decided to divide the severity ranges in 10 equally spaced intervals of width 0.1 p.u. Contingencies whose PI fall into the same interval are grouped together and are assigned the same PI target as shown in table II.

In our approach, bus voltage magnitudes and angles will be used as inputs to the ANN, whereas a target representing each MLRM will be assigned to the output of the ANN.

Table II: Contingency grouping methodology

<i>Model</i>	<i>PI value</i>	<i>Assigned PI target</i>	<i>Level of severity</i>
<i>MLRM 1</i>	1.0-0.9	0.95	Highest
<i>MLRM 2</i>	0.9-0.8	0.85	
<i>MLRM 3</i>	0.8-0.7	0.75	
<i>MLRM 4</i>	0.7-0.6	0.65	
<i>MLRM 5</i>	0.6-0.5	0.55	
<i>MLRM 6</i>	0.5-0.4	0.45	
<i>MLRM 7</i>	0.4-0.3	0.35	
<i>MLRM 8</i>	0.3-0.2	0.25	
<i>MLRM 9</i>	0.2-0.1	0.15	Lowest
<i>MLRM 10</i>	0.1-0.0	0.05	

Once each data base for every MLRM is created, then the ANN training process can start. Next section will present some data pre-processing techniques utilized in order to adequate the data.

3.3. Data Pre-Processing and Feature Extraction

Almost all applications of ANN require the data to be transformed before it can be used as input to the network. Two main objectives are sought while performing such pre-processing task:

- One is to reduce the number of inputs to the ANN and consequently to reduce its complexity. It has been observed that the performance of an ANN can be improved up to a certain number of inputs. After an optimal value, too many inputs start to rather reduce the performance of the ANN as they start to “compete” against each other, therefore reducing the recognition capabilities of the network. [34]-[35].
- The second reason is that sometimes the input data does not have the same order of magnitude. This difference in order of magnitude may penalize some variables in detriment of others. To overcome this problem, a standardization process is used. This standardization consists basically of transforming the input variables by subtracting each input value from its mean and dividing it by its standard deviation. Such process should reduce the size disparity among the variables and cope to a better model performance. Other data anomalies such as missing values or incorrect target values can also appear in the data and must also be properly treated.

One of the most important pre-processing techniques involves the reduction of the dimension of the input vector. The proper selection of the variables that will form the

input vector must be carefully done in order to avoid rejecting variables with salient explanatory capability. Also, a smaller input vector will require a smaller network structure which means that a smaller set of network parameters will have to be determined. Therefore, by reducing the number of ANN inputs one can get an ANN that is faster to train and has better generalization properties.

Another particular point in the application of ANN to power systems using PMU measurements is the fact that PMUs are installed in specific locations across the system. Therefore, the development of an ANN that will take PMU measurements as inputs may have some restrictions the number of measurements and where they should be taken.

In order to evaluate how much PMU devices across an area we adopted two different approaches in this work. In the first approach, a high penetration of PMUs devices distributed all across the system is considered. In the second approach, the most specific locations for future PMUs installation were sought to try to reduce the number of required PMU measurements. Some precaution should be taken when considering possible sites for PMU installation based on feature extraction for ANN. Since a predefined number of scenarios are selected to generate the data base, the variables that show significant importance may be restricted to the scenarios considered in the specific data base only, and may not have the same importance for scenarios that were not implemented.

Feature or input selection has been recognized as an important problem in the context of regression models [31]. Feature or input selection bias may adversely affect the prediction ability of the model. This is because the models may “overfit” the data in the presence of selection bias and it may not hold good generalization properties. In this project, we will have to select amongst the most appropriate RPR to be used as inputs to the MLRM and the most meaningful PMU data as inputs to the ANN. Thus, feature selection is an important issue and needs to be properly addressed in this work.

3.4. Data Flow Along ANN and MLRM

Fig 12 pictorially shows how the online measured data would flow across the ANN and the MLRMs. After the ANN is designed, the bus voltage phasor measurements are passed along to the ANN. The ANN identifies the current system condition and produces an index on its output representing the MLRM to be used.

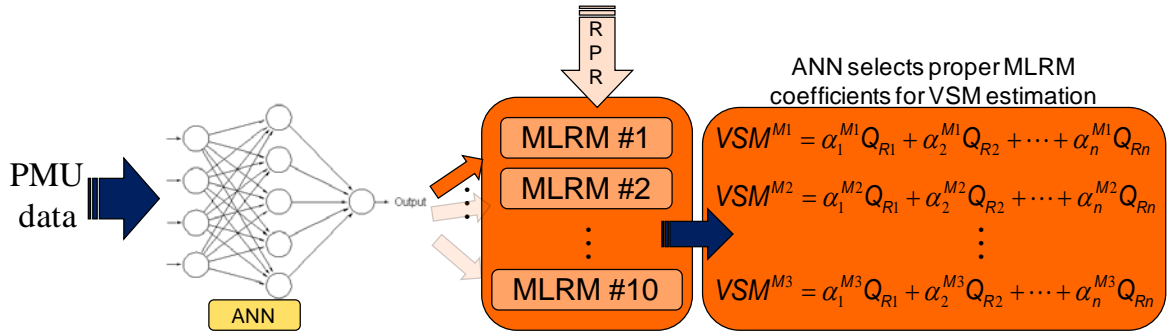


Fig 12: Data flow across ANN and MLRM

Once the proper MLRM is identified, RPRs are provided as inputs to the MLRM which will in turn produce the estimation of VSM based on the amount of RPR available at the selected machines. After showing how the information flows in order to obtain the VSM estimation, a block diagram representation with all the necessary steps involved in online VSM margin estimation is given in the sequence

3.5. Online Implementation of the Methodology

The following diagram in Fig 13 summarizes all the steps involved in the development of the methodology.

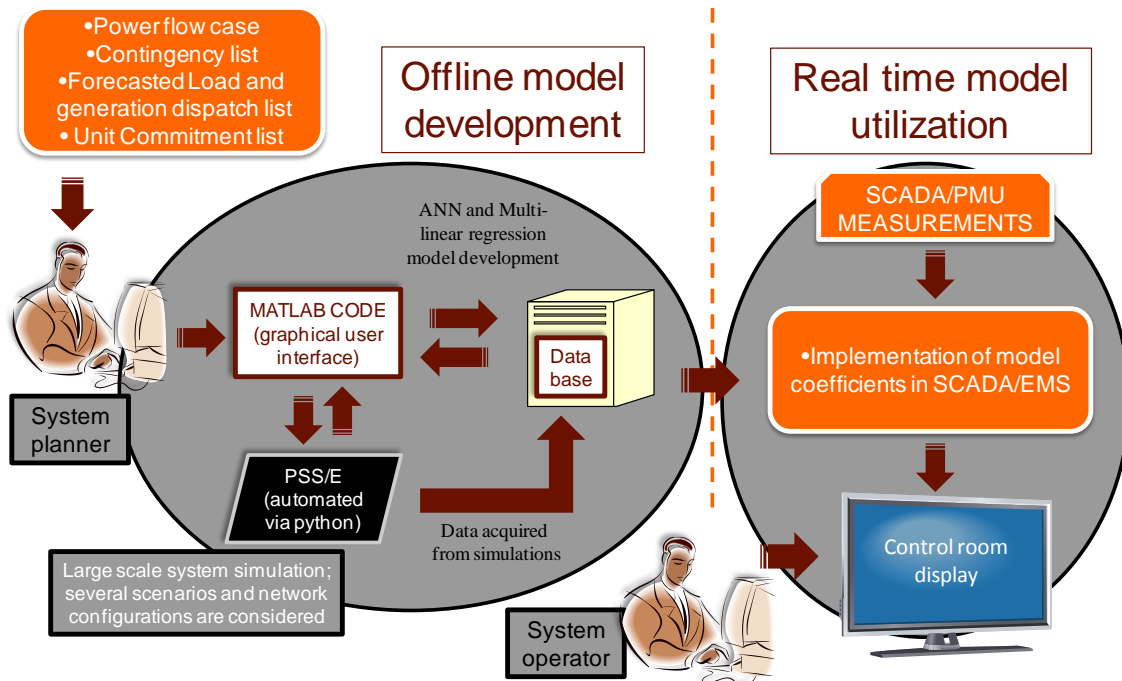


Fig 13: Off/Online overall methodology

Initially, all the power flow cases, a list of critical contingencies, forecasted load levels and generator dispatch order are obtained for system simulation. Several PV curves are calculated for all the contingencies and many load increase directions in order to account for load growth uncertainty in real-time operations. In this case we automated PSS/E® via python in order to speed up system simulation. Once all the simulations are run and the data base is created, data preprocessing is carried over on the data in order to prepare it for MLRM and ANN design. Data preprocessing was performed utilizing Microsoft Excel® through visual basic scripts. The reason why the data was manipulated in Excel is because if a visual inspection of the data is necessary, it would be easier to do so in Excel than in a text file due to all the resources available for data manipulation.

Once the data is preprocessed, Matlab[®] scripts will be utilized to design the MLRM and the ANN. Matlab has a well established and stable statistical and neural network toolbox, which makes the development of the MLRMs and the ANN very practical and versatile. The MLRMs are trained using RPRs and VSMs obtained along the PV curve calculations. The ANN is trained using an index that represents each MLRM and voltage phasors (PMU measurements) from buses across the system.

After the MLRMs and the ANN are designed and validated, they are made available to the EMS/SCADA system. They can be either written into the EMS/SCADA or data from EMS/SCADA can be pulled out to a standalone PC to be used on the MLRMs and ANN. The estimation of VSM should be made available to operators on the control room display.

4. Studied Cases and Discussion

Two different test systems were used to test and demonstrate the methodology presented in this work. A small system was initially used in order to apply the methodology and then a real size test system was later used to demonstrate that the methodology can be applied to realistic systems with good performance.

4.1. IEEE 30 – Bus Test Case

Initial tests of the methodology were conducted on the IEEE 30 bus test system. A description of IEEE-30 bus test system is given in table III.

Table III: Power System Description

<i>Number of buses</i>	<i>Number of generators</i>	<i>Number of loads</i>	<i>Number of lines</i>	<i>Number of transformers</i>
30	6	22	35	6

For this small system, all loads were assumed to participate in the load increase process and all the necessary amount of generation was proportionally divided among the machines in the system, except the slack bus. Each machine picked up a share of the total increased load. The share was proportional to the individual generation of each unit in the total generation.

All the desired simulation data was collected from PSS/E[®] and stored in Excel[®] files for data preprocessing. At this stage, data will be manipulated in order to be used as input in Matlab[®] to design the MLRMs. This data preprocessing in excel uses a VBA[®] macro which objectives are:

- To eliminate unnecessary informative (non numeric) data in the PSS/E[®] output file.
- Separate the contingencies by margin and group the ones with similar VSM.
- Reduce the amount of data exported to Matlab[®] for MLRM development.

Once preprocessed, the data it is used by Matlab[®] for the development of the MLRMs. Due to space constraints, the design and analysis of only one MLRM out of the 10 that were created is going to be shown. The analysis of the other MLRM can be performed in a similar manner.

A total of 50 contingencies were considered in this example. Contingencies included all N-1 cases and several other multiple contingencies where more than one device was out of service at the same time, including loss of units and transformers.

A central load increase direction was defined and PV curves were calculated for all the 50 contingencies in the list. Other nine load increase scenarios were created as random perturbations around the central load increase scenario, totalizing ten load

increase scenarios used in the training phase. Such random perturbation followed a normal distribution as shown in Fig 17. As mentioned before, only MLRM 1 will be analyzed from the statistical point of view. The analysis of other MLRMs can be easily extended and will not be presented here for the sake of space.

MLRM is developed and the β coefficients are found. Quadratic and crossed terms were added to the multi-linear regression model to improve accuracy. The residual distribution for MLRM 1 for the IEEE 30 bus test system is presented in Fig 14.

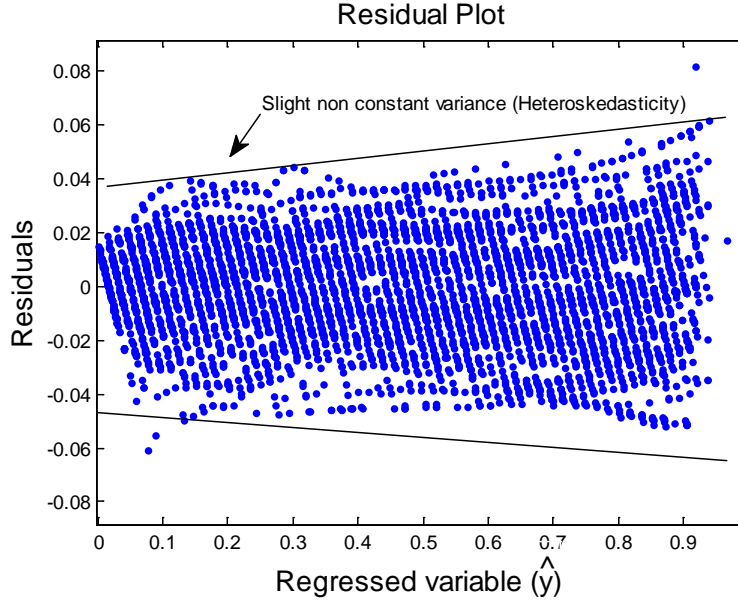


Fig 14: Residual distribution

The residuals distribution presents a close to random distribution around the mean value zero. The variance shows a slight variation along the regressed values of \hat{y} , as can be seen in Fig 15. The conic shape of the residuals indicates the presence of non constant variance, which is also known as heteroskedasticity. Since the constant variance violation is not significant, no action will be taken to correct the model in this case. If there is a severe violation of the homoskedasticity condition, then appropriate actions must be taken as described in section III. In this research we have faced situations where Box-Cox transformations were needed in order to bring the residual probability distribution function close to normal. An example of such transformation will be given on the next test case where the residual distribution shows skewness and heteroskedasticity.

The residual histogram on Fig 15 can be used to verify if the normality assumption is significantly violated or not. The residual distribution follows a close to normal distribution with well behaved tails. In case a significant discrepancy is observed on the histogram plot, variable transformations can be used to make the residuals to follow a normal probability distribution function.

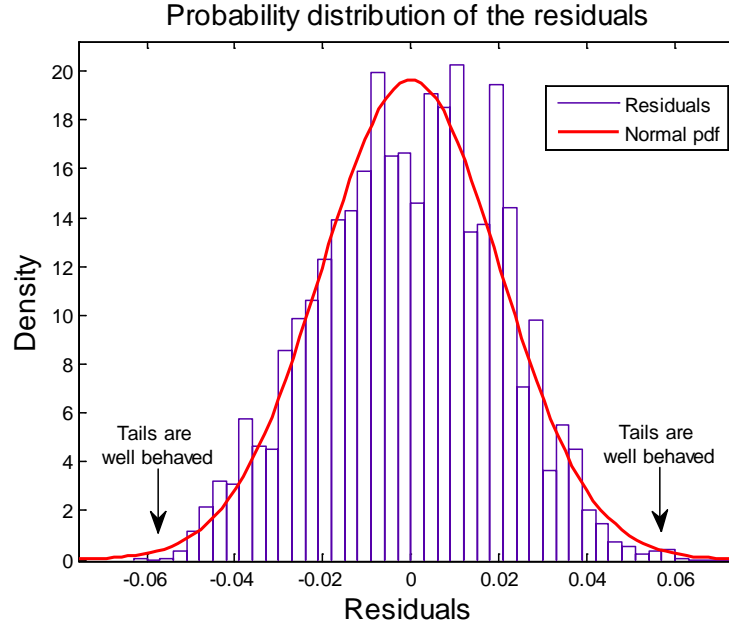


Fig 15: Residual histogram

The parameters of the above normal probability distribution fit for the residual presented in Fig 15 has its coefficients given in table IV.

Table IV: Distribution Parameters

<i>Parameter</i>	<i>Estimate</i>	<i>Standard Error</i>
<i>Mean (μ)</i>	3.16×10^{-16}	0.000287
<i>Standard Deviation (σ)</i>	0.041318	0.000203

The ANOVA table containing general information about the multi-linear regression model is presented in table V. As can be seen from the ANOVA table, the regressed model has a R-squared value close to 1. The R-square value is used to measure the goodness of fit of a model. An R-squared value of 1 signifies that the regressed line perfectly fits the data points.

Another important value from the ANOVA table is the F-statistic, which will be utilized in the F-test to verify the appropriateness of the model.

Table V: ANOVA table

<i>Source</i>	<i>Sum of Squares</i>	<i>Degrees of freedom</i>	<i>Mean Square</i>	<i>F</i>	<i>R²</i>
<i>Regression</i>	2.06	4979	4.14×10^{-4}	4.19×10^4	0.9967
<i>Residual</i>	347.52	20	17.38		
<i>Total</i>	349.58	4999			

▪ ***F-Test***

The F-test is utilized to check whether or not the coefficients obtained by regression can properly explain the dependent variable (VSM) y using the set of X variables (RPRs). The considered significance level considered in this work was $\alpha=5\%$. Consequently, the significance level of the test is 95%. The F-test is applied as follows.

$$F = \frac{MSR}{MSE} = 4.19 \cdot 10^4 > F_{20,4979,0.95} = 1.57, \square \text{ reject } H_0 \quad (4.1)$$

It can be concluded from the hypothesis test that the null hypothesis H_0 must be rejected in detriment to hypothesis H_a (see section 3.1). Therefore it is assumed that there is a regression relation between the dependent variable y and the set of X variables. Once assumed that there is a linear relationship between the response variable y and the set of X variables, the estimated VSM is plotted against the actual VSM in fig 16.

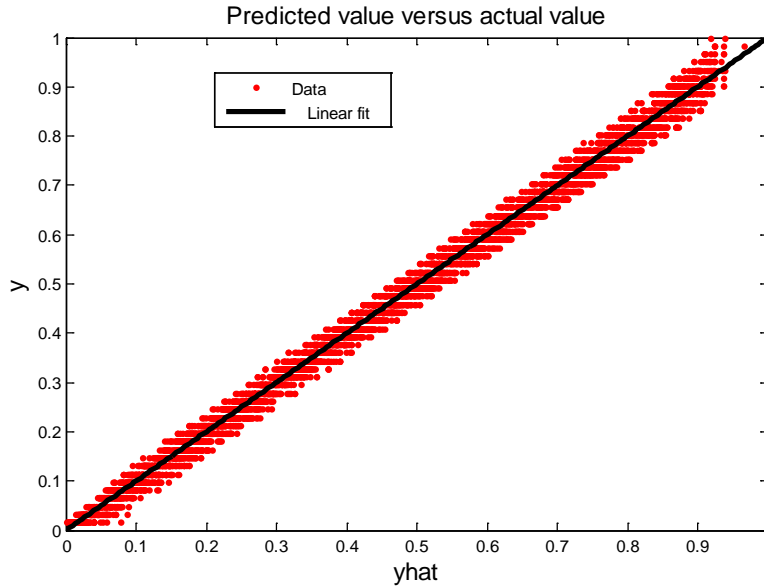


Fig 16: Regressed VSM versus actual VSM

As can be seen from the picture, an exact VSM estimation would not present any data spread around the regression line. But since the regression model is not exact, and it is important that it does not have such characteristic for generalization purposes, some data can be seen spread around the line. The data distribution is homogeneous and presents a constant variance (same spreading width), which in fact confirms the fact that the heteroskedasticity present in the residuals is not significant.

▪ *Confidence bounds*

The following table VI shows the confidence intervals for residuals of each MLRM obtained. Two standard deviations around the mean values were considered. The $\pm 2\sigma$ standard deviation confidence bound accounts for 95.44% of the data. It means that 95.44% of the residuals should fall within the confidence bound specified by $\pm 2\sigma$. The reason why M9 and M10 were not designed was because there were no contingencies to generate data for those models, since they take into account very severe contingencies with very low VSM.

Table VI: Confidence Intervals

<i>Model</i>	<i>Standard deviation</i>	<i>Percentage of estimated error within $\pm 2\sigma$ (95.44% of the estimations)</i>
<i>MLRM 1</i>	4.13	± 8.26
<i>MLRM 2</i>	5.87	± 11.75
<i>MLRM 3</i>	4.47	± 8.95
<i>MLRM 4</i>	6.72	± 13.45
<i>MLRM 5</i>	4.98	± 9.97
<i>MLRM 6</i>	2.10	± 4.21
<i>MLRM 7</i>	2.59	± 5.18
<i>MLRM 8</i>	4.47	± 8.95
<i>MLRM 9</i>	No data	No data
<i>MLRM 10</i>	No data	No data

As mentioned before, the confidence bound of a normally distributed random variable tells us how many times the variable will assume values within the confidence bound. Fig 17 shows the confidence bounds for different values of standard deviation. It can be seen that around 68.2% of the observations fall within $\pm\sigma$ from the mean, 94.4% fall within $\pm 2\sigma$ and so on.

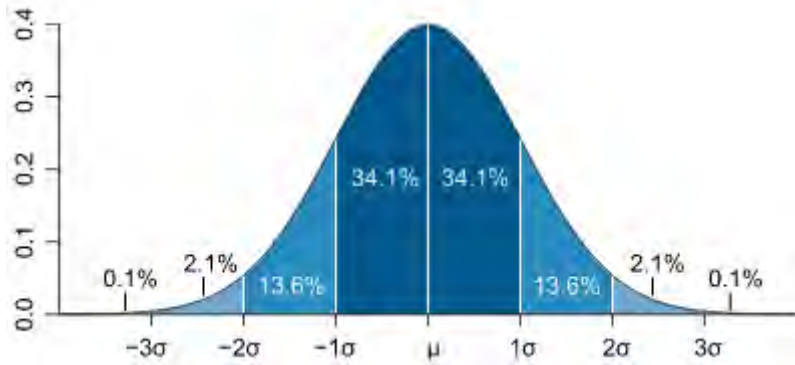


Fig 17: Confidence bounds of a normally distributed random variable [40].

After the MLRM coefficients were obtained, a test was performed on them to verify their accuracy in estimating VSM. Table VII shows some random selected system operating conditions at where the MLRMs were tested. The testing scenarios represent a different load increase direction from the ones used for training

Table VII: MLRMs testing

<i>Model</i>	<i>Actual VSM</i>	<i>Estimated VSM</i>	<i>Error %</i>
<i>MLRM 1</i>	330	312.4297698	-5.32
<i>MLRM 2</i>	230	212.7649831	-7.49
<i>MLRM 3</i>	300	305.4952326	1.83
<i>MLRM 4</i>	340	309.4852367	-8.97
<i>MLRM 5</i>	170	193.5296532	13.84
<i>MLRM 6</i>	180	175.3668083	-2.57
<i>MLRM 7</i>	90	90.0286974	2.86
<i>MLRM 8</i>	80	79.07101965	-1.16
<i>MLRM 9</i>	No data	No data	No data
<i>MLRM 10</i>	No data	No data	No data

**** The negative value in error estimation means underestimation of the VSM; positive values represent overestimation of VSM.**

The results presented in table VII shows that the estimation error is in accordance with the values estimated in table VI. Although most of the errors fall within the $\pm 2\sigma$ range, MLRM 5 has an estimation error out of the $\pm 2\sigma$ confidence bound. The confidence bound only tells us how much data is expected to be found within its

boundaries. Error values out of the confidence bounds can still occur with a low probability.

- *ANN training for MLRM selection*

Once all MLRM models are designed, the focus shifts towards the design of the ANN, which will be responsible for the selection of the MLRMs in real-time. Several approaches were considered during the ANN development.

Initially, PMU units were considered to be installed in all the buses in the system, totalizing 30 PMUs. Then principal component analysis (PCA) was used to identify what measurements were providing a high level of explanation in the data. Once the measurements with a high level of information are found, they are used as inputs to train the ANN. Since noise present in measurement is a common problem in EMS/SCADA, the ANN test has been tested on the presence of noisy inputs and without noise. The noise considered during training had a Gaussian distribution with zero mean and standard deviation of 10% of the maximum measurement in the sample. The noise considered during testing had the same characteristic of the above mentioned but with standard deviation of 5%, 10% and 15%.

Another common problem that is regularly encountered on the control center is when there is missing data. In order to analyze the performance of the ANN for missing data, one of the PMU measurements was blocked and the recognition of the ANN was tested.

Table VIII: ANN testing

<i>Number of PMUs installed</i>	<i>Configuration</i>	<i>Testing error – No Noise</i>	<i>Testing error – Noise 1</i>	<i>Testing error – Noise 2</i>	<i>Testing error – Noise 3</i>	<i>Missing PMU data</i>
<i>PMU installed in all 30-buses</i>	<i>Regular training (no noise)</i>	95.82%	94.74%	92.99%	88.92%	93.51%
	<i>After training with noise</i>	93.72%	93.35%	92.91%	90.96%	93.44%
<i>PMU installed in 13 buses (after PCA)</i>	<i>Regular training (no noise)</i>	97.82%	93.59%	91.12%	88.29%	80.84%
	<i>Training with noise and missing PMU input</i>	98.20%	93.78%	93.35%	92.59%	89.60%

From table VIII it can be seen that the overall accuracy of the ANN is high. First we analyze the case where PMUs are considered to be installed in all the buses. It is clear that the addition of noise to the inputs reduces the accuracy of the network (line 2, columns 1-4). The addition of noise to the training data can improve the accuracy of the ANN on cases where there is noise present in the input data (line 3, columns 1-4). The loss of a PMU signal usually does not compromise the accuracy of the ANN significantly (line 2-3, column 4). For testing purposes, the PMU signal that provides most information according to PCA analysis is the one that is being considered to be missing in all the cases.

For the case where PMU locations were selected using PCA analysis, the result is the following. Again, the addition of noise to the inputs reduces the accuracy of the network (line 2, columns 1-4). The addition of noise to the training data can improve the accuracy of the ANN on cases where there is noise present in the input data (line 3, columns 1-4). The loss of a PMU signal does compromise the accuracy of the ANN significantly in this case (line 2-3, column 4). The reason is because the amount PMU measurement is already reduced. Therefore losing an extra PMU signal when there is a reduced set of measurements causes a higher impact on the recognition capability of the ANN.

4.2. PSS/E Bench[®] - Bus Test Case

The second systems used to test the methodology was the PSS/E bench[®] file, present in PSS/E version 30. The detailed information about the system is presented on table IX below.

Table IX: Power System Description

<i>Number of buses</i>	<i>Number of generators</i>	<i>Number of loads</i>	<i>Number of lines</i>	<i>Number of transformers</i>	<i>Number of Areas</i>
1648	313	1220	2602	308	25

Due to the high number of areas in the system, area 2 was randomly selected to go under a voltage stability assessment and have the online VSM monitoring methodology applied to it. Fig 18 shows a pictorial representation of the load area (area 2) and its neighboring areas (areas 1, 2, 4, 5, 8, 9 and 10).

Load will be increased in area 2 in 20 different patterns (directions) for a list of 430 contingencies until voltage collapse is reached. The contingency list includes all N-1 contingencies, including the loss of generating units and transformers. All the generation will be supplied by machines present in area 2 and machines present in all the neighboring areas surrounding area 2. Reactive reserves will be monitored in area 2 and all the areas that have common boundary with area 2, i.e., areas 1, 2, 4, 5, 8, 9 and 10.

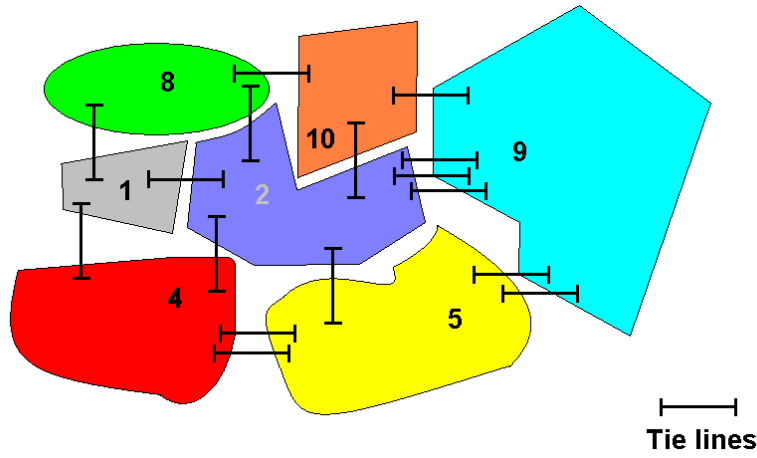


Fig 18: Area 2 and its neighboring areas

All the ten MLRM were designed for the system but only MLRM-2 had its properties analyzed. Another important fact to be mentioned is that in order to design all the MLRM for a system, the data base must contain data for each one of the MLRMs. In other words, there must be contingencies that reduce the VSM to a value with the range specified for each model or there will not be significant data available to design that specific model. Therefore, a diversified set of contingencies with different level of impact on the system is extremely desired.

As mentioned before, load was increase in area 2 in twenty different directions for all the 430 contingencies. The data base was created and al the MLRMs were designed but for sake of space, only MLRM-2 will be analyzed in this report. The RPR selected after the MLRM – 2 was designed are presented in table X.

Table X: Selected Reactive Power Reserves (RPR)

<i>Area number</i>	<i>Total number of machines</i>	<i>Selected machine</i>
1	5	-
2	5	26, 41
4	2	63
5	5	81, 84
8	7	136, 137, 161
9	26	167, 206
10	2	-

From a total of 52 monitored machines, only 11 were selected to form the MLRM – 2. Those machines are the ones that must be monitored online and have its RPR utilized as inputs to MLRM – 2.

Fig 19 shows the residual plot and fig 20 shows the histogram of the residuals for MLRM-2. As can be seen from fig 20, the normal distribution does not fit the data distribution closely and some type of correction might be advised. Although the data distribution has well behaved tails and is centered around zero, which indicates average estimated error equals to zero and absence of outliers, the symmetry around the mean values can still be improved.

One reason of such anomalies in the distribution error is because the RPR and VSM were sampled at regular load intervals while calculating the PV curves. For instance, the total load of the system was increased by 100MW during PV calculation. RPRs and VSMs are sampled at every converged power flow solution, and the process is repeated until voltage collapse happens. Since the sampling only occurs at every 100MW, the data points (RPRs and VSMs) are clustered at every 100MW as can be seen on the residual plot in fig 19.

Another issue relies on the excessive amount of data sampled close to the voltage collapse point. In order to identify the closest point of collapse, the load increment step size is reduced for precise identification of the point of collapse. This variation of the step size causes the oversampling of data points with VSM close to zero, as can also be seen in fig 19. In the previously studied system (IEEE 30), the load increase step size was kept constant and small (10MW), therefore no patterns are observed in the residual plot for the RPRs and VSM are sampled at regular load intervals, and the pdf of the residuals fits the normal curve properly as seen in Fig 15.

For a large system such as the PSS/E Bench[®], the step size of load increase must be variable or an excessive number of power flows will have to be solved, therefore slowing down the data base creation process. Hence it is almost certain that patterns in the residual plot will be observed.

If a better sampling strategy is implemented during the data base development, the chances of obtaining a residual histogram with a distribution closer to the normal probability distribution function are higher. This case was specially selected in order to provide a situation where Box-Cox transformations are applied to correct data from non normality and skewness. Also, the homoskedasticity is slightly improved after the Box-Cox transformation.

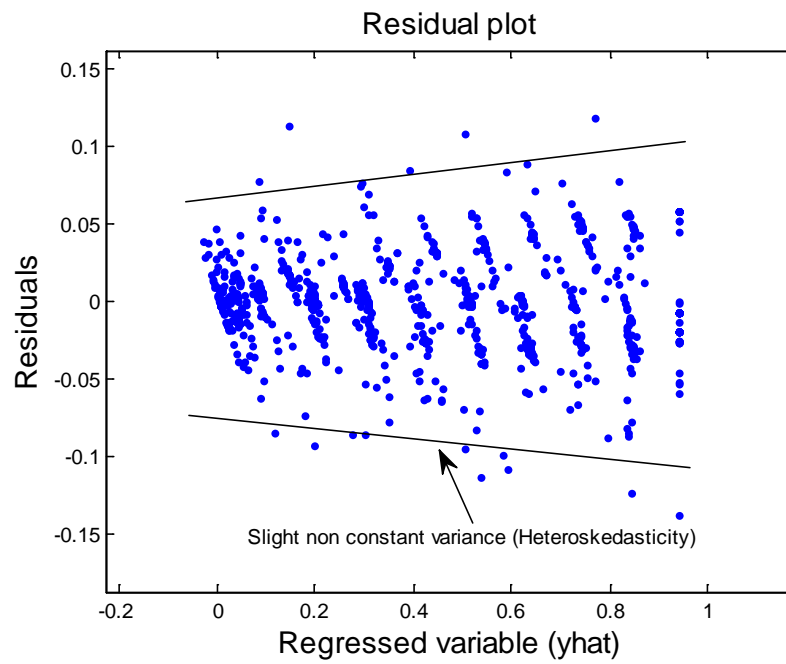


Fig 19: Residual distribution

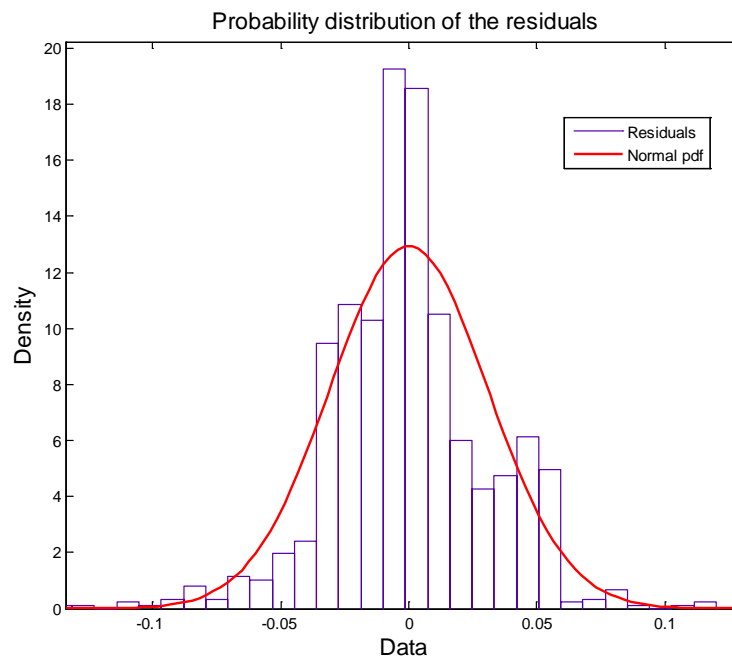


Fig 20: Residual histogram

The parameters of the normal probability distribution fit in fig 20 are presented in table XI below.

Table XI: Distribution Parameters

<i>Parameter</i>	<i>Estimate</i>	<i>Standard Error</i>
<i>Mean (μ)</i>	9.67×10^{-15}	0.000975
<i>Standard Deviation (σ)</i>	0.0374	0.000690

Fig 19 shows a residual plot for MLRM-2 together with the histogram of the distribution in Fig 20. It can be noticed from both graphs that a slight non constant variance can be observed in the residual plot, and the pdf of the residuals does not follow the normal pdf closely. Fig 21 represents the plot of the regressed variable versus the actual variable value. The more spread the points are around the line, the worse the model is.

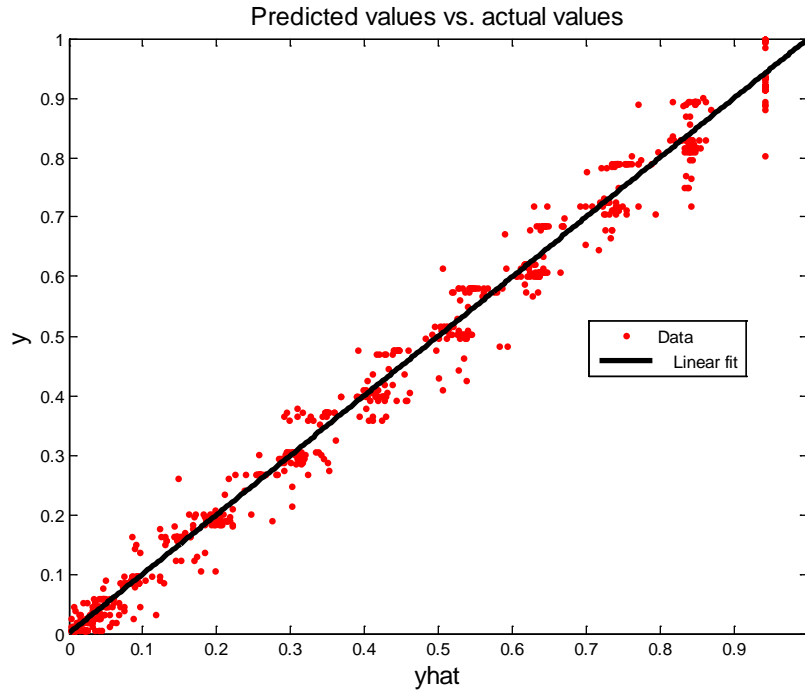


Fig 21: Regressed variable vs. actual variable

Table XII contains the ANOVA statistics for the MLRM – 2. Once again, the R-square value is relatively high, which indicates a good linear fit between RPR and VSM.

Table XII: ANOVA

<i>Source</i>	<i>Sum of Squares</i>	<i>Degrees of freedom</i>	<i>Mean Square</i>	<i>F</i>	<i>R²</i>
<i>Regression</i>	0.95	922	1.029×10^{-3}	1.22×10^3	0.9903
<i>Residual</i>	96.87	77	1.258		
<i>Total</i>	97.82	999			

▪ ***F-Test***

The hypothesis test was once again used to check whether or not there is a regression relation between the dependent variable y and the set of X variables. The considered significance level α is 5%, consequently the significance level of the test is 95%.

$$F = \frac{MSR}{MSE} = 1.029 \cdot 10^3 > F_{77,922,0.95} = 1.295, \square \text{ reject } H_0 \quad (4.2)$$

From the hypothesis test we can conclude that the null hypothesis H_0 must be rejected in detriment to hypothesis H_a (see section 3.1). Therefore it is assumed that there is a regression relation between the dependent variable y and the set of X variables.

Table XIII contains the $\pm 2\sigma$ confidence bounds for all the MLRM designed for this test system. AS can be seen, the confidence intervals are a little bit larger than the ones presented in the previous test case, ranging from 4% to 18% error. Once again, after obtaining the coefficients for all MLRMs, individual tests were performed on them to verify their accuracy in estimating VSM. Table XIV shows some random selected system operating conditions at where the MLRMs were tested. The testing scenarios represent a different load increase direction from the ones used for training.

The results presented in table XIV show that the estimation error is in accordance with the values estimated in table XIII. Although most of the errors fall within the $\pm 2\sigma$ range, some of them do not. The reason is once again because the confidence bounds only tell us how much data is expected to be found within its boundaries. Error values out of the confidence bounds can still occur with a low probability.

Table XIII: Confidence Intervals

<i>Model</i>	<i>Standard Deviation (%)</i>	<i>Confidence interval in % ($\pm 2\sigma$)</i>
<i>MLRM 1</i>	5.04	± 10.08
<i>MLRM 2</i>	3.74	± 7.48
<i>MLRM 3</i>	2.47	± 4.94
<i>MLRM 4</i>	4.18	± 8.36
<i>MLRM 5</i>	4.85	± 9.70
<i>MLRM 6</i>	4.71	± 9.42
<i>MLRM 7</i>	8.30	± 16.60
<i>MLRM 8</i>	9.15	± 18.30
<i>MLRM 9</i>	No data	No data
<i>MLRM 10</i>	No data	No data

**** The % values of standard deviation and confidence interval are always with respect to the maximum VSM utilized to train the models**

Table XIV: Estimated values

<i>Model</i>	<i>Actual VSM (MW)</i>	<i>Estimated VSM (MW)</i>	<i>Error %</i>
<i>MLRM 1</i>	400.0	362.8	-9.28
<i>MLRM 2</i>	456.0	495.1	8.58
<i>MLRM 3</i>	418.0	434.2	3.88
<i>MLRM 4</i>	368.0	404.4	9.89
<i>MLRM 5</i>	581.0	546.0	-6.02
<i>MLRM 6</i>	237.0	245.1	3.42
<i>MLRM 7</i>	337.0	355.6	5.52
<i>MLRM 8</i>	181.0	162.5	-10.19
<i>MLRM 9</i>	No data	No data	No data
<i>MLRM 10</i>	No data	No data	No data

**** The negative value in error estimation means underestimation of the VSM; positive values represent overestimation of VSM.**

- *Model improvement using Box Cox transformation*

In order to improve normality conditions of the residual distribution, a procedure named Box-Cox was applied. The Box-Cox technique is basically a variable transformation of the dependent variable y (VSM) of the type $y' = y^\alpha$, where α is any power ranging from -2 to 2 usually. The procedure basically test what power transformation better changes the data in a way that the residual distribution of the transformed variable will have a closer to normal probability distribution. However, only significant departures from normality would render spurious results. Although the distribution is more peaked than the previously studied case, the fact that the tails of the distribution are well behaved indicates that most of the data will be within the $\pm 2\sigma$ confidence interval.

The transformation coefficient that provided best results was $\alpha = 0.8$, a clearly improvement on the distribution shape can be noticed in fig 22 and fig 23, when compared to fig 19 and fig 20. This improvement on the pdf of the residuals is considered to be sufficiently close to a normal distribution by now. In case the power transformation is not considered to be satisfactory and a more precise normal distribution is required, data base re-sampling using a variable load increase step size during the PV stress is an alternative.

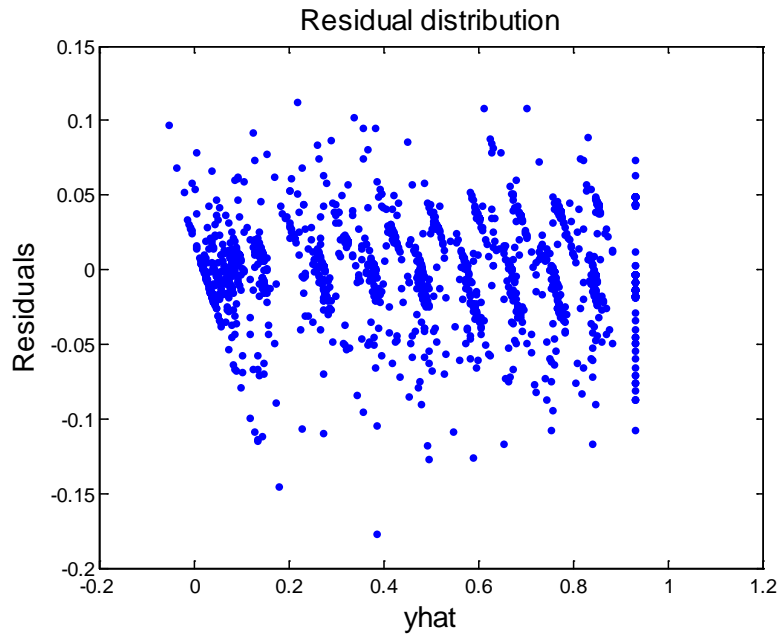


Fig 22: Residual distribution

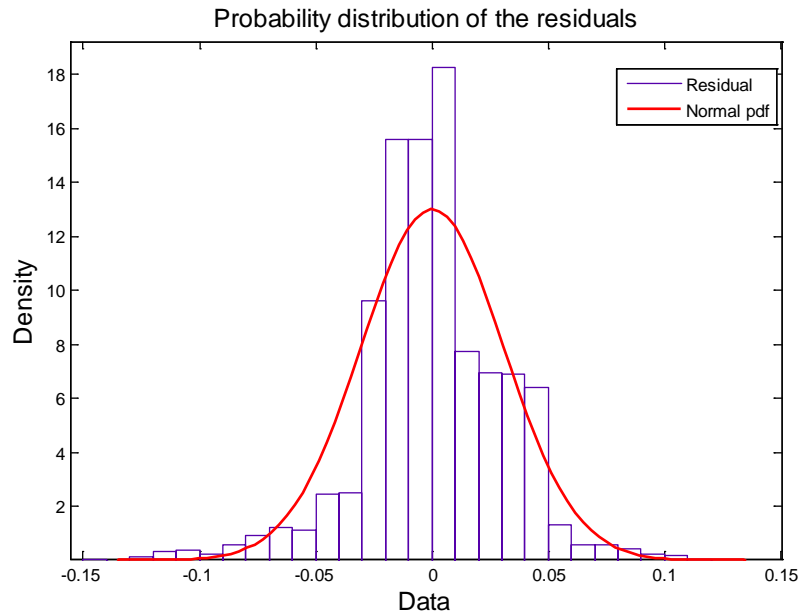


Fig 23: Residual histogram

The parameters of the normal pdf presented on fig 23 are given in table XV below.

Table XV: Distribution Parameters

<i>Parameter</i>	<i>Estimate</i>	<i>Standard Error</i>
<i>Mean (μ)</i>	-6.83×10^{-015}	0.000686
<i>Standard Deviation (σ)</i>	0.0300	0.000486

From the table XV above we can see that the mean value parameter of the normal distribution was approximately zero, which confirms the fact that the residual distribution is centered. The assumption of normal distribution depends on the designer's level of comfort after analyzing the data. It is clear that the histogram presented in fig 23 does not follow the exact normal pdf. The analysis of parameters like kurtosis and skewness can give some hints about the overall characteristic of the distribution, which in this case were considered acceptable.

Table XVI presents the statistics of the ANOVA table for the MLRM – 2. Once again, the model has a high R-squared value.

Table XVI: ANOVA

<i>Source</i>	<i>Sum of Squares</i>	<i>Degrees of freedom</i>	<i>Mean Square</i>	<i>F</i>	<i>R²</i>
<i>Regression</i>	1.88	1922	9.80×10^{-4}	2.44×10^3	0.9899
<i>Residual</i>	1.84×10^2	77	2.40		
<i>Total</i>	1.86×10^2	1999			

If the predicted VSM values were exactly the same as the ones used during training and no error in estimation were present, then the points in fig 24 should all lined up along the solid line. The fact is that the regression is not totally exact, and some spreading can be observed. Such data spreading represents the error in VSM estimation. The error can be modeled and a probability distribution function can be fit to the residuals as shown before.

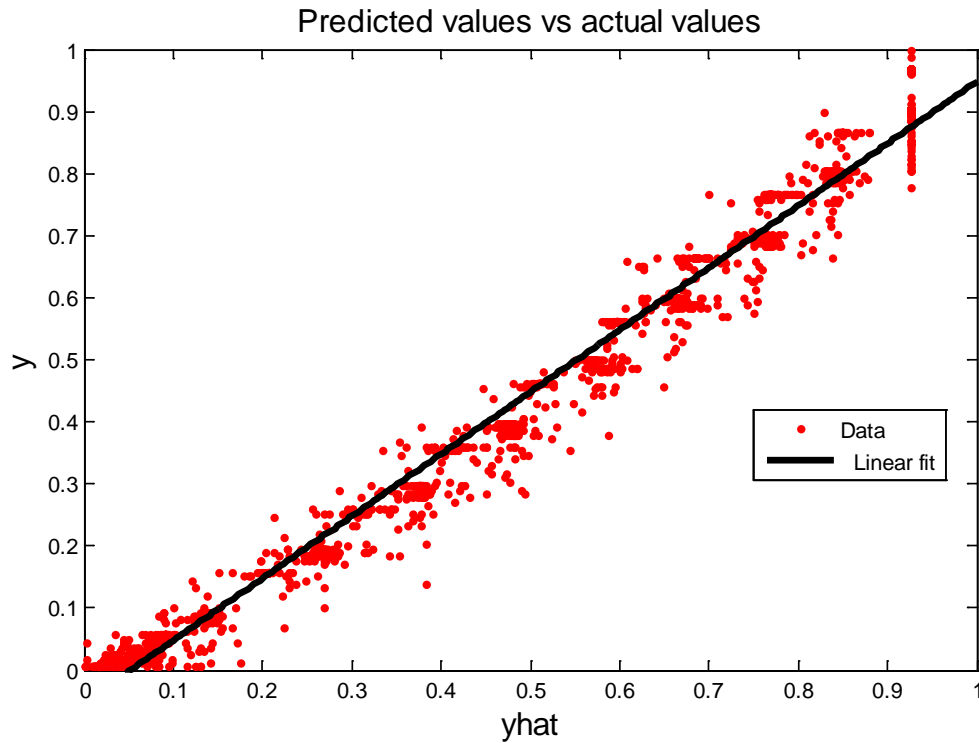


Fig 24: Regressed values vs. actual values of VSM.

▪ ***F-Test***

The hypothesis test was once again used to check whether or not there is a regression relation between the dependent variable y and the set of X variables. The

considered significance level α is 5%, consequently the significance level of the test is 95%.

$$F = \frac{MSR}{MSE} = 2.44 \times 10^3 > F_{77,1922,0.95} = 1.287, \square \text{ reject } H_0$$

From the hypothesis test above, it can be concluded that the null hypothesis H_0 must be rejected in detriment to hypothesis H_a . Therefore it is assumed that there is a regression relation between the dependent variable y and the set of X variables.

Table XVII contains all the standard deviations and the $\pm 2\sigma$ confidence bounds for all the MLRM. Once again, the confidence bounds range from 4% to 16%, what can be considered an acceptable error range.

Table XVII: Confidence Intervals

<i>Model</i>	<i>Standard Deviation (%)</i>	<i>Percentage of estimated error within $\pm 2\sigma$ (95.44% of the estimations)</i>
<i>MLRM1</i>	4.63	± 9.26
<i>MLRM 2</i>	3.00	± 6.00
<i>MLRM 3</i>	2.16	± 4.32
<i>MLRM 4</i>	4.02	± 8.04
<i>MLRM 5</i>	4.96	± 9.92
<i>MLRM 6</i>	4.20	± 8.4
<i>MLRM 7</i>	7.23	± 14.46
<i>MLRM 8</i>	8.33	± 16.66
<i>MLRM 9</i>	No data	No data
<i>MLRM 10</i>	No data	No data

After obtaining the coefficients for all MLRMs, tests were performed on the MLRMs to verify their accuracy in estimating VSM. Table XXVIII shows some random selected system operating conditions at where the MLRMs were tested. Once again, the testing scenarios represent different load increase directions from the ones used for training.

The results presented in table XVIII show that almost all estimated errors are within the confidence bounds presented in table XVII. Although most of the errors fall within the $\pm 2\sigma$ range, some of them do not. The reason is, once again, because the confidence bounds only tell us how much data is expected to be found within its boundaries. Error values out of the confidence bounds can still occur with a low probability.

Table XVIII: Estimated values

<i>Model</i>	<i>Actual VSM (MW)</i>	<i>Estimated VSM (MW)</i>	<i>Error %</i>
<i>MLRM 1</i>	954.7	965.3	1.10
<i>MLRM 2</i>	749.7	753.9	0.56
<i>MLRM 3</i>	455.5	469.1	2.99
<i>MLRM 4</i>	682.3	663.3	-2.78
<i>MLRM 5</i>	290.5	296.6	2.1
<i>MLRM 6</i>	244.8	218.0	-10.95
<i>MLRM 7</i>	96.9	95.9	-1.03
<i>MLRM 8</i>	238.3	253.4	6.34
<i>MLRM 9</i>	No data	No data	No data
<i>MLRM 10</i>	No data	No data	No data

****** *The negative value in error estimation means underestimation of the VSM; positive values represent overestimation of VSM.*

▪ *ANN for MLRM selection*

After designing all the MLRM that will be used in online VSM estimation, operators need to select the appropriate model based on each system condition. Since load variations and system topological variations could lead to an unmanageable number of scenarios, and ANN was again designed with the purpose of selecting the proper MLRM to be used.

System data (PMU measurements) are supplied to the inputs of the ANN. The ANN outputs an index, which represents what MLRM needs to be used. Since voltage stability is the phenomenon being studied, the PMU data considered as inputs to the ANN were bus voltage magnitude and angles.

Due to the large number of buses in the studied areas (224 buses), principal component analysis was utilized in order to identify the measurement that provides a significant amount of information. Therefore a reduced number of PMU measurements will need to be taken from those selected buses, which further improves the economical aspects of the methodology by reducing the number of installed devices. A total of 42 buses were found to provide high explanation to scenario identification.

After identifying the most meaningful measurements, the ANN is trained for several conditions that could occur normally in the system. Several load increase directions (20 in this case) and contingencies (430 in this case) were considered in the ANN training part. The testing data represents the same set of contingencies and a random load increase direction around the forecasted load increase direction.

Table XIX describes the accuracy of ANN for different conditions of the system. All the tested cases are independent from the training set and represent a different loading condition for all the 430 contingencies utilized in the training phase. Initially, PMUs were considered to be installed at each one of the 224 buses in the system. A more realistic

implementation has considered the selection of buses by using principal component analysis and consequently reducing the number of deployed devices. Both cases were tested for the following conditions:

- Situations where there is no noise added to the input measurements
- Considering random Gaussian noise added to the input signal. First case considering noise standard deviation equals to 5% of maximum signal amplitude (noise 1)
- Considering random Gaussian noise added to the input signal. First case considering noise standard deviation equals to 10% of maximum signal amplitude (noise 2)
- Considering random Gaussian noise added to the input signal. First case considering noise standard deviation equals to 15% of maximum signal amplitude (noise 3)
- Considering a missing PMU signal coming into the control room

The ANN was trained with noise and all the above scenarios were tested once again. The type of noise added during training was a Gaussian noise with zero mean and standard deviation equals to 10% of maximum input signal amplitude.

From table XIX it can be seen that the overall accuracy of the ANN is high (above 83% for all the cases). Considering the case when there are PMUs installed in all the buses (224 buses in this case). It is clear from table XIX that the addition of noise to the inputs reduces the accuracy of the network (line 2, columns 1-4). The addition of noise to the training data can improve the accuracy of the ANN on cases where there is noise present in the input data (line 3, columns 1-4). The loss of a PMU signal did not affect the accuracy of the ANN significantly (line2-3, column4). For testing purposes, the PMU signal that provides most information according to PCA analysis is the one that is being missing in the simulation.

Table XIX: Artificial Neural Network testing

<i>Number of PMUs installed</i>	<i>Configuration</i>	<i>Testing error – No Noise</i>	<i>Testing error – Noise 1</i>	<i>Testing error – Noise 2</i>	<i>Testing error – Noise 3</i>	<i>Missing PMU data</i>
<i>PMU installed in all 224-buses</i>	<i>Training without noise</i>	92.5%	91.7%	88.8%	83.8%	91.9%
	<i>Training with noise</i>	93.6%	93.6%	92.8%	92.3%	93.4%
<i>PMU installed in 42 buses (after PCA selection) *</i>	<i>Training without noise</i>	93.7%	93.6%	92.9%	91.9%	93.5%
	<i>Training with noise</i>	94.0%	93.6%	93.1%	92.6%	94.2%

Considering the case where the PMU locations were selected using PCA analysis, a reduced set of buses is then selected to have PMUs installed. In this case, 42 buses were selected out of 224. Again, the addition of noise to the inputs reduces the accuracy of the network (line 2, columns 1-4). The addition of noise to the training data can improve the accuracy of the ANN on cases where there is noise present in the input data (line 3, columns 1-4). The loss of a PMU signal does compromise the accuracy of the ANN significantly in this case (line2-3, column4). The reason is because the amount PMU measurement is already reduced. Therefore losing an extra PMU signal when there is a reduced set of measurements causes a higher impact on the recognition capability of the ANN.

Surprisingly, the performance of the ANN with a reduced set of input variables is slightly better than the case where all the 224 buses are considered. This reduced performance when many inputs are considered is due to the fact that there is a “competition” among the input variables. Such competition can indeed reduce the accuracy of the network as mentioned in [35]-[36].

Fig 25 shows the output error of the ANN and the mean squared training error for the case when the ANN is trained with noise and has PMUs deployed all across the system. It can be noticed that the output error of the ANN increases as the amplitude (standard deviation) of the Gaussian noise increases as well, whereas the training mean squared error stops being significantly reduced after it reaches the value of 10^{-2} . From table XIX, it can be noticed that by training the network considering some noise in the training data can improve the performance of the ANN when there is actually noise in the input measurements. This could be used to boost ANN’s performance and MLRM selection accuracy.

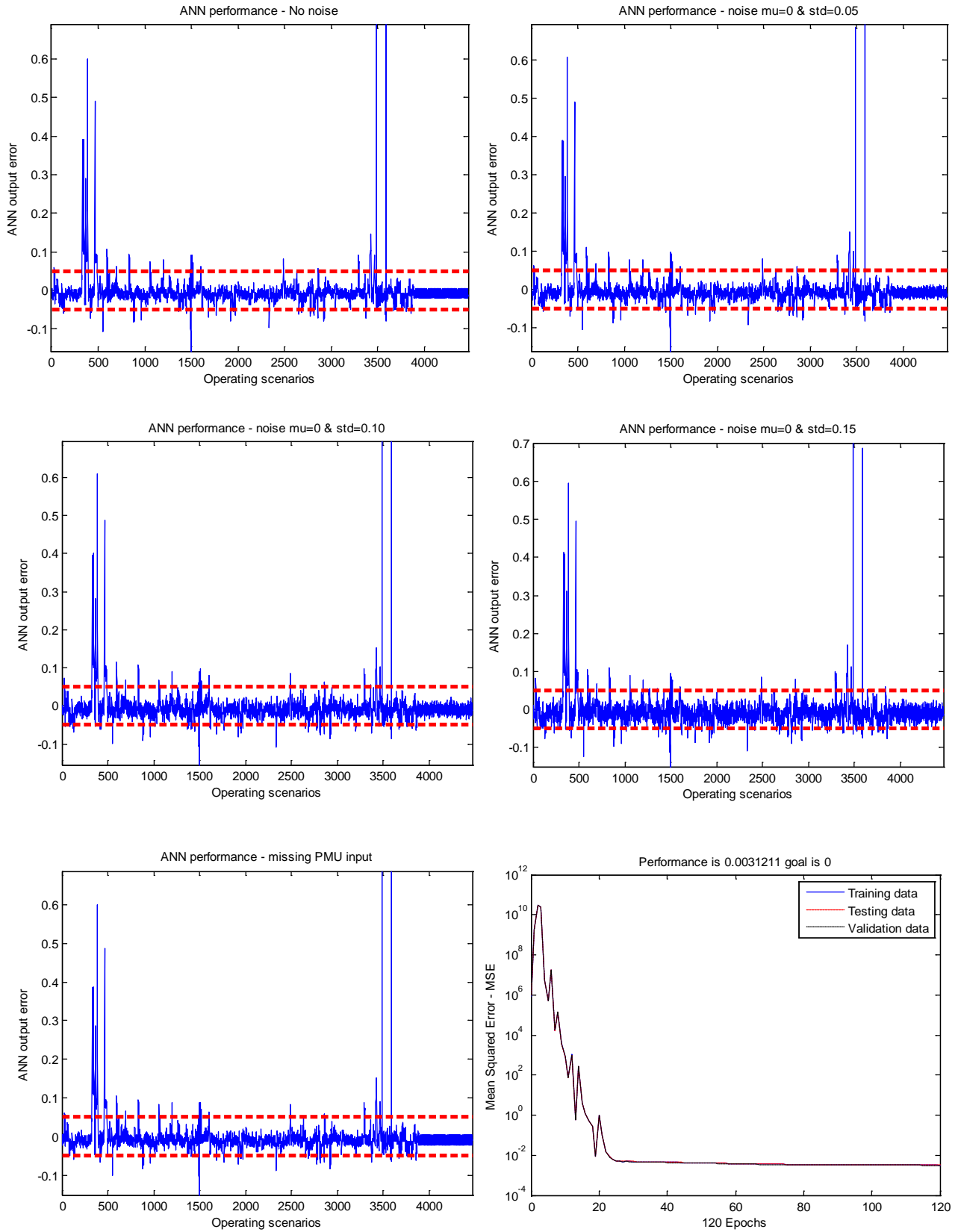


Fig 25: Output error of ANN for different conditions and means squared training error

Overall, the performance of the ANN is usually above 90% for most of the cases after suitable training strategy (training with noise), which means that the proper MLRM will be selected correctly 90% of the time. This high level of accuracy makes us believe that the implementation of such methodology would be possible in real sized systems.

5. Conclusions

A technique to estimate voltage stability margin in real-time is presented in this project. Such methodology makes use of multi-linear regression models and artificial neural networks in order to estimate how far the system is from a voltage collapse. Reactive power reserves were associated with the amount of voltage stability margin using several multi-linear regression models. An artificial neural network selects the most appropriate multi-linear regression model to be used at each instant by identifying current system condition. PMU measurements are used to collect system bus voltage magnitudes and angles in real-time and make it available to be used by the neural network.

Compared to PMU based techniques that make use of the Thevenin equivalent approach, the proposed technique estimates voltage stability margin for a large area of the system, rather than local buses or transmission corridors. This characteristic makes the approach more suitable for practical implementations as it covers larger portions of the system, rather than single transmission corridors or load buses.

The accuracy of the estimations is relatively good and the methodology could be used in real-time applications. The technique is capable of handling real sized systems by the utilization of well established commercial grade software.

This project is given continuity through a support from a local utility and PSerc member. The methodology will be tested on a reduced case of the eastern interconnection.

References

- [1] United States Government Printing Office (USGPO): *Energy Independence and security act of 2007*. Available at: http://frwebgate.access.gpo.gov/cgi-bin/getdoc.cgi?dbname=110_cong_bills&docid=f:h6enr.txt.pdf.
- [2] United States Department of Energy, “Smart Grid”, available at: <http://www.oe.energy.gov/smartgrid.htm>.
- [3] U.S.-Canada Power System Outage Task Force, “Final Report on the August 14, 2003 Blackout in the United States and Canada: Causes and Recommendations”, April 5, 2004. Available at: <http://www.nerc.com/filez/blackout.html>
- [4] North American Electric Reliability Corporation (NERC), “Voltage and reactive control – VAR-001-1”, available at: <http://www.nerc.com/files/VAR-001-1.pdf>.
- [5] North American Electric Reliability Corporation (NERC), “Voltage and reactive control – VAR-001-1a”, available at: <http://www.nerc.com/files/VAR-001-1a.pdf>.
- [6] S. Chakrabarti, B. Jeyasurya, “Multi-contingency voltage stability monitoring of power systems using radial basis function network”, in *Proc. of the 13th International Conference on Intelligent Systems Application to Power Systems*, Nov. 2005.
- [7] B. Moradzadeh, S. H. Hosseinian, M. R. Toosi, M. B. Menhaj, “Online voltage stability monitoring and contingency ranking using RBF neural network”, in *Proc. IEEE-PSE Conference and Exposition in Africa, PowerAfrica*, 2007.
- [8] M. Scala, M. Trovato and F. Torelli, “A neural network-based method for voltage security monitoring”, *IEEE Trans. Power Syst.*, Vol. 11, Issue 3, Aug. 1996.
- [9] D. Popvic, D. Kukolj and F. Kulic, “Monitoring and assessment of voltage stability margins using artificial neural networks with a reduced input set”, *IEE Proc. Gener. Transm. Distrib.*, 1998.
- [10] H. Wan and Y. Song, "Hybrid supervised and unsupervised neural network approach to voltage stability analysis", *Electric Power Systems Research*, vol. 47, 1998.
- [11] L. Srivastava, S. Singh, and J. Sharma, “Estimation of loadability margin using parallel self-organizing hierarchical neural network”, *Computers and Electrical Engineering*, Volume 26, Issue 2, March 2000.
- [12] M. Larson, C. Rehtanz, J. Bertsch, “Real-time voltage stability assessment of transmission corridors”, *IFAC Power Plants and Power Systems Control*, 2003.

- [13] S. Corsi, G. Taranto, "A real-time voltage instability identification algorithm based on local phasor measurements", *IEEE Transactions on Power Systems*, Vol. 23, No. 3, Aug. 2008.
- [14] Y. Gong, N. Schulz, A. Guzman, "Synchrophasor-based real-time voltage stability index", *IEEE Power System Conf. and Exposition PSCE*, 2006.
- [15] M. Glavic, T. Van Cutsem, "Detecting with PMUs the onset of voltage instability cause by a large disturbance", *IEEE Power and Energy Society General Meeting*, 2008.
- [16] S. Grijalva, "Integrating real-time operations and planning using same-format power system models", *IEEE Power Engineering Society General Meeting*, 2007.
- [17] B. Leonardi, V. Ajjarapu, "Investigation of various generator reactive power reserve (GRPR) definitions for online voltage stability/security assessment", *IEEE Power and Energy Society General Meeting*, 2008.
- [18] P. Ruiz, P. Sauer, "Reactive power reserve issues", *North American Power Symposium*, 2006.
- [19] L. Bao, Z. Huang, and W. Xu, "Online voltage stability monitoring using VAR reserves", *IEEE Transactions on Power Systems*, vol. 18, issue 4, Nov. 2003.
- [20] P. Kundur, J. Paserba, V. Ajjarapu, G. Andersson, A. Bose, C. Canizares, N. Hatziargyriou, D. Hill, A. Stankovic, C. Taylor, T. Van Cutsem, V. Vittal, "Definition and classification of power system stability IEEE/CIGRE joint task force on stability terms and definitions", *IEEE Transactions on Power Systems*, Vol. 19, Issue 3, Aug. 2004.
- [21] V. Ajjarapu, Computational Techniques for Voltage Stability Assessment and Control, New York, NY, Springer, 2006.
- [22] C. Canizares (working group chairman), IEEE Special Publication, "Voltage Stability Assessment: Concepts, Practices and Tools", July 2003.
- [23] C Taylor, Power System Voltage Stability, New York, NY, McGraw-Hill, 1994.
- [24] M. Pandit, L. Srivastava, J. Sharma, "Counterpropagation network for voltage contingency ranking exploiting coherency for feature selection" in *Proc. of the IEEE INDICON* (India Annual Conference), 2004.
- [25] I. Hiskens, R. Davy, "Exploring the power flow solution boundary", *IEEE Transactions on Power Systems*, Vol. 16, No. 3, August 2001.
- [26] C. Tavora, O. Smith, "Equilibrium analysis of power systems", *IEEE Transactions on Power Apparatus and Systems*, vol. PAS-91, no. 3, 1972.

- [27] J. Jarjis, F. Galiana, "Quantitative analysis of steady state stability in power systems", *IEEE Transactions on Power Apparatus and Systems*, vol. PAS-100, no. 1, Jan. 1981.
- [28] D. Kleinbaum, L. Kupper, K. Muller, A. Nizam, Applied regression analysis and other multivariable methods, 3rd edition, Pacific Grove, CA, 1998.
- [29] D. Montgomery, E. Peck, G. Vining, Introduction to linear regression analysis, 4th edition, Hoboken, N.J., Wiley-Interscience, 2006.
- [30] M. Kutner, C. Nachtsheim, J. Neter, and W. Li, *Applied Linear Statistical Models*. 5th edition, New York: McGraw-Hill/Irwin (series operations and decision sciences), 2005.
- [31] A. Miller, Subset selection in regression, 2nd edition, Chapman & Hall/CRC, 2005.
- [32] I. Guyon, A. Elisseeff, "An introduction to variable and feature selection. *Journal of Machine Learning Research*, Vol.3, 2003.
- [33] H. Liu, L. Yu, "Toward integrating feature selection algorithms for classification and clustering", *IEEE Trans. Knowl. Data Eng.*, Vol. 17, Issue 4, April 2005.
- [34] S. Singhi, H. Liu, "Feature subset selection bias for classifications learning", in *Proc. of the 23rd International Conference on Machine Learning, Pittsburgh-PA*.
- [35] C. Bishop, Pattern recognition and machine learning, 1st edition, New York, NY, Springer Science, 2006.
- [36] C. M. Bishop, Neural Networks for Pattern Recognition, Oxford University Press (1995). ISBN 0-19-853864-2.
- [37] A.G Phadke, "Synchronized phasor measurements-a historical overview", in *Proc. of IEEE/PES Transmission and Distribution Conference and Exhibition 2002, Asia Pacific*.
- [38] A.G. Phadke, J.S Thorp, "History and applications of phasor measurements", in *Proc. of IEEE PES Power Systems Conference and Exposition, PSCE 2006*.
- [39] A. P. Sakis Meliopoulos, G. J. Cokkinides, F. Galvan, B. Fardanesh and P. Myrda, "Delivering accurate and timely data to all – model-based substation automation applications for advanced data availability," *IEEE Power & Energy Magazine*, pp. 74-86, May/June 2007.
- [40] Normal probability distribution: http://en.wikipedia.org/wiki/Normal_distribution.
- [41] I. T. Jolliffe, Principal component analysis, 1st edition, Springer-Verlag, New York-NY, 1986.

- [42] R. A. Johnson, D. W. Wichern, Applied multivariate statistical analysis, 4th edition, Prentice hall, Upper Saddle River-NJ, 1998.

Project Publications

- [1] B. Leonardi and V. Ajjarapu, “Development of Multi-linear Regression Models for Online Voltage Stability Margin Estimation: to appear in the IEEE transactions on Power Systems, 2010
- [2] B. Leonardi, V. Ajjarapu, “Investigation of various generator reactive power reserve (GRPR) definitions for online voltage stability/security assessment”, *IEEE Power and Energy Society General Meeting*, 2008

Appendix A

- *Least Square Method*

Consider the problem of minimizing the vector of residuals $\mathbf{\varepsilon}$.

$$\underset{\beta}{\text{Min}} \|\mathbf{\varepsilon}\|^2 = \underset{\beta}{\text{Min}} \|\mathbf{y} - \mathbf{X}\beta\|^2$$

This quadratic unconstrained optimization problem is classically solved by taking the gradient of the vector $\mathbf{\varepsilon}$ and making it equal to zero.

$$\nabla_x \|\mathbf{\varepsilon}\|_2^2 = \nabla_x \|\mathbf{y} - \mathbf{X}\beta\|_2^2 = \nabla_x [(\mathbf{y} - \mathbf{X}\beta)^T (\mathbf{y} - \mathbf{X}\beta)] = 0$$

$$\nabla_x [\mathbf{y}^T \mathbf{y} - \mathbf{y}^T \mathbf{X}\beta - \beta^T \mathbf{X}^T \mathbf{y} + \beta^T \mathbf{X}^T \mathbf{X}\beta] = 0$$

And since $\mathbf{y}^T \mathbf{X}\beta = \beta^T \mathbf{X}^T \mathbf{y} = (\mathbf{X}^T \mathbf{y})^T \beta$ we can rewrite the above equation as:

$$\nabla_x [\mathbf{y}^T \mathbf{y} - 2(\mathbf{X}^T \mathbf{y})^T \beta + \beta^T \mathbf{X}^T \mathbf{X}\beta] = 0$$

$$-2(\mathbf{X}^T \mathbf{y}) + 2\mathbf{X}^T \mathbf{X}\beta = 0$$

$$\hat{\beta} = (\mathbf{X}^T \mathbf{X})^{-1} (\mathbf{X}^T \mathbf{y})^T$$

Where $\hat{\beta}$ is the best linear unbiased estimator (BLUE) for the vector of regression coefficients β .

- *ANOVA table and statistical variables*

In the sequence, many of the statistical variables used throughout the text in the ANOVA tables are defined.

SSE - Residual sum of squares.

SSR - Regression sum of squares.

SST - Total sum of squares.

R^2 - Coefficient of multiple determinations.

DF_R - Regression degrees of freedom.

DF_E - Residual degrees of freedom.

DF_T - Total degrees of freedom

MSR - Regression mean square error

MSE – Residual mean square error

$$SSR = \sum_{i=1}^n (\hat{y}_i - \bar{y})^2$$

$$SSE = \sum_{i=1}^n (y_i - \hat{y}_i)^2$$

$$SST = \sum_{i=1}^n (y_i - \bar{y})^2$$

$$SST = SSR + SSE$$

$DF_R = k$, (the number of independent variables in the MLRM).

$DF_E = n - k - 1$ (equals to the total number of samples – $k - 1$).

$$DF_T = DF_R + DF_E = n - 1.$$

$$MSE = \frac{SSE}{DF_E}$$

$$MSR = \frac{SSR}{DF_R}$$

$$R^2 = \frac{SST - SSE}{SST}$$

- Principal component analysis (PCA)

The main idea of principal component analysis is to reduce the dimensionality of the data set which consists of a large number of correlated variables [41]. In this project, PCA was used to identify which variables can be used to identify the current system topology. Once the variables that provide meaningful information are identified, a reduced set containing all of the selected variables is utilized as inputs to the neural network. The reduced set of inputs reduces the complexity and further improves the performance of the ANN.

PCA can be mathematically defined as the eigenvalue decomposition of the data covariance matrix. The larger the eigenvalue, the higher is the importance of the corresponding eigenvector (principal component).

Assuming the data matrix is given by $\mathbf{X} = [\mathbf{x}_1 \ \mathbf{x}_2 \ \cdots \ \mathbf{x}_p]$ where the columns represent system variables, in this case bus voltage magnitudes and angles, and the rows represent different samples of the variables. Assuming that matrix \mathbf{X} is $n \times p$, i.e., has p variables and n samples, the covariance between two variables x_a and x_b from matrix \mathbf{X} can be calculated using the following formula:

$$\sigma_{ab} = \text{Cov}(x_a, x_b) = \frac{\sum_{i=1}^n (x_{ia} - \bar{x}_a)(x_{ib} - \bar{x}_b)}{n - 1}$$

$$\bar{x}_a = \frac{\sum_{i=1}^n (x_{ia})}{n}$$

$$\bar{x}_b = \frac{\sum_{i=1}^n (x_{ib})}{n}$$

Once the covariances between all the elements of the data matrix \mathbf{X} are calculated, the covariance matrix (Σ) can be written as follows:

$$\Sigma = \begin{pmatrix} \sigma_{11} & \sigma_{12} & \cdots & \sigma_{1p} \\ \sigma_{21} & \sigma_{22} & \cdots & \sigma_{2p} \\ \vdots & \vdots & \ddots & \vdots \\ \sigma_{p1} & \sigma_{p2} & \cdots & \sigma_{pp} \end{pmatrix}$$

The diagonal elements represent the variances of the each variable. The off-diagonal elements represent the covariance between two different variables. After the covariance matrix is found, the eigenvalue decomposition of Σ is carried out as follows:

$$\Sigma V = V \Lambda$$

The matrix Λ is a diagonal eigenvalue matrix of Σ . V is the eigenvector matrix and can be represented as $V = [\mathbf{v}_1 \ \mathbf{v}_2 \ \cdots \ \mathbf{v}_p]$. The proportion of total sample variance due to the k th principal component is:

$$\frac{\lambda_k}{\lambda_1 + \lambda_2 + \cdots + \lambda_p}, \quad k = 1, 2, \dots, p$$

After performing the eigenvalue decomposition of the covariance matrix, the largest eigenvalues are selected to start the dimensionality reduction process. The size of the eigenvalue represents how much of the data can be explained by the specific variable.

Plotting all the eigenvalue in a simple line plot is an easy way to identify how many eigenvalues would be required reduce the dimension of the data set and still obtain a high level of information from the remaining variables. The aforementioned eigenvalue plot is also known as *scree test*. Usually, most of the total population variance (for instance, 80% to 90%) can be explained by the first few eigenvalues.

Once k eigenvalues are selected out of a total of p , a weighted summation of the elements of the principal component vector defines how much importance each variable

has on each principal component. This weighted summation will be called *variable importance factor* (VIF).

$$VIF_j = \sum_{i=1}^k \lambda_i |v_{ji}|$$

Where:

- k – is the number of selected eigenvalues (scores)
- j – is the selected variable
- λ_i – eigenvalue i
- v_{ji} – eigenvector i variable j

Although the above specified factor can be, another popular coefficient termed *correlation coefficient* (CC) can also be used to interpret the importance of the variables. Despite the fact that VIF and CC can lead to different rankings as measures of the importance of the variables to a given component, it has been observed in practice that these rankings do not differ appreciably [42]. In this work, the VIF was the selected determine variable importance.

After VIF is calculated for all the variables, a cutoff value (c_0) is specified. This cutoff value is a heuristic value and can be defined by the designer. The final set of selected variables (Ω) is then given by:

$$\{x_j \in \Omega \mid VIF_j \geq c_0\}, \quad j=1, \dots, p$$